FORSCHUNGSZENTRUM JÜLICH GmbH KFA

Institut für Kernphysik

Final State Interaction in Quasielastic Electron Scattering

Sabine Jeschonnek

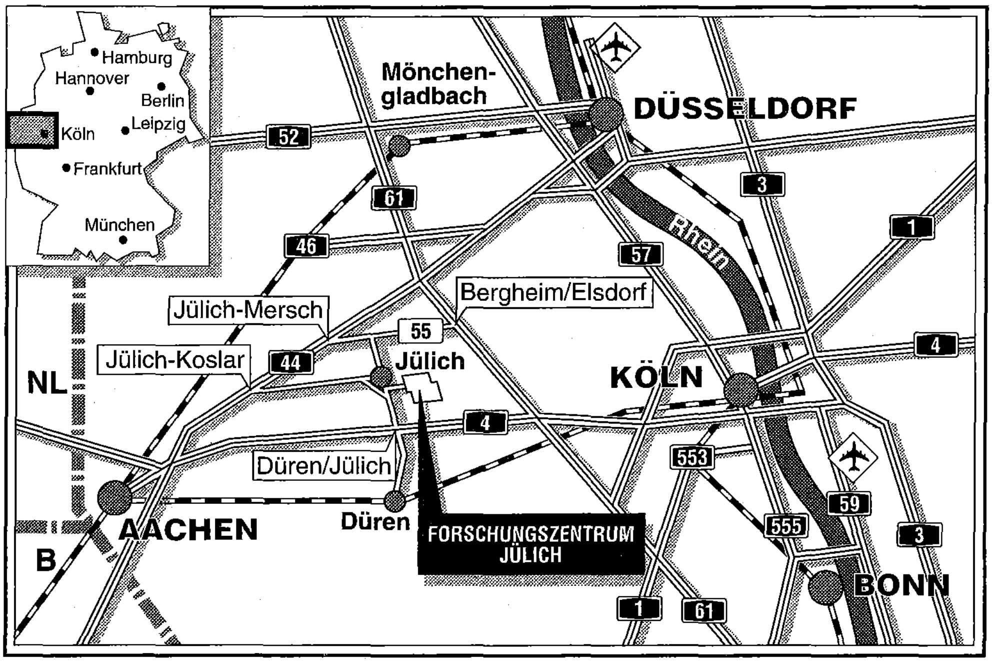

Berichte des Forschungszentrums Jülich ; 3175
ISSN 0944-2952
Institut für Kernphysik   Jül-3175
D 5 (Diss. Universität Bonn)

Zu beziehen durch: Forschungszentrum Jülich GmbH · Zentralbibliothek
D-52425 Jülich · Bundesrepublik Deutschland
Telefon: 02461/61-6102 · Telefax: 02461/61-6103 · Telex: 833556-70 kfa d

Final State Interaction in Quasielastic Electron Scattering

Sabine Jeschonnek

Abstract

In dieser Arbeit wird die Endzustandswechselwirkung in der quasielastischen Elektronenstreuung an leichten Kernen bei hohen Viererimpulsüberträgen untersucht.
Der Wirkungsquerschnitt der $(e, e'p)$ Reaktion an Kernen ist der Impulsverteilung der Nukleonen im Kern direkt proportional, wenn man die Wechselwirkung des herausgeschlagenen Nukleons mit den restlichen Nukleonen vernachlässigt. Die Endzustandswechselwirkung im Energiebereich von $1\,GeV$ und mehr, der für die geplanten Experimente an CEBAF relevant ist, ist jedoch groß und im Gegensatz zur Endzustandswechselwirkung bei kleineren Energien im wesentlichen absorptiv und diffraktiv. Sie kann mit der Glauber Theorie beschrieben werden.
Die Untersuchung der Elektronenstreuung an unpolarisiertem und tensorpolarisiertem Deuterium und an Helium-4 zeigt, daß die Endzustandswechselwirkung für höhere missing momenta dominiert. Sie führt zu einer starken Anisotropie der Winkelverteilung der Spektralfunktion, insbesondere zu einem Peak bei $90°$ für höhere missing momenta, und zu einer Vorwärts-Rückwärts Asymmetrie. Dabei ist die Auswirkung der Endzustandswechselwirkung je nach Kinematik und Absolutbetrag des missing momentum unterschiedlich, sie kann sowohl zur Verstärkung als auch zur Abschwächung führen. Die Details der Wellenfunktion bei kleinen Abständen der Nukleonen haben auf das Endergebnis nur einen sehr geringen Einfluß. Berücksichtigt man bei der Berechnung der Spektralfunktion die Endzustandswechselwirkung, so kann man schließen, daß eine experimentelle Unterscheidung der Vorhersagen von verschiedenen Modellen für die D-Welle des Deuterons oder für die Form der Korrelationen in Helium unmöglich sein wird.
Die Eigenschaften der Endzustandswechselwirkung werden von der Nukleon-Nukleon Streuung bestimmt. Die Endzustandswechselwirkung induziert daher ein universelles Verhalten der Spektralfunktion unabhängig vom spezifischen Target-Kern.

Contents

Chapter 1

Introduction

Electron scattering from nuclei has revealed interesting and important information on the structure of nuclei over the past decades. The electron and nucleus interact electromagnetically by exchanging a virtual photon; one can vary the transferred momentum at fixed transferred energy so long as the four-momentum transfer is space-like. This is a big advantage over experiments with real photons. The electromagnetic interaction is well known and relatively weak compared to the strong interaction of the nucleons in the nucleus, of order $\alpha = \frac{1}{137}$, so that it can be treated perturbatively.

In elastic electron scattering, the cross section yields information on the charge distribution in the nucleus. Starting with the pioneering work of Hofstadter [1] in the fifties, the charge distribution of a wide range of nuclei was determined precisely in electron scattering experiments. Inelastic inclusive electron scattering gives information on the transition charge and current densities and therefore on the nuclear structure.

The next goal for electron scattering experiments is to investigate the nucleon momentum distribution in nuclei especially at high momenta with exclusive electron scattering. In $(e, e'p)$ experiments, the cross section is proportional to the spectral function, which gives the joint probability to find a nucleon of energy E with a momentum k in the nuclear ground state if one assumes that no final state interaction takes place between the struck proton and the residual nucleus. Although the principal ideas and motivation for such experiments go back to Gottfried's classic works of the early sixties ([2, 3, 4], see also [5, 6, 7, 8, 9]), they are only becoming feasible at the new generation of high luminosity, continuous beam electron facilities (CEBAF, AmPS, MAMI, and Bates).

The independent particle shell model describes the nucleus as a system of nucleons in which each nucleon moves independently in a mean field potential generated by the other nucleons. It is assumed that all the shells are filled with nucleons starting from the lowest energy level up to the highest level, the Fermi level. This model of the atomic nucleus is analogous to Bohr's model of the atom. In contrast to the atom, where the residual interaction of the electrons is weak, the residual interaction of the nucleons in the nucleus is strong and leads to correlations between the nucleons [10]. There exist various types of short range and long range correlations, the best known example of which is the Pauli blocking. Those correlations lead to high nucleon momenta in the nuclear ground state, and an experimental determination of the nucleon momentum distribution at high momenta would shed light on the short distance nucleon-nucleon interaction in the nuclear medium. However, the nucleon momentum distribution cannot be extracted directly from the cross section because the final state interaction between the ejectile and the residual nucleus is present and strong. Basically all data taken in $(e, e'p)$ experiments in the past decade show an important influence of final state interaction [11, 12]. In order to extract the interesting information from the $(e, e'p)$ data, a thorough understanding of the final state interaction is necessary. Currently, there exist many calculations for the effects of final state interaction for experiments with kinetic energies of the proton below or around a few hundred MeV [13].

However, for a study of correlations which are supposed to manifest themselves at higher nucleon momenta, it is mandatory for the detected proton to have a much higher kinetic energy; only high kinetic energies of $1\,GeV$ or more allow to access high momenta of about $2 - 3 fm^{-1}$ in all kinematical conditions. Those high energies of the proton will be achieved at the Continuous Electron Beam Acceleration Facility (CEBAF) for the first time. The other recently commissioned continuous beam facilities MAMI in Mainz, AmPS at NIKHEF in Amsterdam, and Bates at the Massachussetts Institute of Technology operate at lower energies.

Previously, there was no anticipation in the literature that the final state interaction at the GeV energies attainable at CEBAF will be any different from the one at low energies. However, the calculations carried out in this thesis and in [14, 15, 16, 17, 18] show that qualitative and quantitative changes take place. At GeV energies, the final state interaction is strong, diffractive and mainly absorptive. The very nature of nucleon-nucleon interaction changes from the purely elastic potential scattering at low energies to a strongly absorptive, diffractive small angle scattering at kinetic energies of the struck proton larger than $0.5 - 1\,GeV$. In this high energy regime, the Compton wavelength of the struck proton is much smaller than the size of a nucleon and the average nucleon-nucleon separation in nuclei. Therefore, the experience gained at lower energies and the methods used there cannot be applied to the calculation of final state interaction in the diffractive regime. The Glauber model [19, 20] becomes a natural framework for the quantitative description of final state interactions.

For several reasons, light target nuclei are of special interest: On the theoretical side, there are several predictions for the ground state wave functions of light nuclei [21, 22, 23, 24, 25, 26, 27, 28]. The models for those wave functions include not only correlations, but also different types of three-nucleon forces [29, 30, 31]. As the predictions differ considerably, some experimental information is needed as a check of those important features.

A large part of the experimental program at CEBAF is devoted to experiments on light nuclei. The deuteron is important as it is used as a neutron target, and also polarized ^3He is a candidate for this.

Apart from the investigation of the conventional topics of nuclear physics, exclusive electron scattering experiments are discussed as tools for the observation of color transparency. Color transparency is the prediction of quantum chromodynamics (QCD) that at sufficiently high energies the strength of final state interactions should decrease (see, e.g. [32, 33, 34]). There exist different predictions for the onset of color transparency. One of the conditions for color transparency, the requirement that the formation length has to be larger than the nuclear radius, leads to the condition that the four momentum transfer Q^2 has to exceed a certain energy that is connected with the nuclear mass number A: $Q^2 \gtrsim (5-10)A^{\frac{1}{3}}GeV^2$ [35]. It was confirmed by the calculations in [35] that the onset of color transparency is slower for heavy nuclei than light nuclei. The condition for Q^2 indicates that with the Q^2 values attainable today, color transparency can be observed only with light target nuclei. As a prerequisite for the planning of suitable experiments for the search for color transparency and their subsequent analysis, it is necessary to identify the effects of conventional final state interaction, e.g. forward-backward asymmetry, to exclude an erroneous interpretation of conventional final state interaction effects as signals of color transparency [36, 37, 38]. Also, one needs to identify the regions of strong final state interaction, as it should be easier to observe the vanishing of final state interaction effects in those regions [34, 39]. Furthermore, theoretical predictions of color transparency can only be confronted to the forthcoming data if a realistic ground state wave function is employed. Therefore, it is necessary to test the various predictions for few-body wave functions and to find out how the uncertainties in the predicted wave functions influence the final results.

In this thesis and the corresponding publications [14, 15, 16, 17, 18] the effect of final state interactions on the experimental results in $(e, e'p)$ scattering from light nuclei has been investigated using Glauber theory [19, 20]. Calculations of initial and final state interaction effects in proton-nucleus scattering at high energies have employed Glauber theory very successfully (see, e.g. [40, 41] and references therein). The calculations presented here are an exploratory study of final state interaction effects. The major goals were to find out how large final state interaction effects are compared with short range correlation effects, to identify the typical signature of final state interaction effects and the kinematical regions where they dominate, and to find out if and how final state interaction effects and short range correlation effects can be disentangled. Also, different types of ground state wave functions have been employed and their effect on the observed missing momentum distribution has been checked.

This thesis is organized as follows: in the second chapter, the effects of final state interaction at high energies are first discussed at a qualitative level, then the final state interaction operator is discussed at a quantitative level. In chapter 3, the final state interaction effects are calculated for electron scattering from unpolarized deuteron targets. The deuteron is the simplest nucleus, and the experimental study of the short distance (i.e. large momentum) behaviour of the deuteron wave function is of particular importance for understanding the short range properties of the nuclear forces. The deuteron presents an ideal testing ground for the calculation of final state interaction effects as there are realistic deuteron wave functions calculated from NN meson exchange potentials [25, 26] available in a conveniently parameterized form. Therefore, no additional assumptions about the nuclear ground state enter the calculations. In chapter 4, electron scattering from tensor polarized deuterons is investigated. Measurements with a polarized deuteron target provide the tensor analyzing power as additional observable besides the missing momentum distributions. In this chapter, the different models for the deuteron ground state are compared, a main point is the investigation of the sensitivity of the expected experimental results to the D-wave content of the deuteron wave function, for which rather different predictions exist. After having established the dominance of final state interaction effects in electron scattering from deuterons, its influence on experiments with heavier target nuclei is studied. A very suitable nucleus for this investigation is ^4He. On the one hand, it is a very tightly bound system and its properties therefore resemble strongly the ones of heavy nuclei. On the other hand, the relatively small number of four nucleons admits a complete treatment of the problem to all orders in the correlations and the final state interactions. Such a complete treatment of the inclusive $^4He(e,e'p)$ reaction is given in [18] and chapter 5 for the first time. In chapter 6, the consequences of the quasi-deuteron hypothesis ([42, 43, 44, 24, 45, 46, 13], and references therein) for experimental measurements are discussed and a new approximate universality of the missing momentum distributions for different target nuclei which is induced by the dominance and universal behaviour of final state interactions is presented.

Chapter 2

Final State Interaction at High Energies and High Momenta

The investigation of the momentum distribution of the nucleons inside the nucleus is a major goal of modern exclusive electron scattering experiments. The nucleon momentum distribution at higher momenta contains unique information on the short range nucleon-nucleon interaction in the medium. Currently there exist several predictions for the wave functions of light nuclei which include refined elements like short and long range correlations and even three-nucleon forces. The calculation of those wave functions demands a high numerical effort, and the research dedicated to the evaluation of realistic wave functions represents a large field of its own. The available predictions differ considerably. Even for the simplest nucleus, the deuteron, which consists only of two nucleons and can therefore be described, in principle, exactly, the predictions for higher momenta differ considerably, by almost one order of magnitude for the prediction for the Bonn meson exchange $N-N$ potential [25] and the Paris potential [26] (see Fig. 2.1). This difference gives an estimate of the uncertainties in the predictions of modern theories of the nucleon-nucleon interaction at large momenta $> 1.3 fm^{-1}$. The important question is how to distinguish between the different predictions *experimentally*.

2.1 $(e, e'p)$ in Plane Wave Impulse Approximation

If there were no final state interactions, exclusive electron scattering from nuclei would directly yield the necessary information, i.e. the nucleon momentum distribution inside the nucleus. A schematic diagram of the reaction is shown in Fig. 2.2. The electron exchanges a virtual photon with the nucleus. I assume Impulse Approximation, which means that the photon interacts with one nucleon only. In the

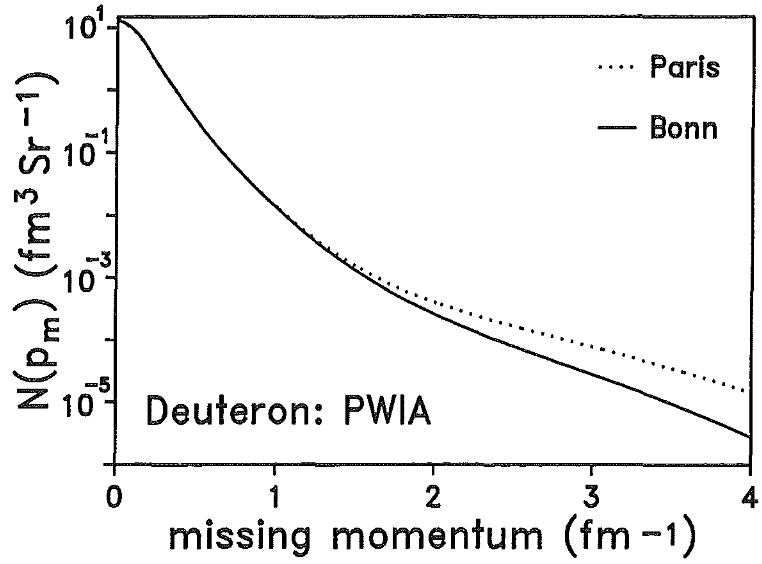

Figure 2.1: Predictions for the single particle momentum distribution of the deuteron calculated from the Bonn wave function [25] (solid line) and from the Paris wave function [26] (dotted line).

idealized case of Plane Wave Impulse Approximation(PWIA), this nucleon leaves the nucleus without any further interaction with the residual nucleus and is detected in coincidence with the scattered electron. In PWIA, the $A(e, e'p)$ coincidence cross section can be represented in the form

$$\frac{d\sigma^{PWIA}}{dQ^2 d\nu dp d\Omega_p} = K|M_{ep}|^2 S(E_m, \vec{p}_m). \tag{2.1}$$

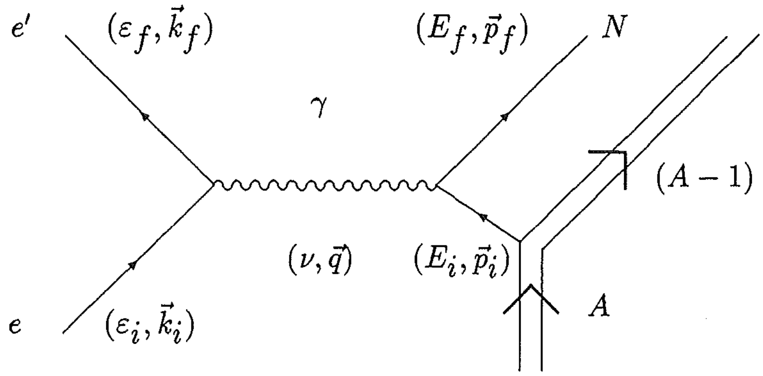

Figure 2.2: The reaction mechanism of the $A(e, e'p)$ reaction in Plane Wave Impulse Approximation.

Here K is a kinematical factor, M_{ep} is the ep elastic scattering amplitude, ν and $\vec{q}$ are the (e,e') energy and momentum transfer, $Q^2 = \vec{q}^{\,2} - \nu^2$, the struck proton has a momentum $\vec{p}$ and energy $E(p) = T_{kin} + m_p$, and the missing momentum and the missing energy are defined as $\vec{p}_m = \vec{q} - \vec{p}$ and $E_m = \nu + m_p - E(p) - T_{kin}(A-1)$ (where $T_{kin}(A-1)$ is the kinetic energy of the undetected $(A-1)$ residual system). Hereafter, the z-axis is chosen along the (e,e') momentum transfer $\vec{q}$. In PWIA, the missing momentum coincides with the negative initial nucleon momentum inside the target nucleus: $\vec{p}_m = -\vec{p}_i$. The spectral function $S(E_m, \vec{p}_m)$ gives the probability to find a nucleon with missing energy E_m and missing momentum p_m inside the nucleus. In an independent particle shell-model (IPSM) for the initial and final nuclear state the spectral function can be written as [11]

$$S(E_m, \vec{p}_m) = \sum_{\alpha} N_\alpha |\phi_\alpha(\vec{p}_m)|^2 \delta(E_m + \varepsilon_\alpha) \tag{2.2}$$

where $\phi_\alpha(\vec{p}_m)$ is the single-proton wave function in a given state α in momentum representation, ε_α the associated energy eigenvalue, and N_α the associated occupation number. The momentum distribution in the nucleus is now obtained by integration over the missing energy:

$$N(\vec{p}_m) = \frac{1}{(2\pi)^3} \int dE_m S(E_m, \vec{p}_m) = \frac{1}{(2\pi)^3} \sum_{\alpha} N_\alpha |\phi_\alpha(\vec{p}_m)|^2 . \tag{2.3}$$

However, in an actual experiment, there is always final state interaction present which spoils the simple picture of PWIA.

2.2 $(e, e'p)$ with Final State Interaction

In a realistic calculation, one has to take into account that the knocked out proton undergoes final state interaction with the residual system. A schematic picture of the reaction is shown in Fig. 2.3. As I want to concentrate on the effects of the final state interaction, I consider the longitudinal response for the sake of simplicity and treat the photon as a scalar operator. Then, the experimentally measured $A(e,e'p)$ coincidence cross section can again be represented in the form

$$\frac{d\sigma}{dQ^2 d\nu dp d\Omega_p} = K|M_{ep}|^2 S(E_m, \vec{p}_m, \vec{p}) \, , \tag{2.4}$$

where the spectral function also depends on the momentum of the knocked out nucleon, in contrast to the PWIA case. Note that the missing momentum $\vec{p}_m$ is not

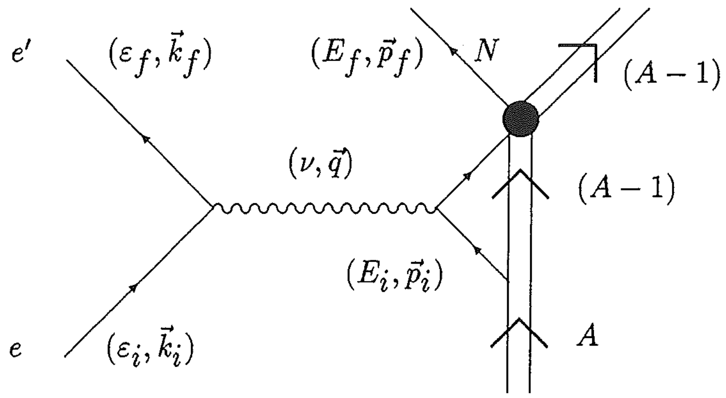

Figure 2.3: Reaction mechanism of the $A(e, e'p)$ reaction including final state interaction.

related in a simple way to the initial proton momentum as it is the case in PWIA. The validity of the factorization assumed in Eq. (2.4) is widely discussed in the literature [11, 47, 48]. In the present case of the longitudinal response only there is no problem with the factorization. Moreover, I will use only central forces in the final state interaction, so that the factorization assumption is valid for all parts of the response [11, 47]. The spectral function $S(E_m, \vec{p}_m, \vec{p})$ can be written in terms of the nuclear reduced amplitudes $\mathcal{M}_f$ as

$$S(E_m, \vec{p}_m, \vec{p}) = \sum_f |\mathcal{M}_f|^2 \delta(\nu + m_p - E(p) - E_m) . \tag{2.5}$$

For the longitudinal response, the reduced nuclear amplitude for the exclusive process $A_i(e, e'p)A_f$ equals

$$\begin{aligned} \mathcal{M}_f &= \int d\vec{R}_1 \ldots d\vec{R}_{A-1} \, \Psi_f^*(\vec{R}_1 \ldots \vec{R}_{A-2}) \\ & \hat{S}(\vec{r}_1, \ldots, \vec{r}_A) \, \exp(i\vec{p}_m \vec{R}_{A-1}) \, \Psi_i(\vec{R}_1, \ldots, \vec{R}_{A-1}) , \end{aligned} \tag{2.6}$$

where the initial nucleus contains A nucleons, Ψ_i is the wave function of the target nucleus and Ψ_f is the wave function of the $(A-1)$-body final state. Jacobi coordinates (see appendix A) are denoted by $\vec{R}_i$, laboratory coordinates $\{\vec{r}_i(\vec{R}_j, \vec{R}_{CM})\}$ are also used when appropriate. The specific expression Eq. (2.6) corresponds to the nucleon "A" chosen for the detected struck proton. In the derivation of Eq. (2.6) the center of mass motion was taken into account (and integrated over). This leads to the presence of $\vec{R}_{N-1}$ instead of $\vec{r}_N$ in the exponential. $\hat{S}(\vec{r}_1, ..., \vec{r}_N)$ stands for the S-matrix of the FSI of the struck proton with the spectator nucleons. The missing momentum distribution is obtained by integrating over the missing energy

E_m.

$$W(\vec{p}_m) = \frac{1}{(2\pi)^3}\int dE_m S(E_m,\vec{p}_m) = \frac{1}{(2\pi)^3}\sum_f |\mathcal{M}_f|^2 \,, \tag{2.7}$$

where the dependence on the momentum $\vec{p}$ of the struck proton was dropped for convenience. All numerical results presented later on are calculated for the fixed value $T_{kin}^{proton} = 1\,GeV$. If the initial state is not known, one has to average over all possible initial states in Eq. (2.7). Evidently, having high kinetic energy of the struck proton T_{kin} is important for reaching the interesting region of high missing momenta where the effects of the correlations are expected. This becomes possible for the first time in the CEBAF range of T_{kin}. Some examples for the kinematical range of different reactions are given in appendix B.

2.3 The Final State Interaction Operator

As the integration over the missing energy calls upon high kinetic energies of the proton, I concentrate on $T_{kin} \gtrsim 1 GeV$. The very nature of nucleon-nucleon interaction changes from the purely elastic potential scattering at low energies to a strongly absorptive, diffractive small angle scattering at $T_{kin} \gtrsim 0.5 - 1\,GeV$. E.g., a typical value for the total elastic $N-N$ cross section is $\sigma_{el} \approx 10mb$ and for the inelastic cross section $\sigma_{in} \approx 30mb$, which clearly shows the dominance of the absorption at the considered high kinetic energies. This is also borne out by the ratio ρ of the real to the imaginary part of the forward elastic scattering amplitude, which takes the values $\rho \approx -0.2$ for $p-p$ scattering and $\rho \approx -0.4$ for $p-n$ scattering [49]. In this high energy regime, the Compton wavelength of the struck proton is much smaller than the size of a nucleon and/or average nucleon-nucleon separation in nuclei. The Glauber model [19, 20] becomes a natural framework for quantitative description of FSI.

The Glauber formalism describes quite well nucleon-nucleus scattering at energies above $500\,MeV$, even at angles as large as 30^o at $500\,MeV$ (for a review see [40]). A thorough test of the Glauber theory in the scattering of $2\,GeV$ polarized deuterons on protons has been performed in [50], higher energy data on elastic *pd* scattering are discussed in [51]. In [52] the Watson multiple scattering series is expanded to develop the Glauber approximation plus corrections arising from three effects: 1) deviations from eikonal propagation between scatterings, 2) Fermi motion of struck nucleons, and 3) the kinematic transformation which relates the many-body scattering operators of the Watson series to the physical two-body scattering amplitude. An important finding of [52] is that the eikonal, Fermi motion and kinematic corrections substantially cancel each other. Hence the Glauber approximation is more accurate than that corrected for one of those effects (see also the review [40]).

Before the Glauber formalism is explained in quantitative terms, some remarks about the general features of final state interaction at high energies are in order. In the simplest case of $(e, e'p)$ on the deuteron, we have the interaction of the fast proton with the neutron. After the interaction of the photon and the proton in the hard vertex, the proton carries in good approximation the momentum $\vec{q}$ of the photon, the comparatively small initial momentum of the proton can be neglected. Final state interaction can only take place if the neutron is in the forward hemisphere with regard to the proton. In this case, due to the diffractive nature of the nucleon-nucleon interaction at the considered high energies, either the proton is absorbed, i.e. the process does not contribute to the considered elastic channel of the $(e, e'p)$ reaction, or it is only slightly deflected in transverse direction. This slight deflection in transverse direction is a dynamical effect due to the diffractive nature of the interaction. This deflection is present in the CM system of the proton and spectator nucleon, it is not a mere kinematical effect in the laboratory system. The reaction is sketched in Fig. 2.4a. The deflection of the proton in transverse direction leads to a difference between its momentum before the final state interaction took place and its momentum afterwards which is most likely perpendicular to the z-direction: $\vec{q} - \vec{p} := \vec{p}_m \perp z$. The missing momentum $\vec{p}_m$ arises from the final state interaction and does not contain any information on the initial nucleon momenta. The missing momentum generated in this way is usually large due to the short ranged nature of the final state interaction. If one plots the distribution of the missing momentum distribution against the angle θ between the missing momentum $\vec{p}_m$ and the z-axis, one expects from this simple intuitive consideration a large peak around $\theta = 90^o$. This distribution is sketched in Fig. 2.4b and it shows up again in the numerical results presented in the following chapters.

After having established a physical understanding for the properties of final state interactions at high energies, it is easy to understand how those features are reflected in the framework of the Glauber theory. For a detailed presentation of Glauber theory and its applications to proton-nucleus scattering, see [19, 20, 40, 52]. The

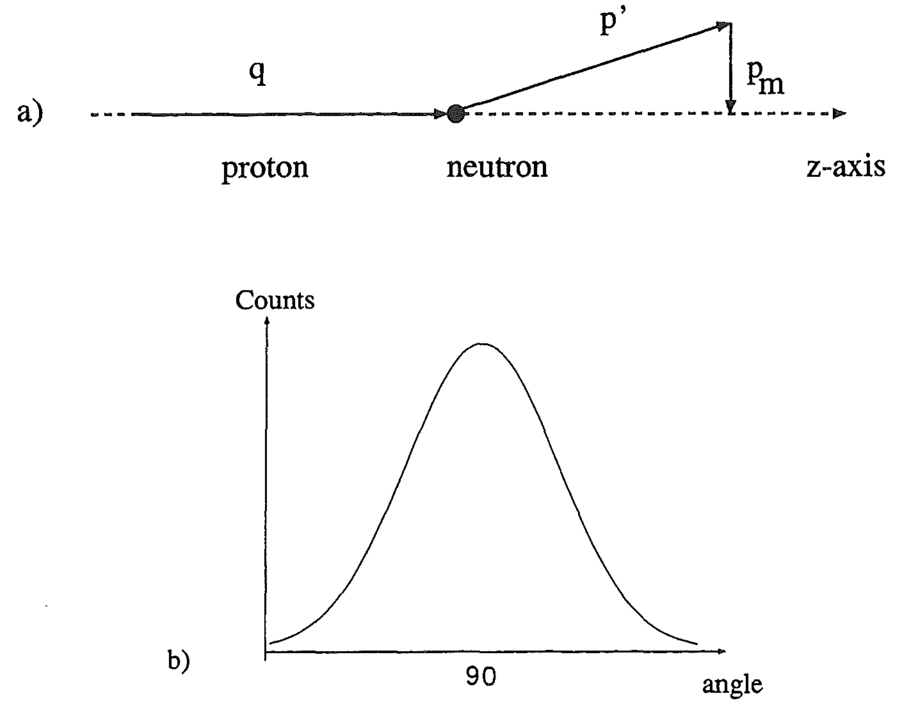

Figure 2.4: Panel a) shows the kinematics of the final state interaction at high energies, and panel b) sketches the expected missing momentum distribution plotted against the angle θ of the missing momentum with the z axis.

final state interaction operator for the exclusive process $A_i(e, e'p)A_f$ reads

$$\hat{S}(\vec{r}_1, \ldots, \vec{r}_A) = \prod_{i=1}^{A-1} \left[1 - \theta(z_i - z_A)\,\Gamma(\vec{b}_A - \vec{b}_i)\right] \tag{2.8}$$

where the decomposition of the coordinate vector into transverse part $\vec{b}$ and longitudinal part z was used: $\vec{r} = (\vec{b}, z)$ and the nucleon "A" was chosen as the struck proton. The profile function of the pN interaction, $\Gamma(\vec{b})$, is related to the proton-nucleon scattering amplitude f by the inverse Fourier transform

$$\Gamma(\vec{b}) = \frac{1}{2\pi ik} \int \exp(-i\vec{q}\cdot\vec{b})\, f(\vec{q}) d^2\vec{q}, \tag{2.9}$$

where $\vec{q} = \vec{k} - \vec{k}'$, and $\vec{k}$ and $\vec{k}'$ are the initial and final momenta of the incident proton. The proton-nucleon scattering amplitude at high energy and small angles can be parameterized as

$$f(\vec{q}) = f(0)\, \exp(-\frac{1}{2} b_o^2 \vec{q}^2) \tag{2.10}$$

with $f(0) = (i+\rho)\frac{k\sigma_{tot}}{4\pi}$ which leads to the profile function

$$\Gamma(\vec{b}) \;=\; \frac{\sigma_{tot}(1-i\rho)}{4\pi b_o^2}\exp\Big(-\frac{\vec{b}^2}{2b_o^2}\Big)\,. \tag{2.11}$$

Here ρ is the real to imaginary ratio for the forward elastic pN scattering amplitude, b_o^2 is the diffraction slope. In the GeV energy range, $\sigma_{tot} \approx 40mb$, $\rho \approx (-0.2) - (-0.4)$, $b_o \approx 0.5fm$ [53, 54, 55, 56, 49]. Those parameters have only a very slight energy dependence in the GeV energy range. In the numerical calculations, I use the values appropriate for $T_{kin} = 1\,GeV$ for the sake of definiteness, but for higher energies, the results hardly change at all. The θ-function in the operator (2.8) implies that the final state interaction is possible only provided that the spectator nucleon was in the forward hemisphere with respect to the struck proton. The form of $\Gamma(\vec{b})$ tells that the struck proton wave is distorted only at small $|\vec{b}| \lesssim b_o$. This means that the FSI operator $\hat{S}$ is short ranged in the transverse direction and long-ranged in the longitudinal direction. Here, long ranged indicates a distance on the scale of the nuclear radius R_A, and short ranged indicates a distance on the scale of the diffraction slope b_o and/or the nucleon-nucleon correlation radius r_c.

Because ρ is small, $\Gamma(\vec{b})$ is dominated by the imaginary part of the p-n elastic scattering amplitude and the distortion factor $\hat{S}$ predominantly gives an absorption of the struck proton wave at small $\vec{b}$. At lower energies, the term "inelastic event" indicates that the target nucleus breaks up, whereas at the considered high four-momentum transfer $(e, e'p)$ experiments, "inelastic" means that the proton breaks up when undergoing FSI with the residual nucleus. The fact that ρ is small and $\sigma_{el} < \sigma_{in}$ means that those inelastic events are dominating at GeV energies.

In contrast to FSI at low energies, which is S-wave dominated and therefore isotropic, the above basic properties of FSI at high energies demonstrate that the transverse and longitudinal directions, and the forward and backward hemisphere, have different roles, with the phenomenological consequences of a marked angular anisotropy, and forward-backward asymmetry.

In my calculation, I use the central part of the nucleon-nucleon scattering amplitude. The contribution of its spin-orbit part is small [40].

Although Glauber has originally derived his formalism in a non-relativistic framework, the high energy approximation of Glauber does not depend upon the existence of a potential. There exists extensive literature on the field theoretic derivation of the Glauber approximation for particle-particle scattering [57, 58, 59, 60]. It can be obtained in the high energy limit of a general expansion of the scattering amplitudes [57]. For hadron-nucleus scattering, a field theoretical rederivation of Glauber's formulas was given for the first time by Gribov [61]. It is important that Glauber's S-matrix for hadron-nucleus interactions only contains the free nucleon-nucleon scattering amplitudes, which can be seen from Eq. (2.9). An additional correction to $A(e, e'p)$ scattering and to quasi-elastic scattering in general originates from the slight loss of energy of the struck proton due to the recoil energy. Its effects in proton-nucleus scattering were investigated in [62] and found to be small. The main effect of this correction for $A(e, e'p)$ scattering is a slight shift of the peak in perpendicular kinematics. The concern of this thesis is a comparison of the final state interaction and short range correlation effects, this contribution is neglected here.

In this thesis, I neglect the intermediate isobar states, because their effect is very small: at the considered energies, the inelastic proton-proton cross section is exhausted by the reaction $pp \longrightarrow p\Delta$, so the Δ is the only candidate for the intermediate isobar state. If the Δ is produced in the hard vertex, it has to decay by the process $\Delta n \longrightarrow pn$, but this process where a pion is exchanged has a real amplitude and therefore its interference with the predominantly imaginary amplitude of the process $pn \longrightarrow pn$ is negligible.

The effect of meson exchange currents at lower energies amounts up to approximately 10% of the transverse response function, it is much smaller in the other parts of the response. At the high energy transfers considered here, there exists no mechanism that would allow to transfer this high energy that the meson receives from the photon to the proton. As I consider the $(e, e'p)$ reaction for kinetic energies of $1\,GeV$, meson exchange current contributions are negligibly small.

Chapter 3

Electron Scattering on Unpolarized Deuterons

The deuteron, which consists of one proton and one neutron, is the simplest nucleus and has a special role due to the fact that the two-body problem can, in principle, be solved exactly. Starting from different models for the nucleon-nucleon interaction [25, 26] the deuteron wave function, the binding energy and the quadrupole moment of the deuteron have been calculated. The various models differ considerably in their predictions of the D-wave content. It is therefore an important question if it is possible to get direct information on the deuteron ground state wave function by performing $^{2}He(e,e'p)n$ experiments, and if this information will allow to check and distinguish between the predictions of the different models. In this thesis, the Bonn and Paris predictions for the deuteron wave function will be compared. There are also other models [27, 28], but their results are in agreement within $20-30\%$ with the Paris predictions. The Bonn model results differ considerably from the other group of models due to the smaller D-wave content. Therefore, the Bonn and Paris models are suitable representatives for the present investigation, the use of another model will not yield different insight into the problem.

For the deuteron, one cannot distinguish between the influence of the "mean field" and the effects of nucleon-nucleon correlations, as there are only two nucleons present in the nucleus. The nuclear correlations are already contained in the S- and D-radial wave functions.

As realistic parameterizations of the wave function are available, no assumptions about the wave function are necessary and therefore the deuteron is very well suited for the exploration of final state interaction effects. The results of this chapter have been published in [14].

3.1 The Deuteron Wave Function

The deuteron has total angular momentum $J = 1$ and positive parity. The deuteron wave function contains S-wave and D-wave, which are coupled to $J = 1$ and the three possible values for J_z with the corresponding spin eigenstates. The wave functions for $J_z = \pm, 0$ are:

$$\begin{aligned}\Psi_+ &= \Big(\frac{u(r)}{r}Y_{00}(\hat{r}) + \sqrt{\frac{1}{10}}\frac{w(r)}{r}Y_{20}(\hat{r})\Big)|1\rangle \\ &-\sqrt{\frac{3}{10}}\frac{w(r)}{r}Y_{21}(\hat{r})|0\rangle + \sqrt{\frac{3}{5}}\frac{w(r)}{r}Y_{22}(\hat{r})|-1\rangle\end{aligned} \tag{3.1}$$

$$\begin{aligned}\Psi_0 &= \Big(\frac{u(r)}{r}Y_{00}(\hat{r}) - \sqrt{\frac{2}{5}}\frac{w(r)}{r}Y_{20}(\hat{r})\Big)|0\rangle \\ &+\sqrt{\frac{3}{10}}\frac{w(r)}{r}Y_{2-1}(\hat{r})|1\rangle + \sqrt{\frac{3}{10}}\frac{w(r)}{r}Y_{21}(\hat{r})|-1\rangle\end{aligned} \tag{3.2}$$

$$\begin{aligned}\Psi_+ &= \Big(\frac{u(r)}{r}Y_{00}(\hat{r}) + \sqrt{\frac{1}{10}}\frac{w(r)}{r}Y_{20}(\hat{r})\Big)|-1\rangle \\ &+\sqrt{\frac{3}{5}}\frac{w(r)}{r}Y_{2-2}(\hat{r})|1\rangle - \sqrt{\frac{3}{10}}\frac{w(r)}{r}Y_{2-1}(\hat{r})|0\rangle\end{aligned} \tag{3.3}$$

Here, $|\sigma\rangle$ stands for the initial triplet spin wave function with the projection $\sigma = 0, \pm 1$.

3.2 The Missing Momentum Distribution

The reduced nuclear amplitude for the exclusive process $D(e, e'p)n$ is given by

$$\mathcal{M}_{ji} = \int d^3\vec{r}\exp(-i\vec{p}_m\vec{r})\chi_j^* S(\vec{r})\Psi_i(\vec{r}) \tag{3.4}$$

where $\vec{r} \equiv \vec{r}_n - \vec{r}_p$, $\Psi_i(\vec{r})$ is the deuteron wave function for the spin state i (see section 3.1) and χ_j stands for the spin wave function of the final pn state. For unpolarized deuterons and for a spin-independent proton-neutron scattering amplitude, one finds the observed momentum distribution by averaging over the three possible initial states and summing over the final states

$$\begin{aligned}W(\vec{p}_m) &= \frac{1}{3}\sum_{j,i}|M_{ji}|^2 = \frac{1}{4\pi(2\pi)^3}\int d^3\vec{r}d^3\vec{r}\,'\exp[i\vec{p}_m\cdot(\vec{r}\,'-\vec{r})]S(\vec{r})S^\dagger(\vec{r}\,') \\ &\left[\frac{u(r)}{r}\frac{u(r')}{r'} + \frac{1}{2}\frac{w(r)}{r}\frac{w(r')}{r'}\left(3\frac{(\vec{r}\cdot\vec{r}\,')^2}{(rr')^2} - 1\right)\right],\end{aligned} \tag{3.5}$$

where u/r and w/r are the S and D-wave radial wave functions of the deuteron, with the normalization $\int dr(u^2 + w^2) = 1$. This normalization leads automatically to the correct normalization of the missing momentum distribution in PWIA:

$$\int d^3\vec{p}_m N(\vec{p}_m) = 1\,, \tag{3.6}$$

where we have denoted the missing momentum distribution in PWIA by N, i.e. $W^{PWIA}(\vec{p}_m) = N(\vec{p}_m)$. This notation is used throughout this text. Note that for unpolarized deuterons and a spin-independent final state interaction of proton and neutron the S- and D-wave do not interfere, as can clearly be seen from Eq. (3.5).

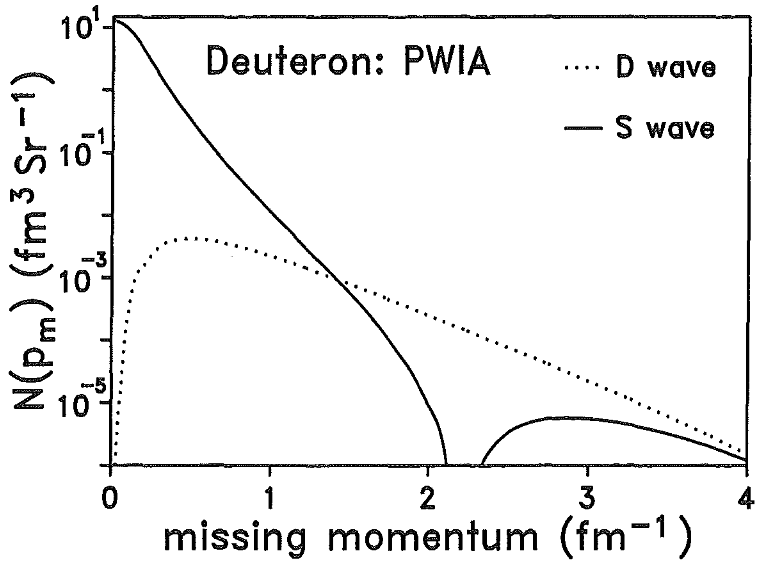

Figure 3.1: The S-wave (solid line) and D-wave contributions to the PWIA missing momentum distribution $N(p_m)$ calculated with the Bonn wave function.

In PWIA, the S-matrix of FSI reduces to $S(\vec{r}) = 1$. Then we obtain a completely isotropic missing momentum distribution:

$$N(\vec{p}_m) = N(p_m)\,. \tag{3.7}$$

In Fig. 3.1 the missing momentum distribution in PWIA is decomposed into the S- and D-wave contributions. Here, the Bonn wave function was used and if not stated otherwise, the numerical results in this thesis have been obtained with the Bonn potential. The interesting dip structure will be discussed in the chapter on electron scattering on tensor polarized deuterons. At higher missing momenta, $p_m \gtrsim 1.5 fm^{-1}$, the distribution is dominated by the D-wave contribution. This causes the discrepancy between the predictions of the Bonn and Paris models as shown in Fig. 2.1: the D-wave content of the models is different. Therefore, an experiment that yields information on the high momentum part of the single particle momentum distribution $N(p_m)$ is necessary to discriminate between the different models.

For electron scattering on deuteron, the final state interaction operator S as given in Eq. (2.8) simplifies to

$$S(\vec{r}) = 1 - \theta(z)\,\Gamma(\vec{b})\,, \tag{3.8}$$

where $\vec{r} = \vec{b} + \hat{q}z$. The profile function $\Gamma(\vec{b})$ as given in Eq. (2.11) is a short ranged operator of the transverse separation $\vec{b}$, as the diffraction slope $b_o = 0.5fm$ is much smaller than the deuteron radius $R_D \approx 2fm$. In contrast, the θ-function is a long ranged function of the longitudinal separation. Therefore, the product $S(\vec{r})\,S^{\dagger}(\vec{r}\,')$ introduces a marked angular anisotropy in the integrand of the observed missing momentum distribution and into the missing momentum distribution $W(\vec{p}_m)$ itself.

In Fig. 3.2, the solid line shows the angular distribution of $W(\vec{p}_m)$ and for comparison, the isotropic PWIA distribution is included as the dotted line. In the different panels, the angular distribution is shown for different moduli of the missing momentum. The angular distribution of the missing momentum distribution $W(\vec{p}_m)$ has several interesting features: i) Even for momenta as low as $1fm^{-1}$, there is a distinct anisotropy present. ii) In all cases, the calculation including FSI differs considerably from the one in PWIA. iii) For missing momenta larger than $1.75fm^{-1}$, $W(\vec{p}_m)$ shows clearly a prominent peak at $\theta = 90^o$ degree. It evolves through a very asymmetric stage to an approximately symmetric peak at 90^o at larger values of p_m. This peak is due to the diffractive character of the final state interaction and was already discussed qualitatively in section 2.3. Its presence is a clear sign of the dominance of the final state interaction for intermediate and large missing momenta. iv) The missing momentum distribution shows a striking forward-backward asymmetry: $W(p_{\perp}, -p_z) \neq W(p_{\perp}, p_z)$ (where the missing momentum was decomposed as follows: $\vec{p}_m = p_{\perp} + p_z\hat{q}$), which has its origin in the nonvanishing real part of the $p-n$ scattering amplitude $\rho \neq 0$, leading to $S(\vec{b}, z)S^{\dagger}(\vec{b}', z') \neq S(\vec{b}', z')S^{\dagger}(\vec{b}, z)$ in the integrand of Eq. (3.5). In fact, it is proportional to ρ.

It is important to see if the dominance of the D-wave at $p_m > 1.5fm^{-1}$ survives the final state interaction. In Fig. 3.3 the angular dependence of the missing momentum distribution $W(\vec{p}_m)$ (solid line) and of its S-wave (dotted line) and D-wave (dashed line) components are shown for different values of the missing momentum

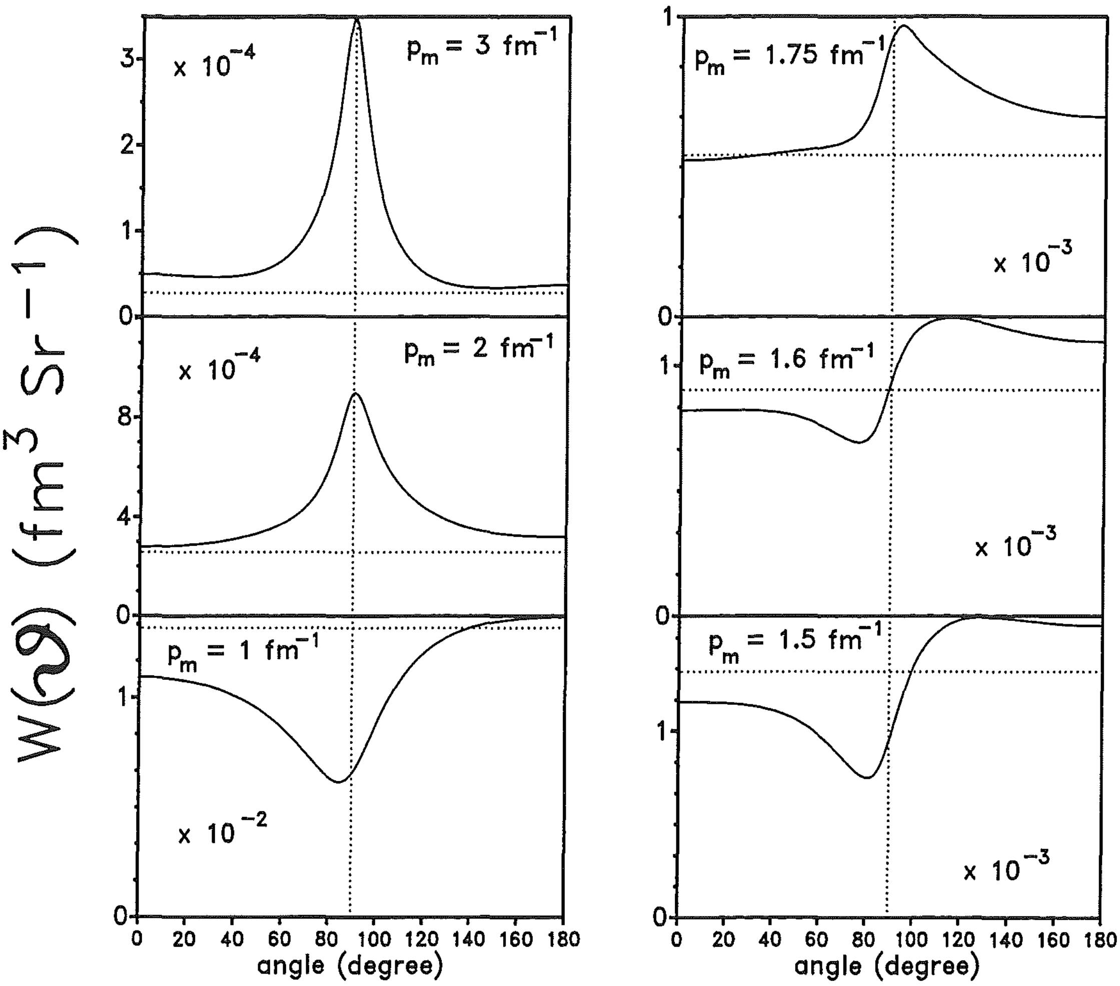

Figure 3.2: The angular dependence of the missing momentum distribution $W(\vec{p}_m)$ including FSI effects (solid line) and of the PWIA missing momentum distribution $N(p_m)$ (dotted line).

p_m. The D-wave contribution is only very slightly distorted, it is almost isotropic. The S-wave shows a distinct angular anisotropy and, at higher missing momenta, builds up the peak at $\theta = 90^o$. In contrast to the PWIA, the S-wave now dominates for higher missing momenta in perpendicular kinematics, i.e. at $\theta = 90^o$.

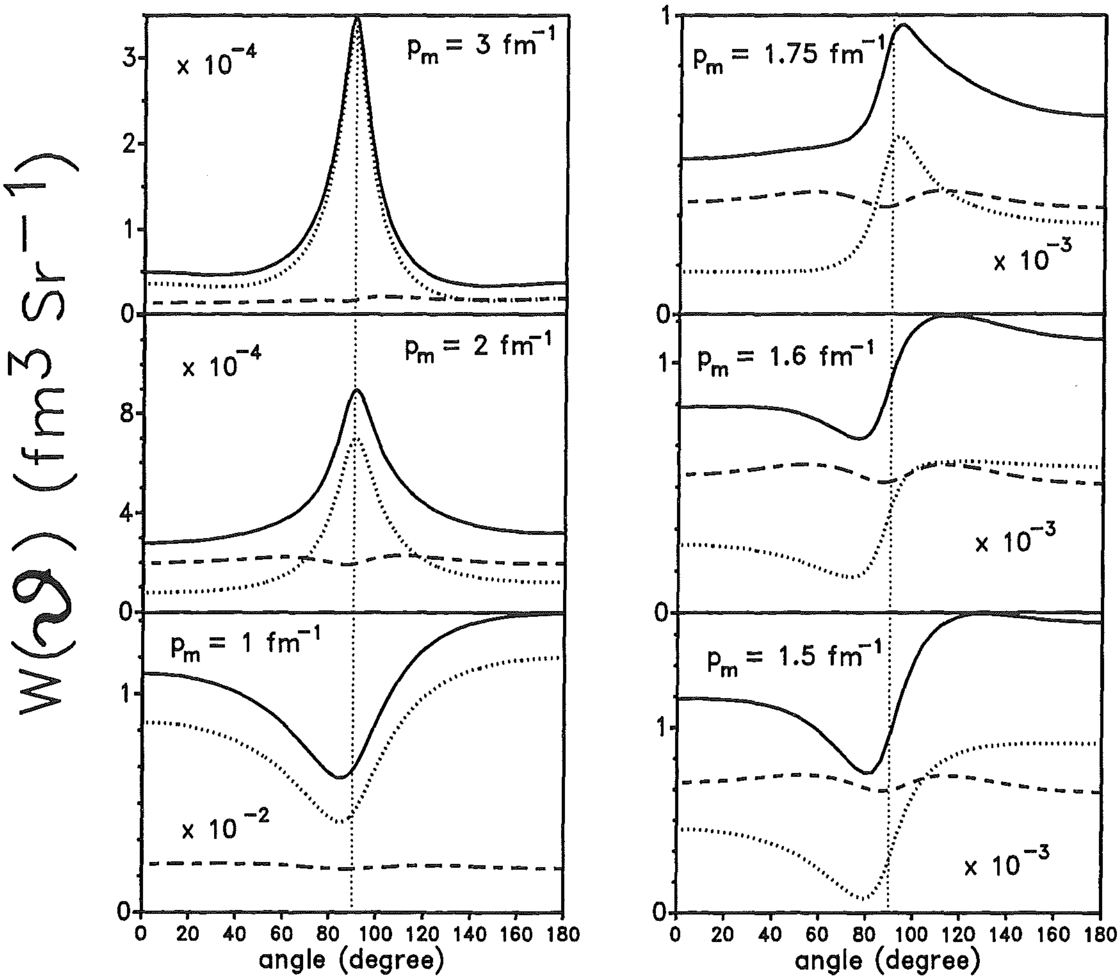

Figure 3.3: The angular dependence of the missing momentum distribution $W(\vec{p}_m)$ (solid line) and of its S-wave (dotted line) and D-wave (dashed line) components at different values of the missing momentum p_m.

This behaviour of the D-wave contribution can be easily understood: the fact that $\Gamma(\vec{b})$ is a short ranged function, whereas the D-wave is strongly suppressed at short distances by the centrifugal barrier, implies that FSI effects in the D-wave contribution to $W(\vec{p}_m)$ should be much weaker than in the S-wave contribution.

In Fig. 3.4, the missing momentum distribution $W(\vec{p}_m)$ and several of its com-

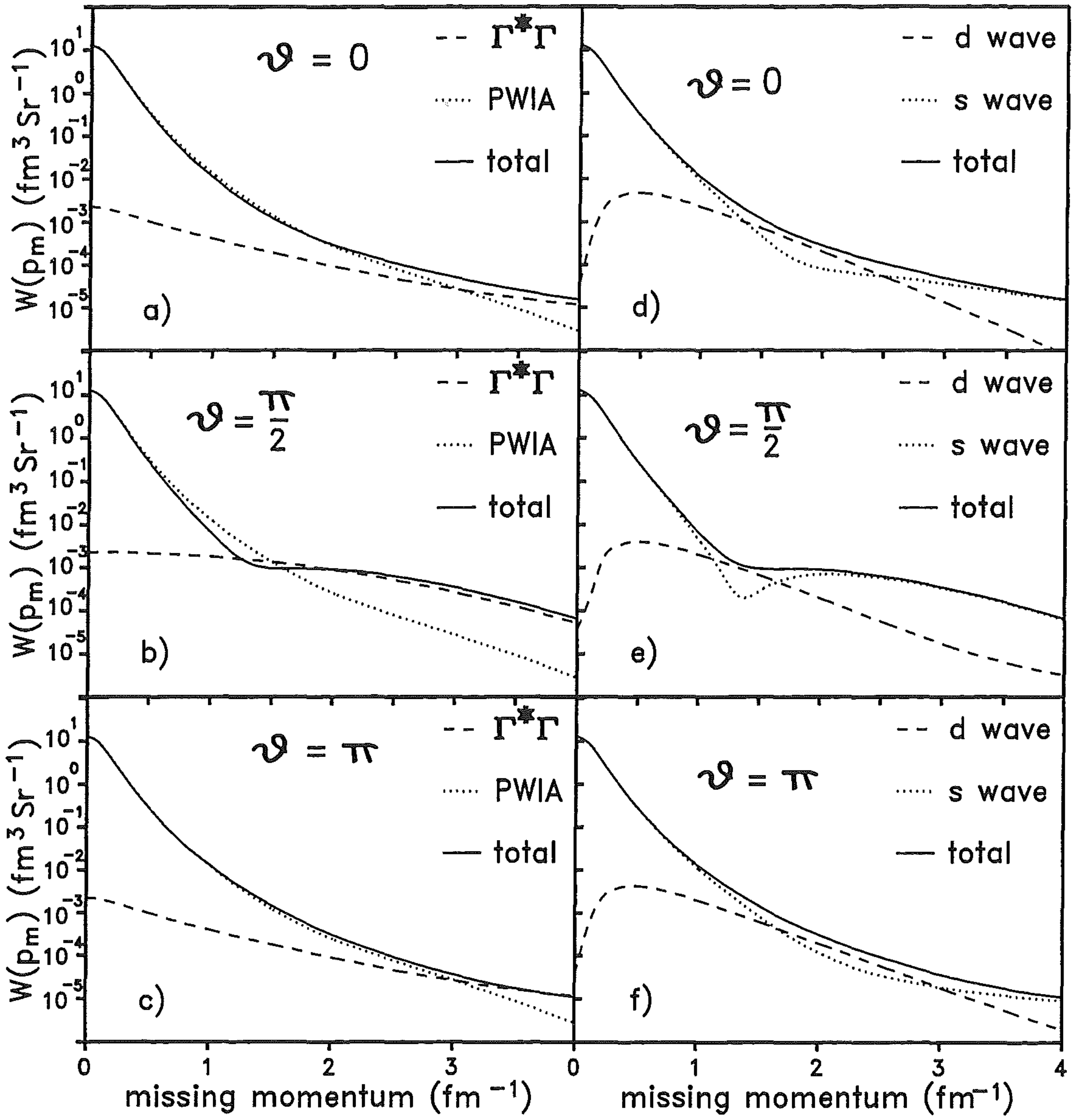

Figure 3.4: The missing momentum distribution $W(\vec{p}_m)$ *vs.* p_m and its decomposition into *(a-c)* the PWIA and the rescattering contributions $\propto \Gamma^*\Gamma$ and into *(d-f)* the S- and D-wave contributions at *(a,d)* $\theta = 0^o$, *(b,e)* $\theta = 90^o$ and *(c,f)* $\theta = 180^o$. In panels *(a-c)* the full distribution $W(\vec{p}_m)$ (solid curve) includes also the contribution $\propto (\Gamma^* + \Gamma)$ from the interference of the PWIA and FSI amplitudes, which is not shown separately.

ponents are plotted versus p_m for parallel (i.e. $\theta = 0^o$), antiparallel (i.e. $\theta = 180^o$) and perpendicular kinematics. Figs. 3.4d-f show the decomposition into S-wave (dotted line) and D-wave (dashed line) contribution. Again, one sees clearly that the S-wave dominates in perpendicular kinematics and contributes significantly in (anti)parallel kinematics. The D-wave is still an important contribution in (anti)parallel kinematics, although it is not as dominant as in the PWIA distribution for higher missing momenta. The S-wave contribution can conveniently be written as $W_S(\vec{p}_m) = 2^{-5}\pi^{-4}U^2(\vec{p}_m)$, where

$$U(\vec{p}_m) = \int d^3\vec{r}\exp(-i\vec{p}_m\cdot\vec{r})S(\vec{r})\frac{u(r)}{r} = u(1;\vec{p}_m) - u(\Gamma;\vec{p}_m) \tag{3.9}$$

The PWIA term $u(1;\vec{p}_m)$ in (3.9) decreases on the scale $p_\perp, p_z \sim 1/R_D$. In view of $b_0^2 \ll R_D^2$, the FSI term $u(\Gamma;\vec{p}_m)$ has a $p_\perp$ dependence $\sim \exp(-\frac{1}{2}b_0^2p_\perp^2)$ and at moderately large p_z it decreases on the scale $p_z \sim 1/R_D$. It has the absolute normalization $\sim \sigma_{tot}(pn)/(2\pi R_D^2) = 0.16$ [15, 63]. The destructive interference of the PWIA and FSI amplitudes produces a dip in the S-wave contribution at $p_\perp \sim 1.3\,\mathrm{fm}^{-1}$ as shown in Fig. 3.4e, which is partly filled by the effect of the finite ρ.

Fig. 3.4b shows the PWIA-FSI decomposition of the $\theta = 90^o$ distribution. Shown by the dotted curve is the PWIA distribution, the dashed curve shows the pure rescattering contribution $\propto \Gamma^*\Gamma$ in Eq. (3.5). The term $\propto (\Gamma + \Gamma^*)$ from interference of the FSI and PWIA amplitudes, not shown separately here, is given by the difference between the solid curve and the sum of the dashed and dotted curves and is most significant around $p_m \sim 1.5\,fm^{-1}$. The sharp peak at $\theta = 90^o$, which emerges at $p_m \gtrsim 1.7\,fm^{-1}$, is a pure FSI (elastic p-n rescattering) effect.

Fig. 3.4a,c show that for $p_m \gtrsim 1.5\,fm^{-1}$, FSI effects are substantial also in parallel kinematics. Here the most interesting effect first noticed in [15], is the emergence of forward and backward peaks in $W(p_m)$ with increasing p_m as shown in Fig. 3.5. In Figs. 3.4a,c, the same effect shows up as the FSI component overwhelming the PWIA component at $p_m \gtrsim 3\,fm^{-1}$. The origin of this phenomenon is in the high-frequency Fourier components of the step-function $\theta(z)$ in the integrands of (3.5,3.9). The dominant effect comes from the "elastic rescattering" operator $\theta(z)\theta(z')\Gamma(b)\Gamma^*(b')$ in the integrand of (3.5), and Fig. 3.4c shows that the excess over the PWIA curve in antiparallel kinematics at $p_m \gtrsim 3\,fm^{-1}$ is entirely due to the contribution from the term $\propto \Gamma^*\Gamma$. In parallel kinematics, the excess over the PWIA curve is mainly due to the term $\propto \Gamma^*\Gamma$ together with a smaller contribution from the terms $\propto (\Gamma^* + \Gamma)$ from the interference of the PWIA and FSI amplitudes, which are not shown sep-

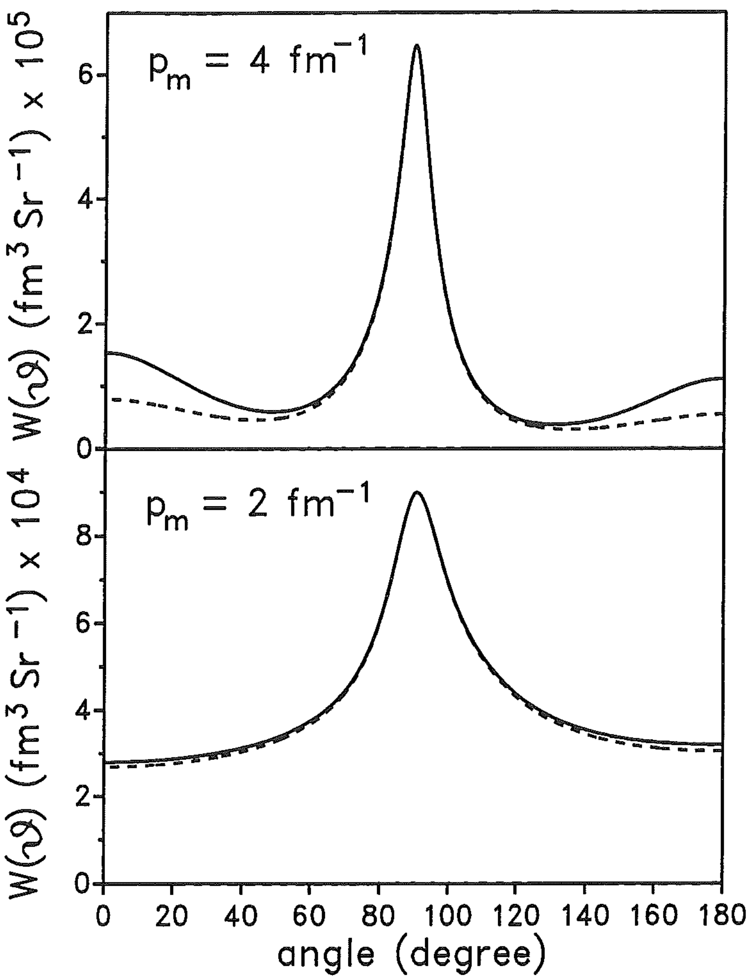

Figure 3.5: The angular dependence of the missing momentum distribution $W(\vec{p}_m)$ (solid line) showing the development of the forward and backward peaks at $p_m = 2\,fm^{-1}$ (lower panel) and at $p_m = 4\,fm^{-1}$ (upper panel). The dashed curve shows $W(\vec{p}_m)$ found with the smeared step-function $T(z)$ of Eq. (3.10) with $z_0 = 0.25\,fm$.

arately in the figure. The scale for the intra-nucleon separation at which nucleons can still be treated as approximately structure-less particles interacting with the free-nucleon amplitude, is set by the radius of the nucleon and/or the short-range correlation radius $r_c \sim 0.5\,fm$. The effect of the non-pointlike nucleons can be modeled substituting the idealized step-function $\theta(z)$ for the smeared one

$$T(z) \equiv \frac{1}{2}[1 + \tanh(\frac{z}{z_0})]. \tag{3.10}$$

The educated guess is $z_0 \lesssim \frac{1}{2}r_c$. In Fig. 3.5 I show the effect of smearing for $z_0 = \frac{1}{2}r_c = 0.25\,fm$. Uncertainties with the smearing do evidently persist at high

Q^2. They are small at least up to $p_m \lesssim 3\, fm^{-1}$, treatment of higher p_m requires new approaches which go beyond the Glauber model.

As far as the applicability of Glauber's multiple scattering theory is concerned, this is an entirely new situation and shows that the Glauber treatment of FSI in $A(e,e'p)$ scattering is not fully self-contained at large longitudinal missing momenta. The Glauber theory description of the proton-nucleus elastic scattering is very accurate [50, 51, 40], but in the pA scattering one has the well defined asymptotic $|in\rangle$ and $|out\rangle$ proton states, whereas in FSI in the $D(e,e'p)$ scattering the incoming proton wave is generated at a finite distance from the target neutron. When this distance becomes of the order of the radius of nucleons, one can not describe the distortion of the wave function of the spectator neutron by formula (3.8) with the idealized step-function.

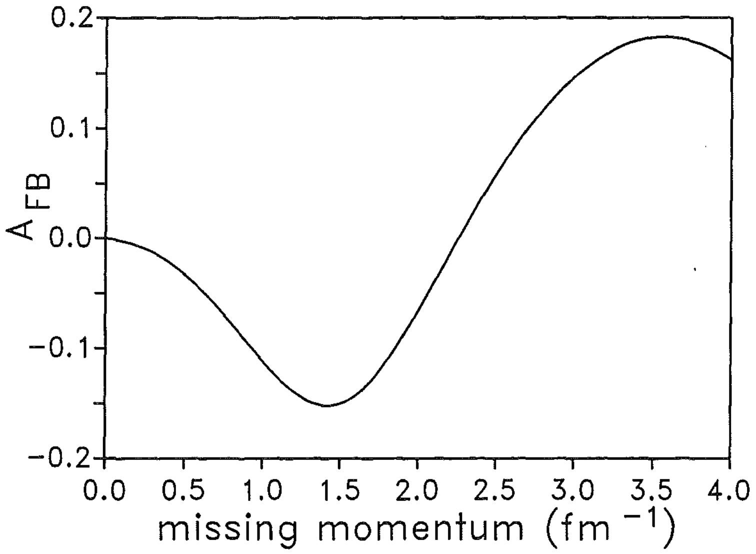

Figure 3.6: The p_m dependence of the forward-backward asymmetry A_{FB} in parallel kinematics.

The FSI-induced forward-backward asymmetry in parallel kinematics

$$A_{FB} = \frac{W(\theta = 0^o, p_m) - W(\theta = 180^o, p_m)}{W(\theta = 0^o, p_m) + W(\theta = 180^o, p_m)} \tag{3.11}$$

is shown in Fig. 3.6. The asymmetry A_{FB} is large and should be taken into account when looking for the forward-backward asymmetry which is expected at higher Q^2 because of the colour transparency effect [36, 37, 38] (see also a discussion in [64]).

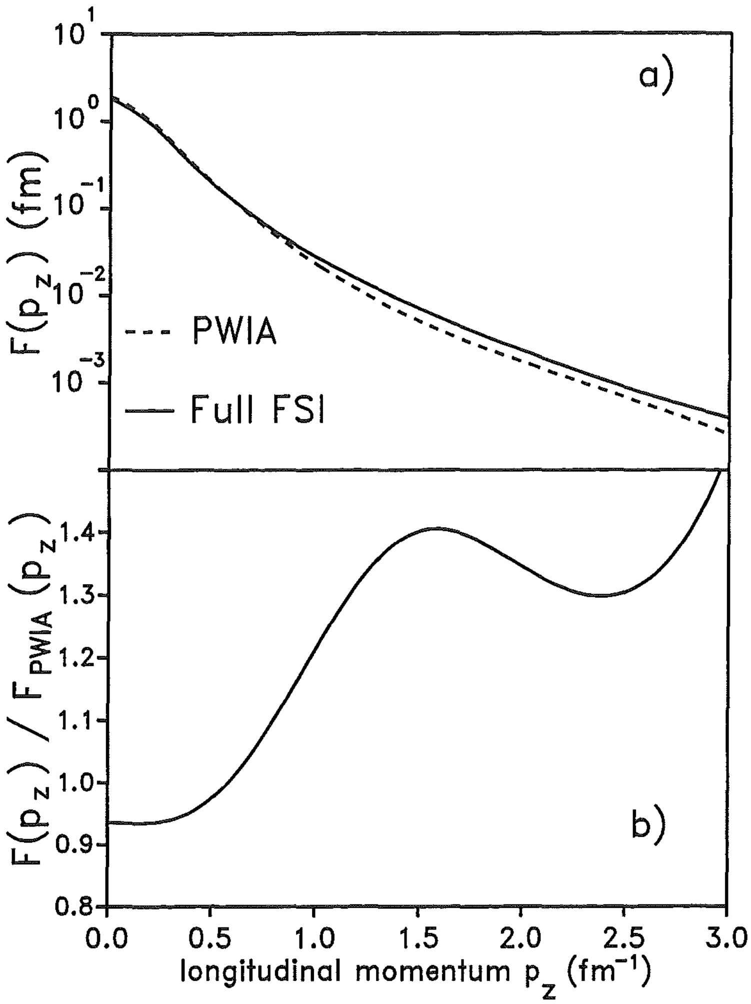

Figure 3.7: *(a)* The longitudinal missing momentum distribution $F(p_z)$ calculated with full FSI (solid curve) and in the PWIA (dashed curve). *(b)* The ratio of the full $F(p_z)$ to the PWIA distribution $F_{PWIA}(p_z)$.

Still another interesting quantity is the $p_\perp$-integrated, longitudinal missing momentum distribution

$$F(p_z) \equiv \int d^2\vec{p}_\perp W(\vec{p}_\perp, p_z)\,. \tag{3.12}$$

In the PWIA, $F_{PWIA}(p_z) = \int d^2\vec{p}_\perp n(p_\perp, y)$ is related to the asymptotic y-scaling function [65, 66]. In Fig. 3.7 we show the ratio $R(p_z) = F(p_z)/F_{PWIA}(p_z)$. At small p_z, the reduction of the flux of protons due to the absorption by the neutron leads to a depletion $\sim 7\%$ in agreement with the estimate [63] and the NE18 experimental finding [67, 68, 69]. At larger $p_z \gtrsim 1.2\, fm^{-1}$, the contribution $\propto \Gamma\Gamma^*$ from FSI enhances $F(p_z)$ by $\sim$(30-40)% as compared to the PWIA distribution $F_{PWIA}(p_z)$.

At larger Q^2 and higher kinetic energies of the proton, $T_{kin} \gtrsim 1\,GeV$, the proton-neutron total cross section is approximately constant [49]. Therefore, this large FSI effect in $F(p_z)$ should persist at large $Q^2 \gg 1\,GeV^2$ and should be taken into account in the asymptotic y-scaling regime, too. However, one has to be careful in transferring those results to the y-scaling regime, as the data analyzed there have been taken in a different kinematic setting of high Q^2 but very small transferred energy ν [70], in contrast to our situation where the transferred energy takes values of several hundred MeV (see appendix B). The departure from the PWIA further increases at $p_z \gtrsim 3\,fm^{-1}$, but the quantitative description of FSI in this region of p_m requires improving upon the Glauber approach, which goes beyond the scope of this thesis.

3.3 Uncertainties due to the Employed Parameters

As was already mentioned in section 2.3, the Glauber model is well tested in the calculation of proton-nucleus scattering and attempts to include only one correction to the Glauber model do not give any improvement, as several corrections tend to cancel each other [52]. One may ask how big the influence of the uncertainties in the experimentally measured employed parameters is. For my calculations, I need the total cross section, the diffraction slope b_o and the ratio of the real to imaginary part of the elastic forward scattering amplitude. Those values are needed for proton-neutron scattering and, for the calculations involving ^4He, also for the proton-proton scattering.

3.3.1 Cross Section

The total spin-independent cross sections are well known and do not pose any problem. However, the spin-dependent cross sections $\Delta\sigma_L$ and $\Delta\sigma_T$ have been determined only with large error bars [49, 71]. Although I discuss electron scattering from an unpolarized deuteron target here, the proton-neutron cross section entering in the Glauber FSI operator is not spin-independent, as the proton and neutron are in the triplet state: in the hard vertex I consider scalar photons, they do not affect the spin state, and in the deuteron there exists only the triplet state. The most general form of the total cross section for reactions with polarized beams and polarized targets is [72]

$$\sigma_{tot} = \sigma_o + \sigma_1 P_b \cdot P_t + \sigma_2 (P_b \cdot \hat{k})(P_t \cdot \hat{k}) \tag{3.13}$$

where σ_o is the total cross section for the reaction with unpolarized particles in the channel under consideration, $\hat{k}$ is the unit vector along the direction of the incident beam. The scalar products entering in Eq. (3.13) are [72]

$$\begin{aligned} P_b \cdot P_t &= \sum_m p_{t,m} - 3p_s \\ (P_b \cdot \hat{k})(P_t \cdot \hat{k}) &= \sum_m (-1)^{m+1} p_{t,m} - p_s \end{aligned} \tag{3.14}$$

where p_s and $p_{t,m}$ are the probabilities of finding the initial system in the singlet state or triplet state with the projection m on the axis k, respectively.

In the case considered here, the proton, which flies in the direction of the z-axis with approximately the momentum $\vec{q}$ of the photon acts as beam, and the neutron acts as target. As the deuteron consists of the triplet state only, $p_s = 0$, and one finds

$$\sigma_{tot} = \sigma_o + \sigma_1 + \sigma_2 (p_{t,1} + p_{t,-1} - p_{t,o}) \tag{3.15}$$

where the obvious relation $p_{t,1}+p_{t,o}+p_{t,-1} = 1$ was used. As all the triplet states have the same probability in the unpolarized deuteron: $p_{t,m} = \frac{1}{3}$, so that the expression for the total cross section further simplifies to

$$\sigma_{tot} = \sigma_o + \sigma_1 + \frac{1}{3}\sigma_2 \,. \tag{3.16}$$

The spin-dependent cross sections σ_1 and σ_2 are related to the measurable quantities $\Delta\sigma_L$ and $\Delta\sigma_T$ as

$$\begin{aligned} -\Delta\sigma_T &= 2\sigma_1 \\ -\Delta\sigma_L &= 2(\sigma_1 + \sigma_2) \,. \end{aligned} \tag{3.17}$$

$\Delta\sigma_L$ and $\Delta\sigma_T$ are determined from the cross section differences measured with parallel or anti-parallel orientations of the beam and target polarization vectors. So the total cross section for the considered case can be expressed as

$$\sigma_{tot} = \sigma_o - \frac{1}{6}\Delta\sigma_L - \frac{1}{3}\Delta\sigma_T \,. \tag{3.18}$$

In a measurement at SATURNE II, at an energy of the incoming beam of $T_{kin} = 1.000\, GeV$, $\sigma_1 = -\frac{1}{2}\Delta\sigma_T = -3.625\, mb \pm 0.44\, mb$ and $-\Delta\sigma_L = 8.894\, mb \pm 0.86\, mb$

(the errors given are total errors) were measured [71]. This leads to a total proton-neutron cross section

$$\sigma_{tot} = \sigma_o - (0.93 \pm 0.33)\, mb\,. \tag{3.19}$$

As the total spin independent cross section at the kinetic energy of $1\,GeV$ $\sigma_o = 40.4\,mb$ is much larger than the correction, it is justified to use σ_o instead of σ_{tot} in the above reported calculations. Even if the correction was known with higher precision, the effect of it on the calculations would be marginal. The correction will be more important for the case of the polarized deuteron target and is discussed in the next chapter. Both $\Delta\sigma_L$ and $\Delta\sigma_T$ show an interesting energy dependence around $T_{kin} \approx 1\,GeV$. Therefore, the correction term will also show an energy dependence. The possibility to use final state interaction effects to learn something about the spin-dependent nucleon-nucleon cross sections are discussed in connection with the polarized deuteron.

3.3.2 Diffraction Slope and ρ Parameter

For the diffraction slope b_o^2 and the ratio of the real to imaginary part of the forward elastic scattering amplitude, the data in the range of $T_{kin} \approx 1GeV$ is scarce and usually has large error bars. The compilation of values for b_o in [53] gives $b_o = 0.4 - 0.6 fm$ for proton-proton scattering. The more recent proton-proton data from Gatchina yield $0.5fm$ for $1\,GeV$ [55]. For proton-neutron scattering, the measured values vary around $0.5fm$ in the energy region of $1\,GeV$ [54]. The data have been collected using unpolarized beams and targets, so the spin dependent parts of the diffraction slope are unknown. For the calculations, I have assumed that $b_o = 0.5fm$ for proton-proton scattering, which represents an average of the available data, and the same value of $0.5\,fm$ for proton-neutron scattering. It is important to note that the precise value of b_o is not that important as long as we have $b_o \ll R_A$, which means that the final state interaction operator is short ranged compared to the nuclear radius. For the deuteron with $R_D \approx 2fm$ and ^4He with $R_{^4He} \approx 1.7fm$, this is certainly true.

To illustrate that the presented calculations are not very sensitive to the precise value of b_o, in Fig. 3.8 results obtained with $b_o = 0.4fm$ (dotted line) and $b_o = 0.6fm$ (dashed line) are shown. In parallel and antiparallel kinematics, the change in the results is negligible. This is to be expected, as b_o enters only in the transverse part of the FSI operator, and has therefore only small influence in (anti)parallel

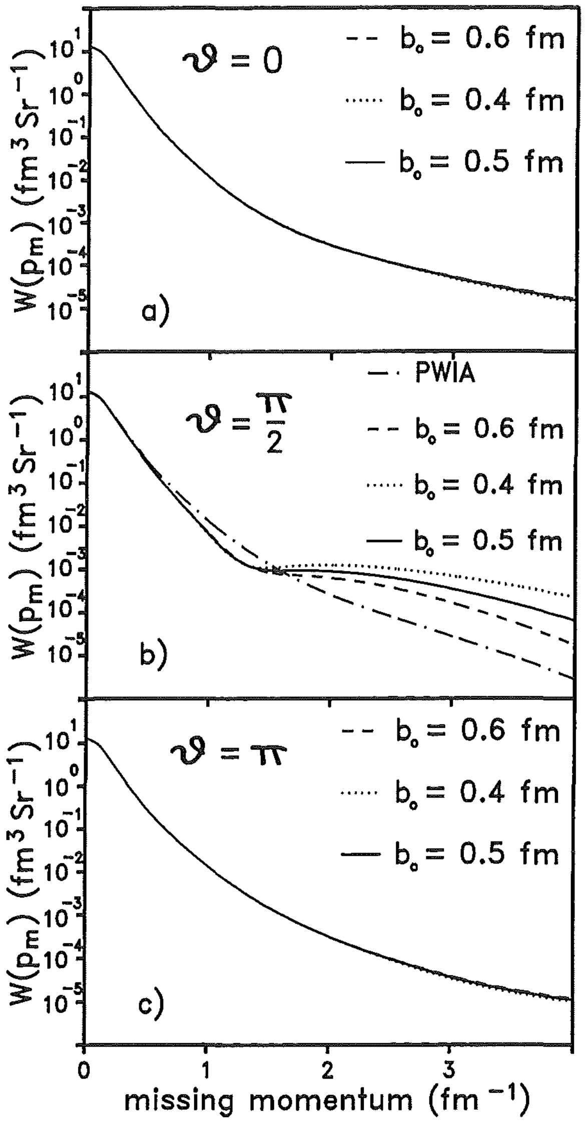

Figure 3.8: The missing momentum distribution $W(\vec{p}_m)$ for different values of the diffraction slope b_o for $theta = 0^o$ in a), for $\theta = 90^o$ in b), and for $\theta = 180^o$ in c). The solid line gives the result for $b_o = 0.5fm$, the dashed line for $b_o = 0.6fm$ and the dotted line for $b_o = 0.4fm$. For comparison, the PWIA distribution $N(p_m)$ (dash-dotted line) is plotted in b) .

kinematics. For perpendicular kinematics, the results remain qualitatively the same. For $b_o = 0.4fm$ (dotted line), the final state interaction is even shorter ranged and therefore the peak in perpendicular kinematics for $p_m \gtrsim 2fm^{-1}$ is more pronounced in this case. For $b_o = 0.6fm$, the range of the final state interaction is increased and therefore the tail at $p_m \gtrsim 2fm^{-1}$ is decreased. However, it is still larger by almost one order of magnitude than the PWIA distribution at $p_m = 3fm^{-1}$. Fig. 3.8 shows that the dependence of the results on the value of the diffraction slope b_o is small and that the observed changes in the calculations agree exactly with the expectations one has.

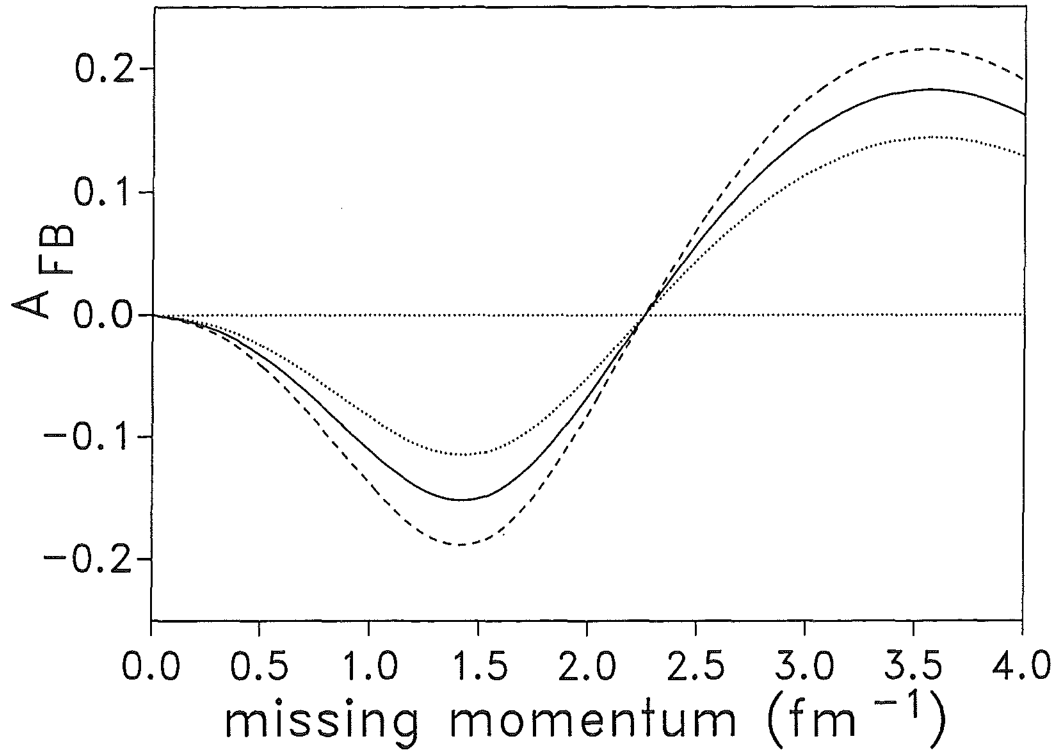

Figure 3.9: The forward-backward asymmetry calculated for $\rho = -0.3$ (dotted line), $\rho = -0.4$ (solid line), and $\rho = -0.5$ (dashed line).

Also for the ratio of the real to imaginary part of the elastic forward scattering amplitude ρ, in the region of $T_{kin} \approx 1\,GeV$, there are only few data for proton-proton scattering [73] and no data for direct proton-neutron scattering available. However, dispersion relation calculations [74, 56] reproduce the present data very well and it is reasonable to trust those calculations also for the proton-neutron case. Those calculations predict a $\rho = -0.4$. In order to demonstrate that the presented calculations are not very sensitive to the precise value of the parameter, the forward-backward asymmetry as defined in Eq. (3.11) is shown for $\rho = -0.3$ (dotted line), $\rho = -0.4$ (solid line), and $\rho = -0.5$ (dashed line) in Fig. 3.9. One can see clearly that the forward-backward asymmetry is proportional to ρ (for an extensive discussion of the forward-backward asymmetry see section 4.7). If one plots the momentum distributions calculated with different ρ values, one sees practically no difference between the curves. This shows again that the forward-backward asymmetry is a very suitable observable for a detailed study of the effects in (anti)parallel kinematics, in contrast to the momentum distribution.

The arguments and results of this section show that the influence of uncertainties in the experimental determination of the parameters which enter the Glauber theory calculation are negligible and that all qualitative conclusions about the nature and dominance of final state interaction effects are not altered by changes in those parameters.

Summarizing, the main result of the investigation of the $D(e, e'p)n$ reaction in the few-GeV energy range is that FSI effects completely dominate the observed missing momentum distribution $W(\vec{p}_m)$ at high p_m (over $\sim 1.5 fm^{-1}$). They produce a marked angular anisotropy in $W(\vec{p}_m)$, consisting in a dip at $\theta \sim 90^o$ (in perpendicular kinematics) for $p_m \sim (1-1.5)\, fm^{-1}$, and a prominent peak at the same angle for larger p_m. This anisotropy is mostly due to the FSI distortions of the S-wave contribution. The anisotropy effects in the D-wave contribution are also sizable, but much smaller than in the S-wave contribution. The D-wave contribution remains an important component for $p_m \gtrsim 1.5\, fm^{-1}$ in parallel kinematics. The effect of the final state interaction is different for perpendicular and (anti)parallel kinematics and for different values of the missing momentum. Inclusion of the final state interaction in the calculation of the observed missing momentum distribution can decrease or enhance it. Therefore it is obvious that the final state interaction effects cannot be accounted for by a simple overall factor multiplying the PWIA distribution.

From the obtained results it is clear that it will be difficult or impossible to obtain direct experimental information on the D-wave of the deuteron ground state in the $D(e, e'p)n$ reaction at the considered energy range. One may assume that the unpolarized deuteron is not the best suited target nucleus for this task, as the S-wave and D-wave do not interfere and as the available observables are not especially sensitive to the D-wave content of the deuteron. This is not so for polarized deuteron targets, which will be investigated in the next chapter.

Chapter 4

Electron Scattering on Tensor-Polarized Deuterons

Despite of the fact that the deuteron is a very dilute target, it was shown in the previous chapter that FSI effects dominate the missing momentum distribution for $p_m \gtrsim 1.5 fm^{-1}$ in electron scattering on unpolarized deuterons. There is a basic necessity to disentangle the short-distance and large relative momentum wave function of the deuteron and to distinguish between different models of the nucleon-nucleon interaction, and to this end, one can think of exploiting the tensor polarization of the deuteron. In contrast to the scattering from unpolarized deuterons, the S-wave and D-wave contributions can interfere in electron scattering from polarized deuterons. Moreover, besides the momentum distributions for different polarizations, one has a new observable, the tensor analyzing power, which is expected to be especially sensitive to the D-wave. Therefore, experiments on polarized deuterons could reveal much more information on the short range behaviour of the nucleon-nucleon interaction than the scattering from unpolarized deuterons which was discussed above. Indeed, due to the mixing of the S- and D-wave components by the tensor nuclear forces, the probability of FSI between the struck proton and the spectator neutron depends on the alignment (tensor polarization) of the deuteron.

Similar sensitivity to tensor polarization of the double scattering amplitude in elastic p - ${}^2\vec{H}$ scattering was discussed earlier [75, 76]. The ${}^2H(e,e'p)$ experiments with both polarized and unpolarized deuterons constitute an important part of the program at CEBAF [77, 78, 79]. The tensor analyzing power can also be measured in the ${}^2\vec{H}(e,e'p)$ reaction on the polarized deuteron jet target in the HERMES experiment at HERA [80].

The important new observable if only the target deuterons are polarized is the tensor analyzing power

$$A \equiv \frac{\sigma_+ + \sigma_- - 2\sigma_0}{\sigma_+ + \sigma_- + \sigma_0} = 2\frac{\sigma_+ - \sigma_0}{2\sigma_+ + \sigma_0}, \tag{4.1}$$

where σ_μ is the cross section for the polarization state of the deuteron $\mu = \pm 1, 0$ and we use the property $\sigma_+ = \sigma_-$. By definition, $-2 \leq A \leq 1$, the limits being saturated when $\sigma_+ = 0$ and $\sigma_o = 0$, respectively. Already in PWIA the tensor analyzing power A is nonzero, as the D-wave admixture in the deuteron produces tensor polarization dependent deviations from the spherical shape of the deuteron wave function. The interest in A stems from the potential sensitivity to the not so well known D-wave component of the deuteron and from the possibility of discrimination among different models for the deuteron ground state. For the same reason of the deviation from a spherically symmetric shape, the probability of FSI also depends on the tensor polarization: at large $\vec{q}$ the struck proton flies in the direction of $\vec{q}$, the probability of interaction with the spectator neutron is higher if the deuteron is aligned along $\vec{q}$ and the alignment depends on the tensor polarization. Consequently, the interpretation of the experimental data on the tensor analyzing power requires a quantitative understanding of FSI effects. The results of this chapter can be found in [16].

4.1 Tensor Analyzing Power in Plane Wave Impulse Approximation

As for the unpolarized deuteron, I would like to concentrate on the FSI effects and to focus on the simpler case of the longitudinal response. For this case, the photon can be treated as a scalar operator which does not change the spin state of the proton and the neutron (for the full hadronic tensor in deuteron scattering, see [81, 82]). The reduced nuclear amplitude for the exclusive process $\vec{D}(e, e'p)n$ is given by

$$\mathcal{M}_{\nu\mu} = \int d^3\vec{r} \exp(-i\vec{p}_m\vec{r})\chi^*_\nu S_\nu(\vec{r})\Psi_\mu(\vec{r}), \tag{4.2}$$

where $\vec{r} \equiv \vec{r}_n - \vec{r}_p$, $\Psi_\mu(\vec{r})$ is the wave function for the deuteron spin state μ and χ_ν stands for the spin wave function of the final pn state. $S_\nu(\vec{r})$ is the S-matrix of FSI between the struck proton and the spectator neutron, which describes the distortion of the outgoing waves. The subscript ν is a reminder that the np interaction in the final state may depend on the spin state. The observed momentum distribution corresponding to a given deuteron polarization μ is the sum

$$W_\mu(\vec{p}_m) = \frac{1}{(2\pi)^3} \sum_\nu |\mathcal{M}_{\mu\nu}|^2 . \tag{4.3}$$

It is convenient to introduce the S- and D-wave amplitudes

$$s(\vec{p}_m) \equiv \int d^3\vec{r}\, \frac{u(r)}{r} Y_{00}(\hat{r})\, S(\vec{r})\, \exp(i\vec{p}_m\vec{r}) \tag{4.4}$$

$$d_\tau(\vec{p}_m) \equiv \int d^3\vec{r}\, \frac{w(r)}{r} Y_{2\tau}(\hat{r})\, S(\vec{r})\, \exp(i\vec{p}_m\vec{r}), \tag{4.5}$$

where $\tau = 0, \pm 1, \pm 2$ and the possible weak dependence of the FSI factor $S(\vec{r})$ on the relevant spin state $|\sigma\rangle$ is suppressed, see below. In terms of these amplitudes the momentum distributions can be written as

$$W_+(\vec{p}_m) = \frac{1}{(2\pi)^3}\left(|s(\vec{p}_m) + \sqrt{\frac{1}{10}} d_o(\vec{p}_m)|^2 + \frac{3}{10}|d_1(\vec{p}_m)|^2 + \frac{3}{5}|d_2(\vec{p}_m)|^2 \right) \tag{4.6}$$

$$W_o(\vec{p}_m) = \frac{1}{(2\pi)^3}\left(|s(\vec{p}_m) - \sqrt{\frac{2}{5}} d_o(\vec{p}_m)|^2 + \frac{3}{10}|d_{-1}(\vec{p}_m)|^2 + \frac{3}{10}|d_1(\vec{p}_m)|^2 \right) \tag{4.7}$$

At first some simple results for PWIA are cited, where $S(\vec{r}) = 1$. Denoting

$$s(p_m) \equiv \int drru(r)j_o(p_m r), \quad d(p_m) \equiv \int drrw(r)j_2(p_m r), \tag{4.8}$$

one finds in PWIA

$$s^{PWIA}(\vec{p}_m) = \sqrt{4\pi}\, s(p_m) \tag{4.9}$$

$$d_\tau^{PWIA}(\vec{p}_m) = -4\pi Y_{2\tau}(\hat{p}_m) d(p_m) . \tag{4.10}$$

Denoting $W_\mu^{PWIA}(\vec{p}_m) = N_\mu(\vec{p}_m)$, one has

$$N_\pm(p_m, \theta) = N(1 + \frac{1}{2}A) \tag{4.11}$$

$$N_o(p_m, \theta) = N(1 - A) \tag{4.12}$$

where

$$N = \frac{1}{3}(N_+ + N_- + N_o) = \frac{1}{2\pi^2}\left(s^2(p_m) + d^2(p_m)\right) \tag{4.13}$$

is the missing momentum distribution for the unpolarized deuteron and the tensor analyzing power equals

$$A^{PWIA}(p_m, \theta) = \frac{1}{2}\frac{\sqrt{8}s(p_m)d(p_m) + d^2(p_m)}{d^2(p_m) + s^2(p_m)}\left(1 - 3cos^2(\theta)\right). \tag{4.14}$$

Notice the proportionality of $A^{PWIA}(\vec{p}_m)$ to $(1 - 3\cos^2(\theta))$, which determines the angular behaviour of the tensor analyzing power in PWIA

$$A^{PWIA}(p_m, \cos(\theta) = \pm\frac{1}{\sqrt{3}}) = 0 \tag{4.15}$$

and

$$A^{PWIA}(p_m, \theta = 0^o, 180^o) = -2A^{PWIA}(p_m, \theta = 90^o) \,. \tag{4.16}$$

Also, notice the property

$$N_0(p_m, \theta = 90^o) = N_\pm(p_m, \theta = 0^o, 180^o) = \frac{1}{2\pi^2}\left(s(p_m) - \frac{1}{\sqrt{2}}d(p_m)\right)^2 , \tag{4.17}$$

which holds because $Y_{2\pm1}(\hat{p}_m) = 0$ and therefore $d_{\pm1}(\vec{p}_m) = 0$ for $\theta = 0^o, 90^o, 180^o$, and $Y_{2\pm2}(\hat{p}_m) = 0$ and therefore $d_{\pm2}(\vec{p}_m) = 0$ for $\theta = 0^o, 180^o$.

4.2 Nodes of S- and D-Wave Amplitudes, S-D Wave Interference and Diffractive Dip-Bump Structure in PWIA

Here I discuss how the properties of the D-wave lead to certain features like zeroes and maxima of the momentum distributions and the tensor analyzing power in PWIA, and how the predictions for those zeroes and maxima differ for the Bonn model and the Paris model.

The salient features of the PWIA distributions $N_\mu(\vec{p}_m)$ and the tensor analyzing power $A^{PWIA}(\vec{p}_m)$ can easily be understood in terms of the p_m-dependence of $s(p_m)$ and $d(p_m)$. For the sake of definiteness, consider perpendicular kinematics, i.e. $\theta = 90^o$. The separate S- and D-wave function contributions (dotted line and dash-dotted line, respectively) to $N_o(p_m, \theta = 90^o)$ (solid line) and $N_+(p_m, \theta = 90^o)$ (solid line) are shown in Figs. 4.1c,d, respectively, for the Bonn potential [25]. Notice a stronger D-wave contribution to $N_+(p_m, \theta = 90^o)$. The total distributions $N_\mu(p_m)$ include also the S-D interference terms which are not shown separately. The S-wave amplitude $s(p_m)$ has a zero at $p_m = p_m^{(1)} = 2.22 fm^{-1}$ for the Bonn potential. The D-wave amplitudes $d_\tau(\vec{p}_m)$ have a kinematical zero at $p_m = 0$ and are node-free in the considered region of p_m. The S- and D-wave amplitudes become comparable at $p_m \gtrsim 1.5 fm^{-1}$, and the D-wave contribution takes over at larger p_m. For the Bonn potential $N_o(p_m, \theta = 90^o)$ has a zero at $p_m = p_m^{(2)} = 1.58 fm^{-1}$ for the destructive interference and exact cancelation of the S-wave and the D-wave contributions, when $d(p_m) = \sqrt{2}s(p_m)$, see Eq. (4.17). At $p_m > p_m^{(1)}$, the S-D interference in $N_o(p_m, \theta = 90^o)$ becomes constructive: the sum of the S-wave and D-wave contributions (dashed line) is considerably smaller than the total distribution N_o. The p_m-dependence of $N_o(p_m, \theta = 90^o)$ and $N_+(p_m, \theta = 90^o)$ is strikingly different. As shown in Fig. 4.1d, $N_+(p_m, \theta = 90^o)$ exhibits a smooth, structure-less decrease with p_m, and interference effects are small, with a change from constructive to destructive interference at $p_m > p_m^{(1)}$. The effect of the dip in the S-wave contribution is completely masked by an overwhelming D-wave contribution.

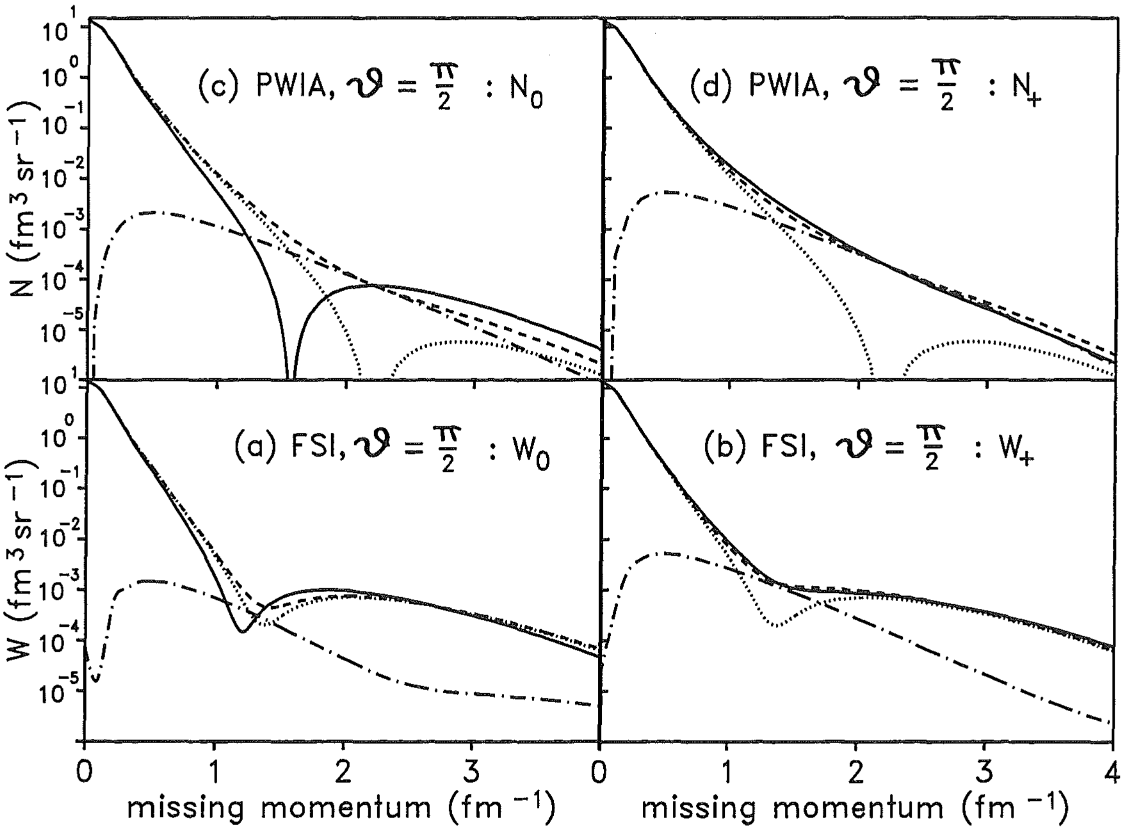

Figure 4.1: The full momentum distributions (solid line) W_o (a), W_+ (b) including FSI and N_o (c), N_+ (d) vs. p_m at $\theta = 90^o$ and their decomposition in the S-wave (dotted line) and D-wave (dash-dotted line) contribution. The dashed line shows the sum of S- and D-wave contribution.

The properties of $s(p_m)$ and $d(p_m)$ have simple manifestations in the tensor analyzing power. At $p_m \to 0$ one has $A^{PWIA}(p_m, \theta = 90^o) \to 0$ due to the vanishing of the D-wave function $d(p_m)$. With increasing p_m, $A^{PWIA}(p_m, \theta = 90^o)$

(dotted line in Fig. 4.2) stays positive, and saturates at $p_m = p_m^{(2)}$ the upper bound $A^{PWIA}(p_m, \theta = 90^o) = 1$, when $N_o(p_m, \theta = 90^o)$ vanishes, as predicted by Eq. (4.12). With the further increase of p_m, the tensor analyzing power decreases and takes the value $A^{PWIA}(p_m, \theta = 90^o) = \frac{1}{2}$ when the S-wave function $s(p_m)$ has a node at $p_m = p_m^{(1)} = 2.22 fm^{-1}$ for the Bonn potential. Beyond the node, the S-wave function rises in magnitude, leading to a change of sign of $A^{PWIA}(p_m, \theta = 90^o)$ at $p_m = p_m^{(3)} = 2.73 fm^{-1}$ for the Bonn potential, when $s(p_m) = -\frac{1}{\sqrt{8}} d(p_m)$.

The position $p_m^{(2)}$ of the zero in $N_0(p_m, \theta = 90^o)$ and $N_\pm(p_m, \theta = 0^o, 180^o)$, and the position $p_m^{(3)}$ of the zero of $A^{PWIA}(p_m, \theta = 90^o)$, are a matter of delicate cancelations between the S- and D-wave functions. As such, they are sensitive to the D-wave function, which remains a not so well known quantity in the theory of the deuteron. In Fig. 4.2a the predictions for $A^{PWIA}(p_m, \theta = 90^o)$ from the Bonn and Paris [26] wave functions (dotted and dash-dotted curve, respectively) are compared. The qualitative behaviour of the results is the same, but for the Paris potential, $N_0(p_m, \theta = 90^o)$ has a zero at a value of $p_m^{(2)} = 1.50 fm^{-1}$, which is $0.08 fm^{-1}$ smaller than for the Bonn wave function. The sensitivity to the model of the wave function increases with p_m: for the Paris wave function, the tensor analyzing power changes sign at a value of $p_m^{(3)} = 2.52 fm^{-1}$, by about $0.2 fm^{-1}$ smaller than for the Bonn wave function.

The angular dependence of $N_\mu(p_m, \theta)$ in PWIA for different missing momenta is shown in Fig. 4.3 and the angular distribution of $A^{PWIA}(p_m, \theta)$ is shown by the dotted curve in Fig. 4.4. As $N = \frac{1}{3}(N_+ + N_- + N_o) = \frac{1}{3}(2N_+ + N_o)$ is the PWIA distribution for scattering on unpolarized deuterons which does not change with the angle θ, a minimum in N_+ (dotted curve) in the angular distribution corresponds to a maximum in N_o (dashed curve) and vice versa, and $N_+ = N_o$ at $\theta = \arccos\left(\pm\frac{1}{\sqrt{3}}\right) = 90^o \pm 35.3^o$, as the tensor analyzing power vanishes at this angle (see Eqs. (4.14),(4.11),(4.12)). By virtue of the definition (4.1) the sign of the difference between $N_\pm(p_m, \theta)$ and $N_o(p_m, \theta)$ depends on the tensor analyzing power A. For instance, $A^{PWIA}(p_m, \theta = 90^o)$ changes sign at $p_m^{(3)} = 2.73 fm^{-1}$ (see Figs. 4.2,4.4) and for $p_m > p_m^{(3)}$ we have $N_+(p_m, \theta = 90^o) < N_o(p_m, \theta = 90^o)$, whereas for $p_m < p_m^{(3)}$ we have $N_+(p_m, \theta = 90^o) > N_o(p_m, \theta = 90^o)$, cf. Figs. 4.3a-e and Fig. 4.3f. In PWIA, the distributions $N_\mu(p_m, \theta)$ are even functions of $\cos\theta$, and there is no forward-backward asymmetry: $N_\mu(p_m, \theta = 0^o) = N_\mu(p_m, \theta = 180^o)$.

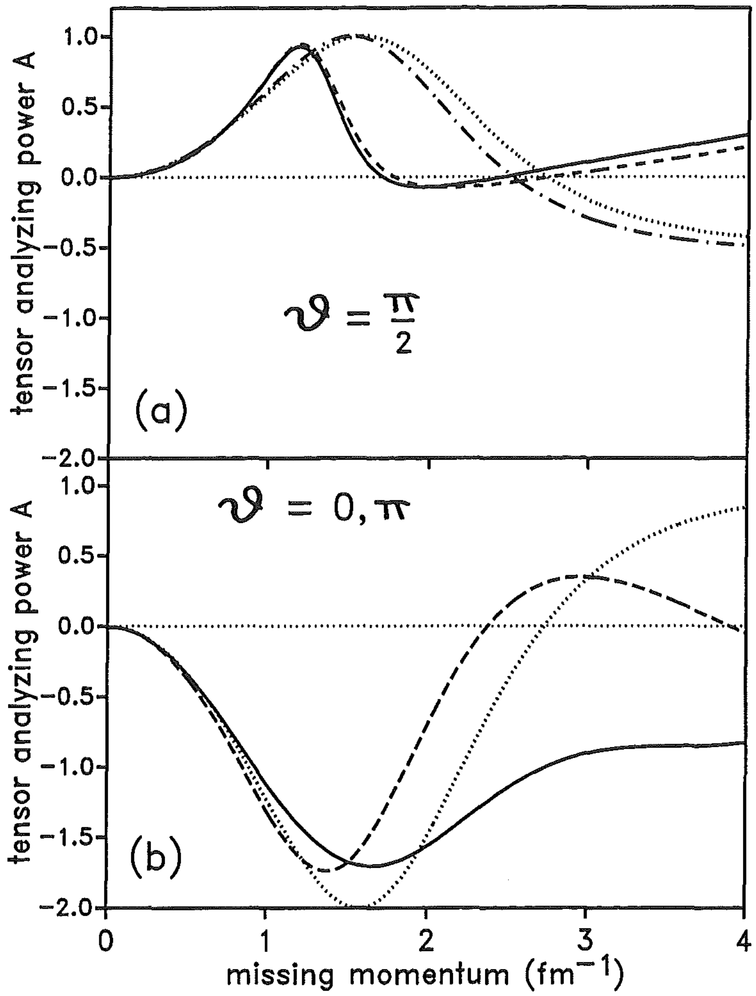

Figure 4.2: The tensor analyzing power vs. the missing momentum p_m. Panel (a) shows $A^{PWIA}(p_m, \theta = 90^o)$ calculated using the Bonn wave function (dotted line) and calculated using the Paris wave function (dash-dotted line) and also $A(p_m, \theta = 90^o)$ calculated with the Bonn wave function (solid line) and with the Paris wave function (dashed line). Panel (b) shows $A^{PWIA}(p_m, \theta = 0^o) = A^{PWIA}(p_m, \theta = 180^o)$ (dotted line) and A calculated including FSI for $\theta = 0^o$ (long-dashed line) and $\theta = 180^o$ (solid line).

4.3 FSI Effects and Nodal Structure of S- and D-Wave Amplitudes

FSI effects substantially modify the above pattern. The FSI-operator $S(\vec{r})$ and the profile function $\Gamma(\vec{b})$ have the same form as for unpolarized deuterons, but the

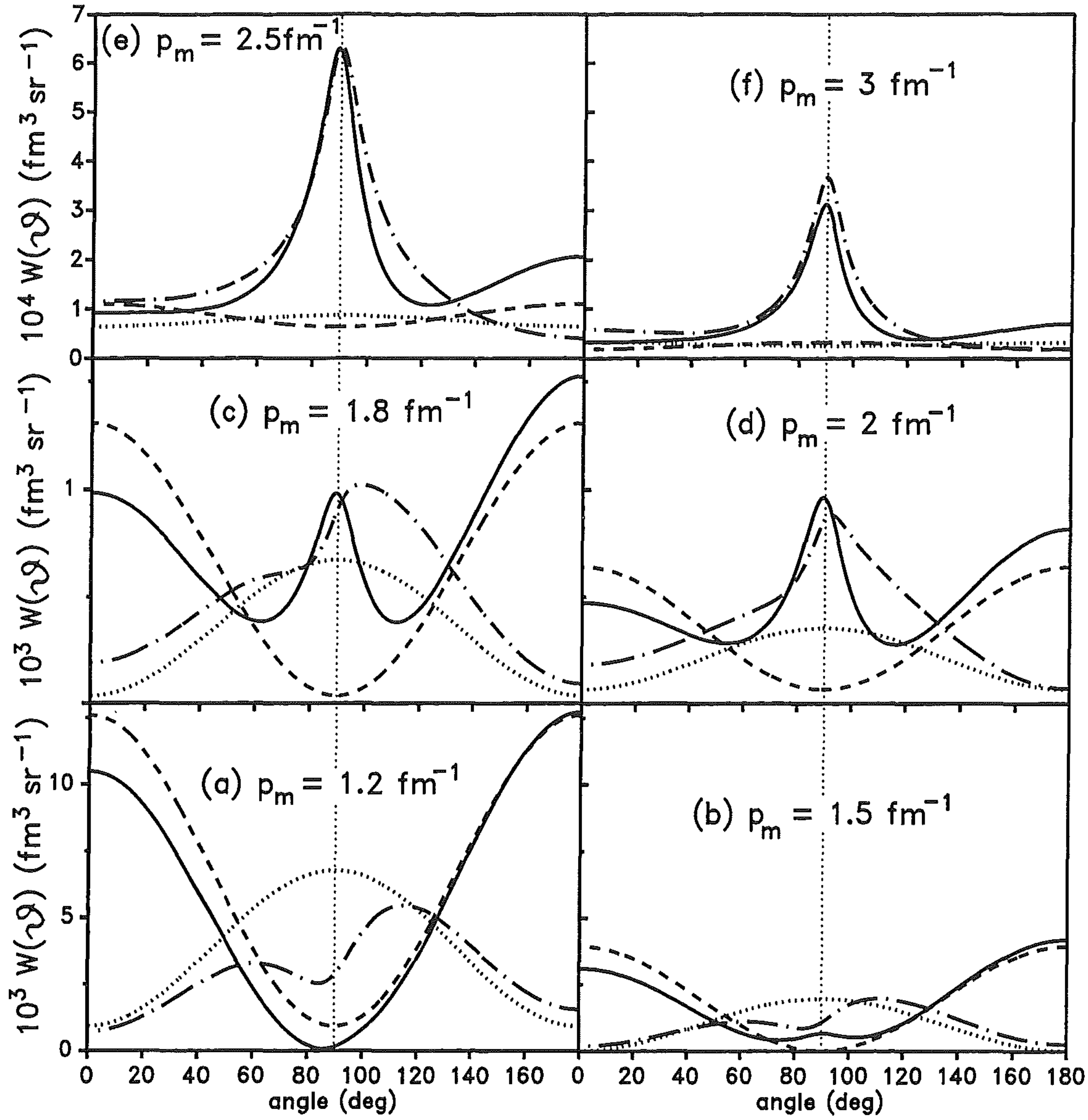

Figure 4.3: The angular dependence of the missing momentum distributions N_o (dashed line), N_+ (dotted line), W_o (solid line) and W_+ (dash-dotted line) for different values of the missing momentum p_m.

dependence on the spin state has to be taken into account:

$$S_\nu(\vec{r}) = 1 - \theta(z)\Gamma_\nu(\vec{b}), \tag{4.18}$$

and

$$\Gamma_\nu(\vec{b}) \equiv \frac{\sigma_{tot}^{(\nu)}(1 - i\rho_\nu)}{4\pi b_o^2} \exp\left[-\frac{\vec{b}^2}{2b_o^2}\right] = (1 - i\rho_\nu)G_\nu(\vec{b}). \tag{4.19}$$

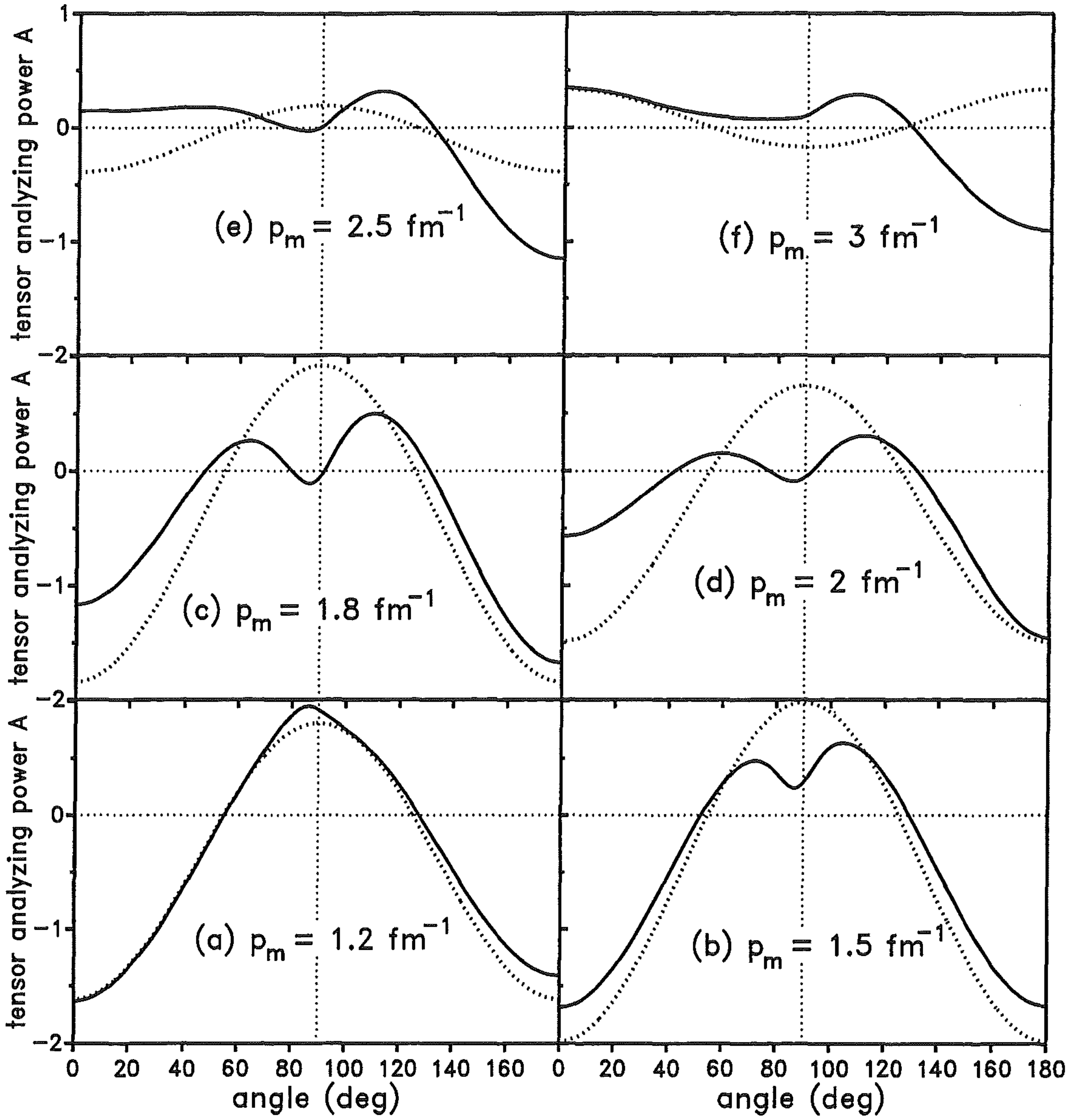

Figure 4.4: The angular dependence of the tensor analyzing power in PWIA (dotted line) and including FSI (solid line) for different values of the missing momentum.

As the struck protons have high energy and momentum and as the simple case of the longitudinal response considered here, the spin state of the proton and neutron does not change and FSI between struck proton and spectator neutron proceeds in the spin triplet state. What enters the Glauber FSI factor (4.19) is the np total cross section $\sigma_{tot}^{(\nu)}$ for the triplet state with polarization ν. One can express $\sigma_{tot}^{(\nu)}$ in terms of the conventional longitudinal, $\Delta\sigma_L$, and transverse, $\Delta\sigma_T$, cross section differences [72, 49] (compare section 3.3). For transverse polarization $|\nu\rangle = \pm 1$, the probabilities for the triplet states are $p_{t,+} + p_{t,-} = 1$ and $p_{t,o} = 0$ and one finds from Eq. (3.15)

$$\sigma_{tot}^{(\pm 1)} = \sigma_o + \sigma_1 + \sigma_2 = \sigma_o - \frac{1}{2}\Delta\sigma_L\,, \tag{4.20}$$

and for longitudinal polarization $|\nu\rangle = 0$, one has $p_{t,o} = 1$ and $p_{t,+} + p_{t,-} = 0$ and finds the cross section

$$\sigma_{tot}^{(o)} = \sigma_o + \sigma_1 - \sigma_2 = \sigma_o - \Delta\sigma_T + \frac{1}{2}\Delta\sigma_L\,. \tag{4.21}$$

The experimental data on $\Delta\sigma_L$ and $\Delta\sigma_T$, reviewed in [49], show that $\Delta\sigma_L$ and $\Delta\sigma_T$ are $\lesssim (10-20)\%$ of the unpolarized cross section σ_o. They exhibit an interesting energy dependence in the region $0.5\,GeV \lesssim T_{kin} \lesssim 1\,GeV$ and tend to decrease at higher T_{kin}. For $T_{kin} = 1.0\,GeV$, the SATURNE II data [71] yield $\sigma_1 = -\frac{1}{2}\Delta\sigma_T = -3.625\,mb \pm 0.44\,mb$ and $-\Delta\sigma_L = 8.894\,mb \pm 0.86\,mb$, leading to

$$\sigma_{tot}^{(\pm 1)} = \sigma_o + (4.447 \pm 0.43)\,mb \tag{4.22}$$

and

$$\sigma_{tot}^{(o)} = \sigma_o - (11.697 \pm 0.979)\,mb\,. \tag{4.23}$$

This shows that the correction for the spin-dependence is small for transversely polarized deuterons and more significant for longitudinally polarized deuterons. In principle, the experimental isolation of FSI effects and investigation of their T_{kin} dependence can shed some light on the energy dependence of $\sigma_{tot}^{(\nu)}$. As already mentioned in section 3.3.2, direct experimental measurements of ρ_ν and of the diffractive slope b_o^2 for pure spin states ν are unfortunately not yet available. The interplay of FSI and tensor polarization effects leads to a very complex pattern of the (p_m, θ) dependence of momentum distributions. In order to emphasize the salient features of FSI effects, here I omit small corrections due to $\Delta\sigma_L, \Delta\sigma_T$ and, for the sake of definiteness, consider $\sigma_{tot} = 40.4mb$, $\rho = -0.4$ and $b_o = 0.5fm$, appropriate for unpolarized np scattering at $T_{kin} \approx 1GeV$ [40, 49, 53, 54]. The small effect of the correction to σ_{tot}^o is discussed in section 4.6.

As for the unpolarized deuteron target, the fact that the FSI operator $\theta(z)\Gamma(\vec{b})$ is a "short-ranged" function of $\vec{b}$ and a "long-ranged" function of z leads to the anisotropy of $S(\vec{r})S^\dagger(\vec{r}\,')$ and to the angular anisotropy of $W(\vec{p}_m)$. The forward-backward asymmetry $W(p_\perp, -p_z) \neq W(p_\perp, p_z)$, which has its origin in the non-vanishing real part of the p-n scattering amplitude $\rho \neq 0$, is also present. This angular anisotropy of FSI effects leads to quite a complex interplay of FSI and S-D interference, breaking of the PWIA symmetry properties (4.15) - (4.17), and strong departure from the PWIA law $A \propto (1 - 3\cos^2(\theta))$. A further complication comes from the finite ρ, which, apart from the forward-backward asymmetry leads to complex-valued S- and D-wave amplitudes and to the filling of the dips in the distributions $N_\mu(\vec{p}_m)$.

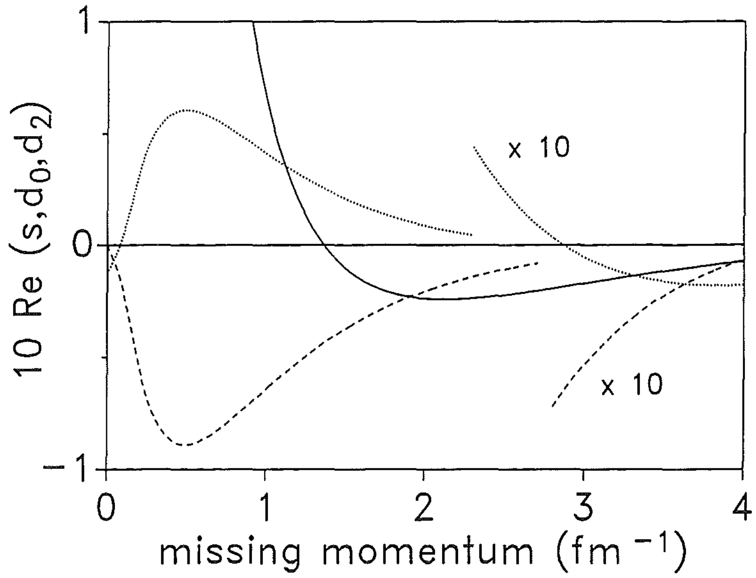

Figure 4.5: The real parts of the matrix elements $s(\vec{p}_m)$ (solid line), $d_o(\vec{p}_m)$ (dotted line) and $d_2(\vec{p}_m)$ (dashed line) for $\theta = 90^o$ including FSI, as defined in Eqs. (4.4), (4.5). Notice the change of the scale of $d_o(\vec{p}_m)$ at $p_m = 2.3 fm^{-1}$, and of $d_2(\vec{p}_m)$ at $p_m = 2.7 fm^{-1}$.

The gross features of FSI effects can readily be understood, though, in terms of FSI distortions of the S- and D-wave amplitudes (4.4), (4.5); those features are already present for the unpolarized case (compare with the previous chapter): i) Angular anisotropy of the FSI factor (4.18) leads to an angular dependence of the S- and D-wave amplitudes (4.4),(4.5) which is different from the PWIA expressions (4.9),(4.10). ii) At small $p_m \lesssim 0.5 fm^{-1}$, FSI reduces $s(\vec{p}_m)$ by $\sim$ 3.5%. In this region of small p_m, the FSI reduction is to a good approximation θ- independent. It describes the attenuation of the flux of struck protons due to inelastic np interactions and the flow of events from small to large $p_\perp$ due to elastic np rescattering. iii) Destructive interference between PWIA and FSI components of $s(\vec{p}_m)$ produces a node of the real part of $s(\vec{p}_m)$, shown by the solid curve in Fig. 4.5, in perpendicular kinematics, $\theta = 90^o$, at $p_\perp = p_m^{(4)} = 1.37 fm^{-1}$ (for the Bonn wave function). The presence of this node, shown in Fig. 4.5, is solely a consequence of the PWIA-FSI interference, it is not related to the presence of the node in the PWIA amplitude (4.9) at much larger $p_m = p_m^{(1)} = 2.22 fm^{-1}$. The position of the node of $Res(\vec{p}_m)$ in $p_\perp$ only weakly depends on the longitudinal component p_z of the missing momentum. iv) At larger $p_\perp$, the FSI contribution to $s(\vec{p}_m)$ becomes much larger than the PWIA amplitude, and leads to a sharp peak at $\theta = 90^o$. This peak has its origin in elastic rescattering of the struck proton on the spectator neutron, which contributes predominantly to $\theta = 90^o$ for the reason that in high-energy elastic rescattering the momentum transfer is predominantly a transverse one (see the discussion in section 2.3). Fig. 4.3 shows how this 90^o peak builds up with the increase of p_m.

Distortion of the D-wave amplitudes $d_\tau(\vec{p}_m)$ has a certain specifics due to the fact that the radius of pn FSI is much smaller than the radius of the deuteron. For crude estimates, consider the approximation of the zero-range pn interaction:

$$\Gamma(\vec{b}) \approx \frac{1}{2}\sigma_{tot}(pn)(1 - i\rho)\delta(\vec{b}) . \tag{4.24}$$

For the presence of $\delta(\vec{b})$ in (4.24), FSI contributions to $d_\tau(\vec{p}_m)$ will be dominated by $\cos\alpha = 1$ (α is the angle of $\vec{r}$ with the z-axis), where $Y_{2\pm2}(\alpha) = Y_{2\pm1}(\alpha) = 0$. This leads to an extra, and very strong kinematical suppression of the final state interaction contributions to $d_{\pm2}(\vec{p}_m)$ and $d_{\pm1}(\vec{p}_m)$. On the other hand, the FSI contribution to $d_o(\vec{p}_m)$ does not have any special suppression and, in close similarity to an S-wave amplitude, the real part of $d_o(\vec{p}_m)$, shown by the dotted curve in Fig. 4.5, develops a node at $p_\perp = p_m^{(5)} = 2.87 fm^{-1}$ (for the Bonn wave function). Compared to $d_o(\vec{p}_m)$, in $d_{\pm1}(\vec{p}_m)$ and $d_{\pm2}(\vec{p}_m)$ FSI effects are negligible in the region of practical interest where $p_m \lesssim (3-4) fm^{-1}$. For instance, $Re\, d_2(\vec{p}_m)$, shown by the dashed curve in Fig. 4.5 does not develop a node.

Still another striking effect of FSI is a nonvanishing $d_\tau(\vec{p}_m)$ at $\vec{p}_m = 0$, as shown in Fig. 4.5 for $\theta = 90^o$. Indeed, in the momentum space, the FSI contribution can be represented as a convolution of the PWIA amplitude with a certain smearing function. Because of this smearing, $d_\tau^{FSI}(\vec{p}_m = 0) \neq 0$. Because of the kinematical suppression of the PWIA amplitude at small p_m, even a weak FSI amplitude which has a sign opposite to that of the PWIA amplitude, leads to a zero of $Re\, d_\tau(\vec{p}_m)$ at small p_m. Fig. 4.5 shows how $Re\, d_o(p_m, \theta = 90^o)$ develops such a zero at $p_\perp = p_m^{(6)} = 0.09 fm^{-1}$ for $\theta = 90^o$. The nonvanishing D-wave contribution at $\vec{p}_m = 0$ when FSI is included is evident also in Figs. 4.1a,b. However, because of the strong inequality

$|d_\tau(\vec{p}_m)| \ll |s(\vec{p}_m)|$ in the vicinity of $p_m = 0$, it is very difficult to observe this fine structure of the D-wave amplitudes experimentally.

4.4 FSI Effects on the S-D Interference and on the Position of Diffractive Dips

Now the obtained results can be interpreted in view of the above described properties of FSI. At small $p_m \lesssim 0.5 fm^{-1}$, both $W_o(\vec{p}_m)$ and $W_+(\vec{p}_m)$ are dominated by the S-wave contribution and are reduced by $\simeq 7\%$ with respect to the PWIA distributions $N_o(p_m)$ and $N_+(p_m)$. The discussion of larger p_m is started again with the simpler case of $W_o(\vec{p}_m, \theta = 90^o)$ shown by the solid curve in Fig. 4.1a. The S-wave contribution, shown by the dotted line, has a dip at $p_m = p_m^{(4)} = 1.37 fm^{-1}$ for the node of $Re\, s(\vec{p}_m)$ (the same dip shows up in $W_+(\vec{p}_m)$ shown by the solid line in Fig. 4.1b). In the PWIA case, the dip of the S-wave contribution to $N_\mu(\vec{p}_m)$ was located at $p_m = p_m^{(1)} = 2.22 fm^{-1}$ and its effect on $N_\mu(\vec{p}_m)$ was barely observable for the overwhelming D-wave contribution. The dip in the S-wave component of $W_{o,+}(\vec{p}_m)$ is filled in by the contribution from the imaginary part of the S-wave amplitude. The D-wave component of $W_o(\vec{p}_m)$ (dash-dotted curve in Fig. 4.1a) shows an irregularity at $p_m = p_m^{(5)} = 2.87 fm^{-1}$ due to the node of $Re\, d_o(\vec{p}_m)$. The possible dip of the D-wave component of $W_o(\vec{p}_m)$ is filled in by a contribution from $Im\, d_o(\vec{p}_m)$ (and also by the much smaller FSI components of $d_2(\vec{p}_m), d_{\pm 1}(p_m)$). This irregularity is difficult to observe experimentally due to the predominant S-wave contribution to $W_o(p_m, \theta = 90^o)$.

Because of the shift of the zero of $Re\, s(\vec{p}_m)$ to $p_m = p_m^{(4)} = 1.37 fm^{-1}$ compared to $p_m^{(1)} = 2.22 fm^{-1}$ in the PWIA, the condition $Re\, s(p_m, \theta = 90^o) \simeq \sqrt{\frac{5}{2}} Re\, d(p_m, \theta = 90^o)$ and the resulting dip in $W_o(\vec{p}_m)$ will be met at $p_m = p_m^{(7)} = 1.21 fm^{-1}$, a strong shift from $p_m^{(2)} \simeq 1.58 fm^{-1}$ in the PWIA, cf. solid curves in Figs. 4.1a,c. The dip in $W_o(\vec{p}_m)$ is partly filled in by the contribution $\propto |Im\, s(\vec{p}_m)|^2$ (there is also a small effect of interference between $Im\, s(\vec{p}_m)$ and $Im\, d_o(\vec{p}_m)$ and a small contribution from nonvanishing FSI components of $d_{\pm 1}$ and $d_{\pm 2}$). FSI effects in $W_o(p_m, \theta = 90^o)$ are very strong and lead to a drastic difference between $W_o(p_m, \theta = 90^o)$ and the PWIA distribution $N_o(p_m, \theta = 90^o)$ starting already from a small missing momentum $p_m \gtrsim (0.8 - 0.9) fm^{-1}$. FSI effects in $W_+(p_m, \theta = 90^o)$ are even larger than in $W_o(p_m, \theta = 90^o)$, for $p_m > 2.5 fm^{-1}$ W_+ is by one order of magnitude larger than N_+. The dip in the S-wave contribution leads to a substantial structure in $W_+(p_m, \theta = 90^o)$ shown by the solid curve in Fig. 4.1b, as compared to a structureless and monotonously decreasing PWIA distribution $N_+(p_m, \theta = 90^o)$. The dip in W_+ is not as pronounced as the dip in W_o, as the interference is much weaker for W_+.

At a sufficiently large $p_\perp$, the contribution of elastic rescattering to $W_\mu(p_m, \theta = 90^o)$ admits to a certain extent a probabilistic interpretation. At $p_\perp \gtrsim 2.5 fm^{-1}$ the 90^o peak in $W_+(p_m, \theta = 90^o)$ is higher than in $W_o(p_m, \theta = 90^o)$, in agreement with the fact that the the proton and the neutron are aligned along the z-axis only for $\mu = \pm 1$, which leads to a higher probability of FSI (see the discussion in section 4.5).

The results for parallel kinematics, $p_\perp = 0$, $\theta = 0^o$ and $\theta = 180^o$, are shown in Fig. 4.6. At small $p_\perp$, FSI amplitudes are suppressed by a small factor $\propto \frac{\sigma_{tot}^{(pn)}}{4\pi R_D^2} \sim \left(\frac{b_o}{R_D}\right)^2$. For this reason of small FSI effects, $W_+(p_m, \theta = 180^o)$ (solid curve in Fig. 4.6a) has a shallow dip and $W_+(p_m, \theta = 0^o)$ (dashed curve in Fig. 4.6a) has a shoulder-like structure at p_m very close to the position of the dip in the PWIA distribution $N_+(p_m, \theta = 0^o, 180^o)$ (dotted curve) at $p_m = p_m^{(2)} = 1.58 fm^{-1}$. Substantial departure from PWIA starts at $p_m \gtrsim 1 fm^{-1}$ and is very strong at higher p_m.

In Fig. 4.6a, I present also $W_o(p_m, \theta = 90^o)$ (dash-dotted curve). A comparison with $W_+(p_m, \theta = 0^o)$ (dashed curve) and $W_+(p_m, \theta = 180^o)$ (solid curve) shows a dramatic breaking of the PWIA symmetry (4.17) by FSI effects. Strong breaking of still another PWIA symmetry, $W_\mu(p_m, \theta = 0^o) \neq W_\mu(p_m, \theta = 180^o)$, will be discussed in more detail below, in section 4.7.

In spite of the suppression factors $\sim \left(\frac{b_o}{R_D}\right)^2$, FSI effects in $W_+(p_m, \theta = 0^o, 180^o)$ shown in Fig. 4.6a are enhanced due to the destructive S-D interference, see Eqs. (4.6), (4.7). In $W_o(p_m, \theta = 0^o, 180^o)$, shown in Fig. 4.6b, the S-D interference is constructive and consequently, $W_o(p_m, \theta = 0^o)$ (dashed curve) and $W_o(p_m, \theta = 180^o)$ (solid curve) are least sensitive to FSI effects. Even so, FSI effects are noticeable already at relatively small $p_m \gtrsim 1 fm^{-1}$. Notice that at large $p_m \gtrsim (2.5 - 3) fm^{-1}$ the distributions $W_o(p_m, \theta = 0^o)$ and $W_o(p_m, \theta = 180^o)$ exhibit a strong excess over the PWIA distribution $N_o(p_m, \theta = 0^o)$ (dotted curve), and decrease very slowly compared to the PWIA distribution $N_o(p_m, \theta = 0^o)$. The origin of this excess lies in the θ-function which emerges in the idealized form of the Glauber FSI operator

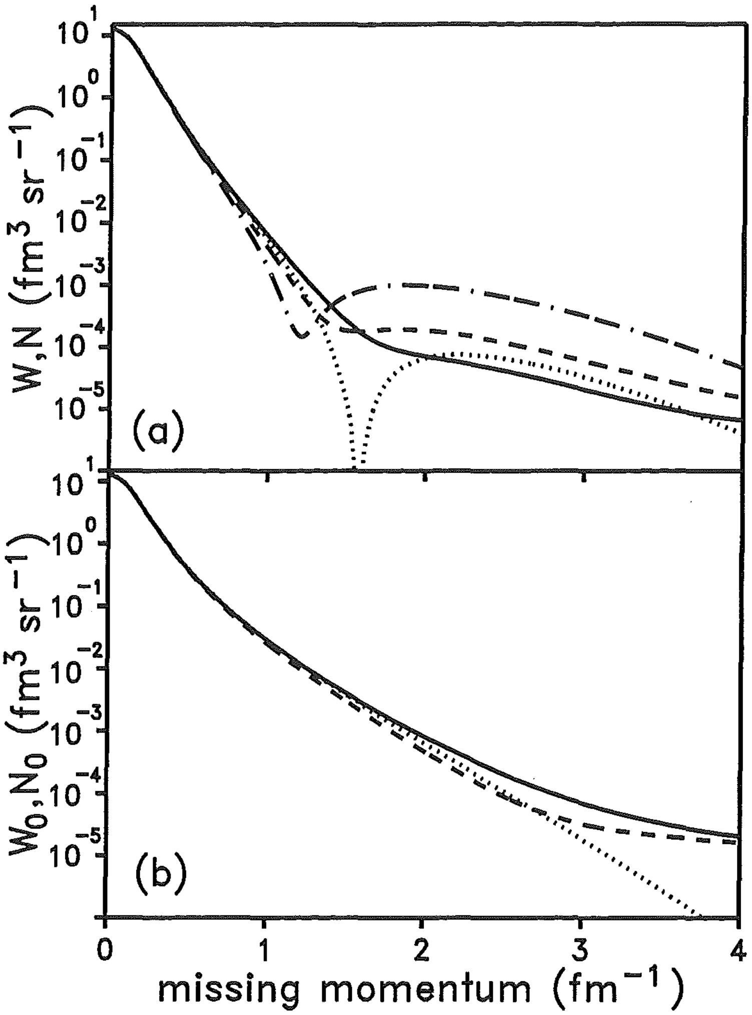

Figure 4.6: (a) The momentum distributions $W_+(p_m, \theta = 0^o)$ (dashed line), $W_+(p_m, \theta = 180^o)$ (solid line) and $W_o(p_m, \theta = 90^o)$ (dash-dotted line) including FSI and $N_+(p_m, \theta = 0^o) = N_+(p_m, \theta = 180^o)$ (dotted line). (b) The momentum distributions $W_o(p_m, \theta = 0^o)$ (dashed line), $W_o(p_m, \theta = 180^o)$ (solid line) and $N_o(p_m, \theta = 0^o) = N_o(p_m, \theta = 180^o)$ (dotted line).

(4.18). For the discussion of the sensitivity of this excess to modifications of the FSI operator for the finite size of the nucleus see the previous chapter.

A comment on the interpretation of the above results in terms of the nuclear transparency ratio

$$T_\mu = \frac{W_\mu(p_m, \theta)}{N_\mu(p_m, \theta)} \tag{4.25}$$

is in order. The results for $T_o(p_m, \theta = 90^o)$ and $T_+(p_m, \theta = 90^o)$ are shown in Fig. 4.7.

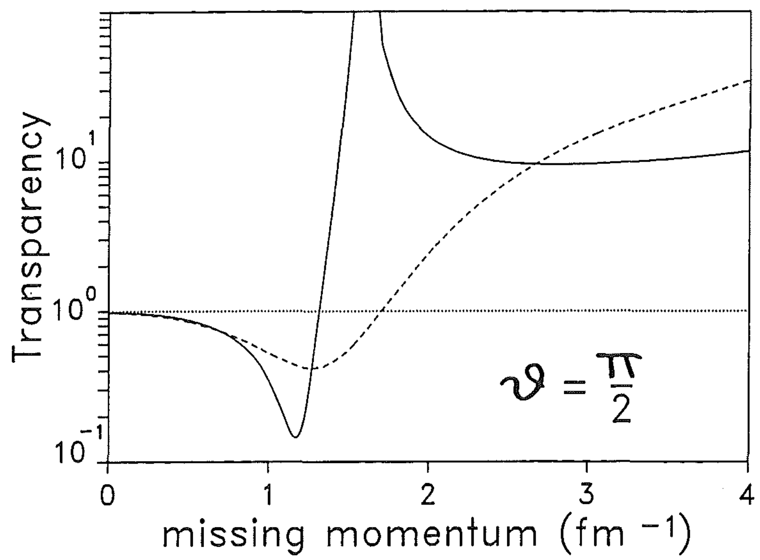

Figure 4.7: The nuclear transparency ratio $T_o(p_m, \theta = 90^o)$ (solid line) for longitudinally polarized deuterons and $T_+(p_m, \theta = 90^o)$ (dashed line) for transversely polarized deuterons in perpendicular kinematics.

Only at small $p_m \sim 0$, the result that $T_\mu(p_m, \theta) \simeq 0.93 < 1$ can be interpreted as a conventional nuclear attenuation. At higher p_m, the nuclear transparency ratio has a strongly polarization dependent dip-bump structure. The rich and complex p_m and θ dependence of the nuclear transparency $T_\mu(p_m, \theta)$ is evident from the results shown in Fig. 4.3. For instance, in transverse kinematics $T_o(p_m^{(7)}, \theta = 90^o) \ll 1$, which is followed by a rapid rise of the transparency ratio and an infinite peak $T_o(p_m^{(2)}, \theta = 90^o) = \infty$ at the dip of the PWIA distribution $N_o(p_m, \theta = 90^o)$. At still larger $p_\perp$, in the region dominated by elastic rescattering effects, there is very strong nuclear enhancement (antishadowing) $T_\mu(p_m, \theta) \gg 1$ (see also [15, 35]).

4.5 The Tensor Analyzing Power

The tensor analyzing power for $\theta = 90^o$ calculated with the Bonn wave function including final state interaction is shown by the solid line in Fig. 4.2. Before going into the details, the effects of the final state interaction can be discussed qualitatively: already at rather low missing momenta $p_m \gtrsim 0.9 fm^{-1}$, there is a distinct deviation from the PWIA curve (dotted line). For higher missing momenta, the shape of the tensor analyzing power is changed drastically by the final state interaction. This large and early deviation from the plane wave behaviour is caused by the fact that the final state interaction acts different on the different parts of the tensor analyzing power

$$A = 2\frac{W_+ - W_o}{2W_+ + W_o}, \tag{4.26}$$

i.e. on the momentum distribution for transversely polarized deuterons ($\mu = \pm 1$) and longitudinally polarized deuterons ($\mu = 0$). From the sign of the quadrupole deformation of the deuteron, which was measured experimentally [83], it is known that the deuteron's spin is aligned along the distance vector $\vec{r} = \vec{r}_n - \vec{r}_p$. The quantization axis is along the direction of the (e, e') momentum transfer $\vec{q}$, and the proton carries in good approximation this momentum $\vec{q}$ after the interaction with the photon in the hard vertex. Therefore, the probability of final state interaction is larger for the transverse polarization of the deuteron, where proton and neutron are aligned in $\vec{q}$ direction, than for the longitudinal polarization of the deuteron, where proton and neutron are aligned perpendicular to $\vec{q}$. The two cases are depicted in Fig. 4.8. The strong distortion of the tensor analyzing power by FSI again shows that the FSI effects cannot be described by a simple overall factor: if this was the case, the FSI effects in the tensor analyzing power would vanish.

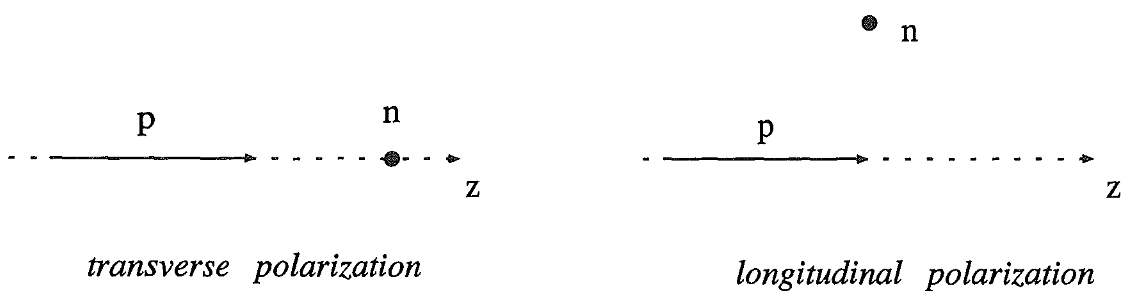

Figure 4.8: Sketch of the final state interaction in polarized deuteron targets for transverse polarization of the deuteron and longitudinal polarization of the deuteron.

The (p_m, θ) dependence of the tensor analyzing power naturally follows from the above described properties of the S- and D-wave amplitudes and $W_\mu(p_m, \theta)$. Fig. 4.4 shows a strong departure of $A(p_m, \theta)$ (solid curve) from the PWIA law $A \propto (1 - 3\cos^2\theta)$. In the PWIA (dotted curve), the tensor analyzing power has two zeroes at $\theta = 90^o \pm 35.3^o$. The results shown in Fig. 4.4 demonstrate how the FSI distortions change both the location and number of zeroes of $A(p_m, \theta)$.

The p_m dependence of $A(p_m, \theta)$ derives from the p_m dependence of the S- and

D-wave amplitudes. In contrast to the PWIA case, $A(p_m, \theta)$ does not vanish at $p_m = 0$, but numerically $|A(p_m = 0, \theta)| \ll 1$ and is hardly measurable. For the sake of definiteness, I consider in more detail perpendicular kinematics $\theta = 90^o$ (see Fig. 4.2, upper panel). With increasing p_m, $A(p_m, \theta)$ rises and has a maximum at $p_m \approx p_m^{(8)} = 1.19 fm^{-1}$, in the region of the dip in $W_o(p_m, \theta = 90^o)$. In contrast to $A^{PWIA}(p_m^{(2)}, \theta = 90^o)$ in PWIA (dotted line), $A(p_m^{(8)}, \theta = 90^o)$ does not saturate the bond $A = 1$. With the further increase of p_m, we encounter $A(p_m, \theta = 90^o) = \frac{1}{2}$ at $p_m^{(9)} = 1.42 fm^{-1}$, very close to the position of the FSI induced node in $Re\, s(\vec{p}_m)$. At still higher p_m, $A(p_m, \theta = 90^o)$ has two zeroes. The first zero, at $p_m = p_m^{(10)} = 1.70 fm^{-1}$ is the counterpart of the zero at $p_m = p_m^{(3)} = 2.73 fm^{-1}$ in PWIA, caused by the cancelation of S- and D-wave amplitudes when $d(p_m) \simeq -\sqrt{8} s(p_m)$. Such a strong shift of the location of this zero with respect to PWIA is due to the fact that $s(\vec{p}_m)$ is affected strongly by FSI and changes sign much sooner compared to the PWIA case. Compared to the PWIA case, the value of $p_m^{(10)}$ is affected also by different distortions of $d_\tau(\vec{p}_m)$ and by the contribution from $Im\, s(\vec{p}_m)$, $Im\, d_\tau(\vec{p}_m)$, see Eqs. (4.6),(4.7). The origin of the second zero at $p_m = p_m^{(11)} = 2.46 fm^{-1}$ is related to the FSI induced node of $Re\, d_o(\vec{p}_m)$ at $p_m = p_m^{(5)} = 2.87 fm^{-1}$. The inequality $p_m^{(11)} < p_m^{(5)}$ is an effect of the contribution to $A(p_m, \theta = 90^o)$ from $|d_2(\vec{p}_m)|^2$ (the contribution $\propto |d_1(\vec{p}_m)|^2$ is numerically very small), which makes $A > 0$ at $p_m = p_m^{(5)}$. At still larger p_m, where $W_\mu(p_m, \theta = 90^o)$ is dominated by the contribution from elastic np rescattering in the S-wave, the tensor analyzing power is positive, i.e. $W_+ > W_o$, for the above discussed larger probability of rescattering for $\mu = \pm 1$.

A comparison of the tensor analyzing power A calculated with the Bonn wave function (solid line) and the Paris wave function (dashed line) shows that the differences in the predictions including final state interaction are only marginal. Consequently, the tensor analyzing power does not seem to be an especially suitable observable for distinguishing between the different models, in contrast to the naive expectation.

4.6 Comparison of the Bonn and Paris Wave Functions

Comparison of the PWIA results from the Paris and Bonn wave functions in Fig. 4.9 shows a significant sensitivity of $N_\mu(p_m, \theta = 90^o)$ to the model of the deuteron wave function at large momentum. The PWIA tensor analyzing power shown in Fig. 4.2 exhibits similar model dependence at large p_m. FSI effects mask this sensitivity to the model of the wave function to a large extent, which naturally derives from the fact that $\Gamma(\vec{b})$ is a short ranged function compared to the deuteron wave function. For this reason, the FSI component of S- and D-wave amplitudes becomes fairly insensitive to details of the large p_m behaviour of the deuteron wave function. For instance, whereas in PWIA $N_o(p_m, \theta = 90^o)$ has a dip at $p_m^{(2)} = 1.50 fm^{-1}$ for the Paris wave function (dashed curve in Fig. 4.9b) and at $p_m^{(2)} = 1.58 fm^{-1}$ for the Bonn wave function (solid curve in Fig. 4.9b), with allowance for FSI a position of the dip of $W_o(p_m, \theta = 90^o)$ at $p_m = p_m^{(7)}$ is predicted very close for the Paris (dashed curve in Fig. 4.9a) and Bonn (solid curve in Fig. 4.9a) potentials: $p_m^{(7)} = 1.206 fm^{-1}$ and $p_m^{(7)} = 1.208 fm^{-1}$, respectively. This suggests that the actual value of $p_m^{(7)}$ is much more sensitive to the strength of the FSI rather than to the wave function.

The difference between $W_+(p_m, \theta = 90^o)$ for the Paris (dotted curve in Fig. 4.9a) and the Bonn (dash-dotted curve in Fig. 4.9a) wave functions also becomes marginal compared to the difference between the PWIA distributions shown in Fig. 4.9b. Because the position of the dip in $W_o(p_m, \theta = 90^o)$ is mostly controlled by FSI in the spin-triplet state with $\nu = 0$, one can think of using the high-statistics data on $^2\vec{H}(e, e'p)$ scattering on longitudinal deuterons in perpendicular kinematics for the evaluation of $\sigma_{tot}^{(o)} = \sigma_o + \frac{1}{2}\Delta\sigma_L - \Delta\sigma_T$. For instance, to check the sensitivity of FSI towards changes in the cross section, I repeated the calculation for $\sigma_{tot}^{(o)} = 30\, mb$, as predicted by Eq. (4.23) for $T_{kin} = 1\, GeV$, keeping the same value of ρ_o and b_o^2. The results for the Bonn wave function (solid line) and for the Paris wave function (dashed line) are shown in Fig. 4.10b. The dip is shifted to $p_m = 1.264 fm^{-1}$ and $1.270 fm^{-1}$ for the Paris and Bonn potentials, respectively. This shows that there is a minimal residual model dependence of the dip position. The shift of the dip position from $p_m^{(7)} \simeq 1.21 fm^{-1}$ to $p_m^{(7)} \simeq 1.27 fm^{-1}$ when the np cross section is changed from $40\, mb$ to $30\, mb$ is substantially larger than the difference between the results for Paris and Bonn potentials, and it is hard to distinguish the two curves in the dip region at all. Besides the position of the dip in $W_o(p_m, \theta = 90^o)$, the large p_m behaviour of $W_o(p_m, \theta = 90^o)$ is also sensitive to $\sigma_{tot}^{(o)}$. Namely, according to [14], the height of the $\theta = 90^o$ peak in $W_\mu(p_m, \theta)$ is proportional to $\left(\frac{\sigma_{tot}^{(o)}}{4\pi R_D^2}\right)^2$. The effect of the different normalization can be seen in Fig. 4.10a, where $W_o(\vec{p}_m)$ calculated with a value of $\sigma_{tot}^{(o)} = 40.4\, mb$ (solid line) and $\sigma_{tot}^{(o)} = 30\, mb$ (dashed line) is plotted.

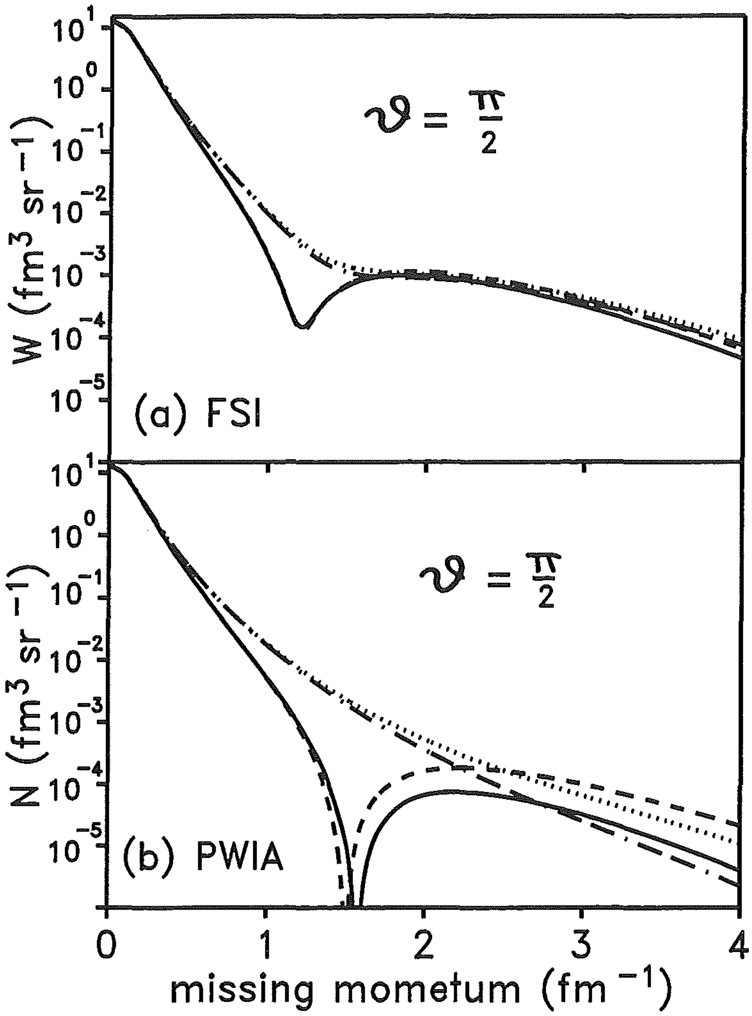

Figure 4.9: The momentum distributions calculated with the Bonn and Paris wave functions in PWIA (b) and including FSI (a) at $\theta = 90^o$. The results calculated with the Bonn wave function for W_o and N_o are shown by solid lines, W_+ and N_+ are shown by dash-dotted lines, the results calculated with the Paris wave function for W_o and N_o are shown by the dashed lines and for W_+ and N_+ are shown by dotted lines.

The smaller normalization when $\sigma_{tot}^{(o)} = 30\,mb$ is used leads to a slightly smaller tail at high missing momenta. Although the change in $\sigma_{tot}^{(o)}$ was quite large, the results are rather similar and differ both significantly from the PWIA result $N_o(p_m)$ (dotted line). The large p_m behaviour of this peak also depends on the as yet experimentally not measured diffraction slope for scattering in this specific spin state. However, the influence of changes in the diffraction slope on the missing momentum distribution

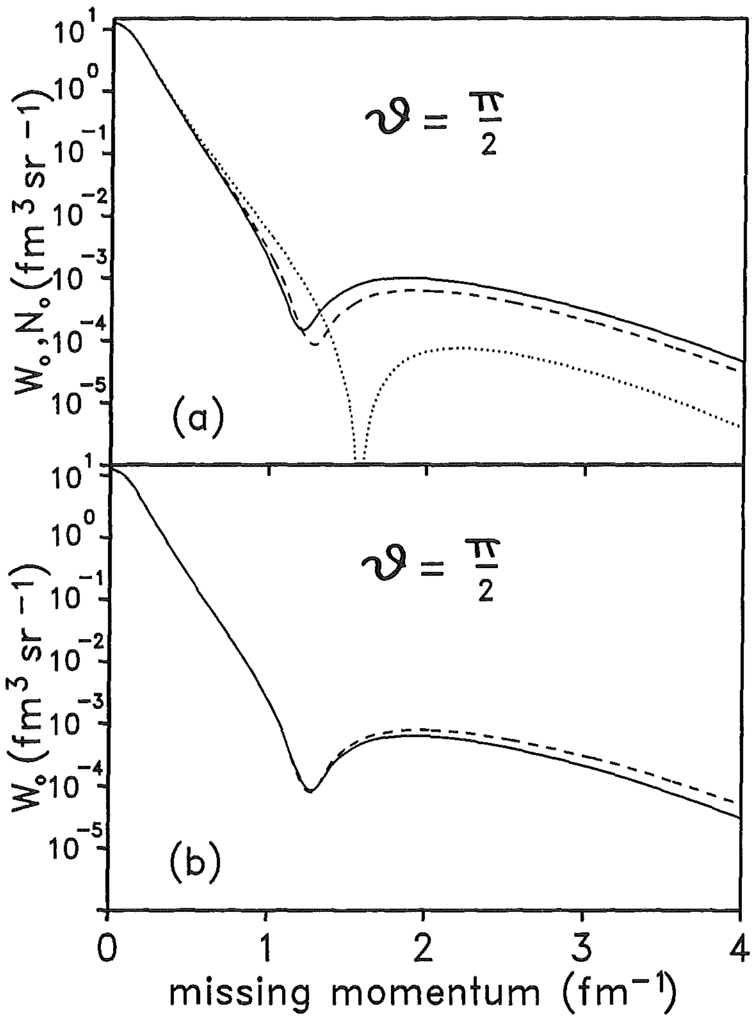

Figure 4.10: In a), the momentum distribution W_o calculated with the Bonn wave function in perpendicular kinematics is shown for $\sigma_{tot}^{(o)} = 40.4\,mb$ (solid line) and for $\sigma_{tot}^{(o)} = 30\,mb$ (dashed line). For comparison, the PWIA distribution calculated with the Bonn wave function is shown by the dotted line. In b), W_o calculated with $\sigma_{tot}^{(o)} = 30\,mb$ is shown for the Bonn wave function (solid line) and for the Paris wave function (dashed line).

is small, see Fig. 3.8. A more detailed analysis of the sensitivity of the dip position and of the elastic rescattering peak to $\Delta\sigma_L$, $\Delta\sigma_T$, and to values of ρ and b_o^2 for pure spin states $|\nu\rangle$ goes beyond the scope of this thesis. The results presented in Fig. 4.10 imply, however, that it will be a difficult task to distinguish different values of the cross section by experiment.

4.7 Tensor Polarization and Forward-Backward Asymmetry

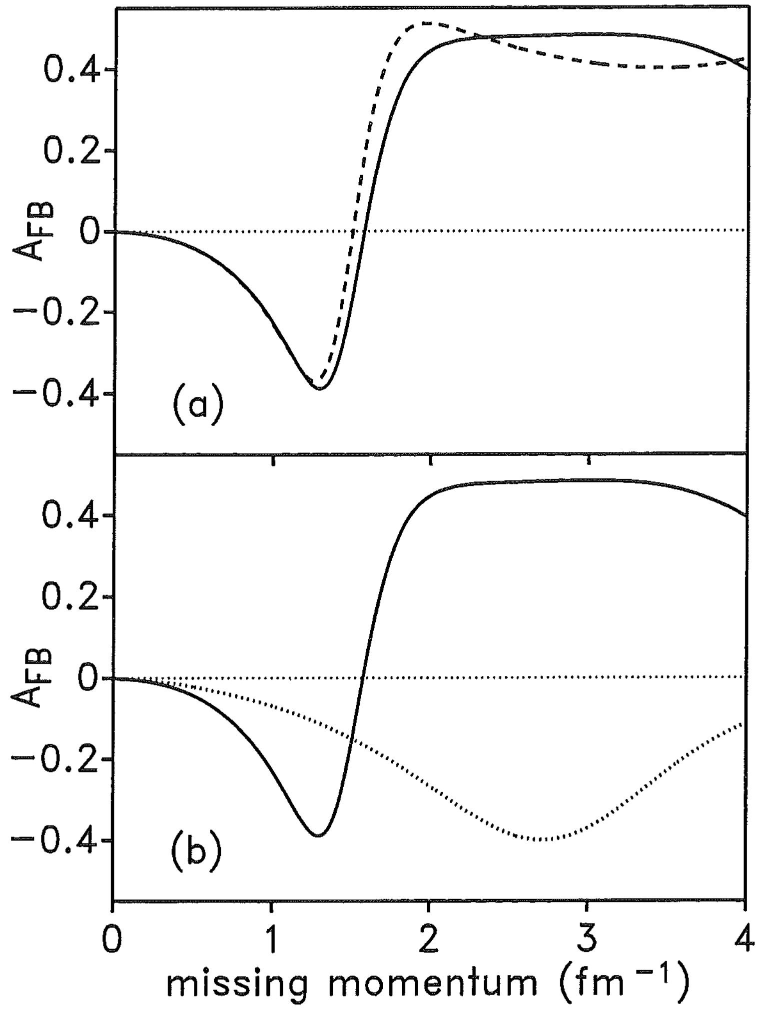

Figure 4.11: (a) The forward-backward asymmetry A_{FB} vs. p_m for W_+ calculated with the Bonn wave function (solid line) and the Paris wave function (dashed line). (b) The forward-backward asymmetry A_{FB} vs. p_m for W_+ (solid line) and W_o (dotted line) calculated with the Bonn wave function.

Above it was shown how FSI masks the effects due to the peculiarities of the unperturbed wave function of the deuteron. It is interesting that the forward-backward asymmetry

$$A_{FB}^{(\mu)} = \frac{W_\mu(\theta = 0^o, p_m) - W_\mu(\theta = 180^o, p_m)}{W_\mu(\theta = 0^o, p_m) + W_\mu(\theta = 180^o, p_m)} \tag{4.27}$$

is a pure PWIA-FSI interference effect caused by the nonvanishing elastic part of the p-n rescattering amplitude and as such is proportional to the PWIA amplitudes. Let's compare the amplitudes $\mathcal{M}_{\mu\nu}(\pm p_m)$ for a given initial spin state μ at $\theta = 0^o$ ($p_z = +p_m$) and $\theta = 180^o$ ($p_z = -p_m$): using $\theta(z) = \frac{1}{2}(1+\epsilon(z))$, where $\epsilon(z)$ is equal to +1 for $z > 0$ and -1 for $z < 0$, we have (we suppress the spin variables ν, μ, τ)

$$\begin{aligned}\mathcal{M}(\pm p_m) &= \int \Psi(\vec{r}) \exp(\pm i p_m z)\Big(1-(1-i\rho)G(\vec{b})\theta(z)\Big)d^2b dz \\ &= \mathcal{M}_{PWIA}(p_m) - (1-i\rho)\Big(F_c(p_m) \pm iF_s(p_m)\Big) \\ &= \mathcal{M}_{PWIA}(p_m) - F_c(p_m) \mp \rho F_s(p_m) + i\left(\rho F_c(p_m) \mp F_s(p_m)\right),\end{aligned} \tag{4.28}$$

where, using the fact that in our case $\Psi(\vec{r})$ is an even function of z,

$$\begin{aligned}\mathcal{M}_{PWIA}(\pm p_m) &\equiv \int_{-\infty}^{\infty} \Psi(\vec{r}) \exp(\pm i p_m z) d^2b dz \\ &= 2\int_0^{\infty} \Psi(\vec{r}) \cos(p_m z) d^2 b dz,\end{aligned} \tag{4.29}$$

$$F_c(p_m) \equiv \int_0^{\infty} \Psi(\vec{r})G(\vec{b}) \cos(p_m z) d^2 b dz, \tag{4.30}$$

$$F_s(p_m) \equiv \int_0^{\infty} \Psi(\vec{r})G(\vec{b}) \sin(p_m z) d^2 b dz. \tag{4.31}$$

Then one obtains

$$\begin{aligned}A_{FB}^{(\mu)} &= \frac{W_\mu(+p_m) - W_\mu(-p_m)}{W_\mu(+p_m) + W_\mu(-p_m)} = \frac{1}{(2\pi)^3}\frac{\sum_\tau \{|\mathcal{M}(p_m)|^2 - |\mathcal{M}(-p_m)|^2\}_{\mu,\tau}}{W_\mu(+p_m) + W_\mu(-p_m)} \\ &= -4\rho\frac{1}{(2\pi)^3}\frac{\sum_\tau \{\mathcal{M}_{PWIA}(p_m)F_s(p_m)\}_{\mu,\tau}}{W_\mu(+p_m) + W_\mu(-p_m)},\end{aligned} \tag{4.32}$$

where the sum over τ is a reminder that for the chosen deuteron polarization μ different combinations of $s(\vec{p}_m)$ and $d_\tau(\vec{p}_m)$ enter the matrix element according to Eqs. (4.6),(4.7). Because of $F_s(p_m) \to 0$ at $p_m \to 0$, see Eq. (4.31), $A_{FB}^{(\mu)}$ vanishes at $p_m \to 0$.

In the generic case, both the S-wave and D-wave amplitudes with $\tau = \pm 2, \pm 1, 0$ contribute to $A_{FB}^{(\mu)}$. The situation greatly simplifies for transverse deuterons, polarized along the z axis, $\mu = \pm 1$. In this case, D-waves with $|\tau| = 1, 2$ do not contribute to $A_{FB}^{(+)}$, because the corresponding PWIA amplitudes (4.10) vanish at $\theta = 0^o, 180^o$.

Consequently, only the term with $\tau = 0$ contributes to the numerator in (4.32), and the relevant PWIA amplitude equals

$$\mathcal{M}^{(\tau=0)}_{PWIA} = \sqrt{4\pi}\left(s(p_m) - \frac{1}{\sqrt{2}}d(p_m)\right) . \tag{4.33}$$

Therefore, it is predicted that $A^{(+)}_{FB}$ has a node at precisely $p_m = p^{(2)}_m$ and the location of this node is not affected by FSI. This provides a unique possibility of experimental determination of $p^{(2)}_m$, which is important for testing models of the deuteron wave function. The sensitivity to the model of the deuteron is demonstrated in Fig. 4.11b, where $A^{(+)}_{FB}$ is compared for the Bonn and the Paris wave functions. Notice the very steep p_m-dependence of $A^{(+)}_{FB}$ around the node. Eqs. (4.30),(4.31) show that while $F_c(p_m)$ decreases with p_m, $F_s(p_m)$ first rises with p_m. As a matter of fact, in spite of the FSI suppression factor $\sim (\frac{b_o}{R_D})^2$, $F_s(p_m)$ is quite large in the vicinity of the node and gives rise to a peak in $A^{(+)}_{FB}$ at $p_m \approx 1.3 fm^{-1}$.

For the longitudinal deuterons, $\mu = 0$, the corresponding PWIA amplitudes do not have any interesting nodal structure, see Fig. 4.1d, which shows quite a structureless $N_o(p_m, \theta = 0^o, 180^o)$ (solid line). Correspondingly, $A^{(0)}_{FB}$ does not exhibit any structure at $p_m \lesssim (3-4) fm^{-1}$.

In this chapter, an analysis of effects of the quadrupole deformation of the deuteron in ${}^2\vec{H}(e,e'p)n$ scattering on tensor-polarized deuterons has been carried out. Because the final state interaction is sensitive to the alignment of the deuteron, FSI effects depend strongly on the tensor polarization of the deuteron, which leads to a very rich pattern of the angular and p_m dependence of momentum distributions and tensor analyzing power. In the tensor analyzing power A, FSI effects turn out to be substantial at a relatively small missing momentum $p_m \gtrsim (0.9 - 1.0) fm^{-1}$ both in perpendicular and (anti)parallel kinematics. In perpendicular kinematics, for the longitudinal deuteron $\mu = 0$, one finds that FSI shifts the dip of the momentum distribution from $p_m = 1.58 fm^{-1}$ to $p_m = 1.21 fm^{-1}$. For transverse deuterons, $\mu = \pm 1$, FSI produces a shoulder-like structure in $W_+(p_m, \theta = 90^o)$ as compared to a monotonous decrease of $N_+(p_m, \theta = 90^o)$ in PWIA. At large $p_m \gtrsim 2.5 fm^{-1}$, the elastic rescattering peak in $W_+(p_m, \theta = 90^o)$ is stronger than in $W_o(p_m, \theta = 90^o)$, in agreement with the expectation that the experimentally known sign of the quadrupole deformation of the deuteron makes the probability of rescattering of the struck proton on the spectator neutron larger for $\mu = \pm 1$.

Only at small $p_m \approx 0$ the departure of the nuclear transparency ratio $T_\mu(p_m, \theta) =$

$\frac{W_\mu(p_m,\theta)}{N_\mu(p_m,\theta)}$ from unity is small, $T_\mu(p_m,\theta) \simeq 0.93$. At larger p_m, in the region of strong PWIA-FSI interference, one finds both $T_\mu(p_m,\theta) \ll 1$ and $T_\mu(p_m,\theta) \gg 1$. The antishadowing effect $T_\mu(p_m,\theta) > 1$ is particularly strong in perpendicular kinematics.

In PWIA, the tensor analyzing power exhibits substantial sensitivity to models of the deuteron wave function at large p_m. FSI effects mask this sensitivity to a large extent. A unique observable, which provides an FSI independent probe of the nodal structure of the combination of S- and D-wave functions $s(p_m) - \frac{1}{\sqrt{2}}d(p_m)$, is the forward-backward asymmetry $A_{FB}^{(+)}$ for transverse deuterons $\mu = \pm 1$. The asymmetry $A_{FB}^{(\mu)}$ is a pure PWIA-FSI interference effect and has its origin in the nonvanishing real part of the np scattering amplitude. None the less, $A_{FB}^{(+)}$ is shown to be proportional to $s(p_m) - \frac{1}{\sqrt{2}}d(p_m)$, and the node of $A_{FB}^{(+)}(p_m)$ is predicted to coincide with the node of the PWIA amplitude $s(p_m) - \frac{1}{\sqrt{2}}d(p_m)$. The potential sensitivity of FSI effects to the spin triplet np total cross section was explored and shown to be small. A very precise measurement of $W_o(\vec{p}_m, \theta = 90^o)$ might shed some light on the values of $\Delta\sigma_T$ and $\Delta\sigma_L$, as the dip position in $W_o(\vec{p}_m, \theta = 90^o)$ is determined by the total spin-dependent pn cross section σ_{tot}.

In conclusion, interpretation of the experimental data on $^2\vec{H}(e,e'p)$ scattering on tensor polarized deuterons at missing momenta $p_m \gtrsim (0.9 - 1.0) fm^{-1}$requires an accurate evaluation of FSI effects which depend strongly on the spin state of the deuteron and on the scattering kinematics. For this, one needs better experimental data on $\vec{N}\vec{N}$ scattering.

Chapter 5

Electron Scattering on ^4He

In the previous chapters, electron scattering from deuterons has been investigated. As there are several realistic deuteron wave functions available in parameterized form, the deuteron is an ideal testing ground for the calculation of the final state interaction effects: no additional assumptions about the ground state wave function enter the calculation. Now, as a good understanding of the final state interaction effects is established, I proceed with the investigation of electron scattering on heavier nuclei. A very suitable nucleus for this investigation is ^4He, as it is a tightly bound nucleus, which is expected to have similar properties as heavier nuclei. Especially, its momentum distribution should resemble the momentum distributions for heavier nuclei. Therefore, there are good reasons to believe that an exhaustive analysis of FSI effects in ^4He gives a good guidance to the significance of FSI effects in heavier nuclei.

Currently, the ^4He wave functions are not available in parameterized form and they are obtained only with a considerable numerical effort by Monte Carlo calculations (see, e.g. [23]), by solving the Faddeev equations (see, e.g. [21]), or by the hyper-spherical harmonic expansion method (see, e.g. [22]). As the calculation of the final state interaction itself is quite involved, those wave functions cannot be used in the calculations presented here. Furthermore, the most interesting phenomena take place at large missing momentum, where higher order terms in the cluster expansion for the momentum distribution become quite important and a very tight control of the numerical accuracy is necessary. Despite the small number of nucleons in ^4He, the full cluster expansion in correlation function and final state interaction operator includes a very large number of terms. For this reason, at this exploratory stage, I employ a simple model wave function. The actual calculations can be carried out for an arbitrarily large missing momentum if a suitable form of the wave function is chosen which allows a semi-analytic evaluation of the missing momentum distribution. A calculation of this type to all orders in the correlations and final state interactions has been carried out in [18] for the first time. The obtained results do not depend on the details of this wave function, and its simple form makes a semi-analytic evaluation of the integrals feasible. The results of this chapter can be found in [15] and [18].

5.1 The Missing Momentum Distribution

For the longitudinal response, the reduced nuclear amplitude for the exclusive process $^4He(e,e'p)A_f$ equals

$$\mathcal{M}_f = \int d\vec{R}_1\, d\vec{R}_2\, d\vec{R}_3 \Psi_f^*(\vec{R}_1,\vec{R}_2)\hat{S}(\vec{r}_1,...,\vec{r}_4)\Psi(\vec{R}_1,\vec{R}_2,\vec{R}_3)\exp(i\vec{p}_m\vec{R}_3)\,. \tag{5.1}$$

Here $\Psi(\vec{R}_1,\vec{R}_2,\vec{R}_3)$ and $\Psi_f(\vec{R}_1,\vec{R}_2)$ are wave functions of the target ^4He nucleus and of the specific 3-body final state A_f, which are conveniently described in terms of the Jacobi coordinates $\vec{R}_1=\vec{r}_2-\vec{r}_1$, $\vec{R}_2=\frac{2}{3}\vec{r}_3-\frac{1}{3}(\vec{r}_1+\vec{r}_2)$, $\vec{R}_3=\vec{r}_4-\frac{1}{3}(\vec{r}_1+\vec{r}_2+\vec{r}_3)$ (plus $\vec{R}_{cm}=\frac{1}{4}\sum_i\vec{r}_i\equiv 0$). Lab coordinates $\{\vec{r}_i(\vec{R}_j,\vec{R}_{cm})\}$ are also used when appropriate. The specific expression (5.1) for $\mathcal{M}_f$ corresponds to the nucleon "4" of ^4He being chosen for the detected struck proton. $\hat{S}(\vec{r}_1,...,\vec{r}_4)$ stands for the S-matrix of the FSI of the struck proton with three spectator nucleons.

The calculation of the full FSI-modified spectral function $S(E_m,\vec{p}_m)$ is a separate problem, as the wave functions for the final three-nucleon state are required for its calculation. In this exploratory study of the salient features of FSI, I focus on the inclusive missing momentum spectrum of protons in $^4He(e,e'p)$ scattering in quasielastic kinematics

$$W(\vec{p}_m) = \frac{1}{(2\pi)^3}\int dE_m S(E_m,\vec{p}_m) = \frac{1}{(2\pi)^3}\sum_f |\mathcal{M}_f|^2 \tag{5.2}$$

The sum over all the allowed final states A_f for the three undetected nucleons can be performed making use of the closure relation

$$\sum_f \Psi_f(\vec{R}_1{}',\vec{R}_2{}')\Psi_f^*(\vec{R}_1,\vec{R}_2) = \delta(\vec{R}_1-\vec{R}_1{}')\delta(\vec{R}_2-\vec{R}_2{}')\,. \tag{5.3}$$

This leads to the missing momentum distribution

$$W(\vec{p}_m) = \frac{1}{(2\pi)^3}\int d\vec{R}_3{}' d\vec{R}_3 \rho(\vec{R}_3,\vec{R}_3{}')\exp\left[i\vec{p}_m(\vec{R}_3-\vec{R}_3{}')\right]\,, \tag{5.4}$$

where

$$\rho(\vec{R}_3, \vec{R}_3{}') = \int d\vec{R}_1\, d\vec{R}_2\, \Psi^*(\vec{R}_1, \vec{R}_2, \vec{R}_3{}') S^\dagger(\vec{r}_1{}'..,\vec{r}_4{}') S(\vec{r}_1, ..., \vec{r}_4) \Psi(\vec{R}_1, \vec{R}_2, \vec{R}_3) \tag{5.5}$$

is the FSI-modified one-body density matrix (OBDM). In PWIA, when $\hat{S}(\vec{r}_1, ..., \vec{r}_4) = 1$, Eq. (5.5) reduces to the standard one-body density matrix of a nucleus and Eq. (5.4) gives the PWIA missing momentum distribution $N(k)$, also referred to as single particle momentum distribution (SPMD). Extensive studies of $N(k)$ are available in the literature ([66, 84] and references therein, see also the monograph [85]).

An accurate incorporation of FSI effects into the calculation of the momentum distribution $W(\vec{p}_m)$, Eq. (5.4), is a numerically very involved problem. For this reason, in this exploratory study of FSI effects, I use a simple, yet realistic, parameterization of the wave function, which allows a semi-analytic evaluation of $W(\vec{p}_m)$. Namely, I employ the frequently used Ansatz consisting of a harmonic oscillator mean field wave function Ψ_o and a Jastrow correlation factor $\hat{F}$ to allow for the effects of the correlations in the ground state,

$$\Psi(\vec{R}_1, \vec{R}_2, \vec{R}_3) \equiv \hat{F}\, \Psi_o(\vec{R}_1, \vec{R}_2, \vec{R}_3), \tag{5.6}$$

where

$$\hat{F} \equiv \prod_{i<j}^{4} \left[1 - C(\vec{r}_i - \vec{r}_j)\right], \tag{5.7}$$

$$\Psi_o \propto \exp\left[-\frac{1}{2R_o^2}\sum_i^4 \vec{r}_i{}^2\right] = \exp\left[-\frac{1}{4R_o^2}\left(\vec{R}_1{}^2 + 3\vec{R}_2{}^2 + \frac{3}{2}\vec{R}_3{}^2\right)\right] \tag{5.8}$$

and

$$C(r) = C_o \exp\left(-\frac{r^2}{2r_c^2}\right). \tag{5.9}$$

For a hard core repulsion of the nucleons $C_o = 1$, for a soft core $C_o < 1$. In the literature, one usually considers the correlation radius $r_c \approx 0.5$-$0.6\, fm$ [84, 85, 86, 87, 88]. The exact value of the correlation radius is not known; an upper limit is given by the charge radius of the proton of $r_{charge} = 0.8\, fm$ [89], the correlation radius is certainly smaller. The radius R_o of the oscillator wave function can be determined from the charge radius of the ^4He, from which one must subtract the contribution due to the finite charge radius of the proton. For instance, for a hard core repulsion, $C_o = 1$, and $r_c = 0.5\, fm$, the experimentally measured charge radius of the ^4He [89] is reproduced with $R_o = 1.29\, fm$. Notice that the "correlation volume" r_c^3 is a very small fraction of the volume of a nucleus and one has the strong inequality $(r_c/R_0)^3 \ll 1$.

5.2 Short Range Correlations and Single Particle Momentum Distribution

In order to set up a background, I start with a discussion of the short range correlation (SRC) effects in the SPMD $N(\vec{p}_m)$. Here one has to evaluate the conventional OBDM

$$\rho(\vec{R}_3, \vec{R}_3{}') = \int d\vec{R}_1\, d\vec{R}_2\, \Psi_o^*(\vec{R}_1, \vec{R}_2, \vec{R}_3{}')\hat{F}^\dagger(\vec{r}_1{}'.., \vec{r}_4{}')\hat{F}(\vec{r}_1, ..., \vec{r}_4)\Psi_o(\vec{R}_1, \vec{R}_2, \vec{R}_3) \tag{5.10}$$

The product of the Jastrow functions in (5.10) can be expanded as

$$\hat{F}^\dagger\hat{F} = \prod_{i<j}^{4}\left[1 - C^\dagger(\vec{r}_i{}' - \vec{r}_j{}')\right]\left[1 - C(\vec{r}_i - \vec{r}_j)\right] =$$
$$1 - \sum_{i<j}\left[C^\dagger(i' - j') + C(i - j)\right] + \sum C^\dagger C + \sum C^\dagger C^\dagger + \sum CC + \cdots \tag{5.11}$$

The cluster expansion (5.11) gives rise to 2^{12} terms in the integrand of the OBDM in Eq. (5.10), but with the considered Ansatz wave function it is possible to carry out all the integrations in the OBDM and in the SPMD analytically. Here I present a brief summary of main effects of short range correlations in the SPMD (for the related earlier works see [84, 85, 86], the more refined form of the above approximation known as the correlated basis function theory is widely being applied to SPMD in heavier nuclei ([88] and references therein)).

Although the number of terms in the expansion Eq. (5.11) is large, one can classify each term according to the number of correlations it contains and investigate its importance for the interesting region of higher missing momenta. To the zeroth order in the correlation function, one has the "mean field" term, which leads to the long ranged OBDM

$$\rho_0(\vec{R}, \vec{R}') = w_1 \frac{27}{512}\frac{1}{\pi^3}\frac{1}{R_0^6}\exp\left(-\frac{3}{8R_o^2}\left(\vec{R}^{\,2} + \vec{R}'^{\,2}\right)\right) \tag{5.12}$$

(where I have introduced $\vec{R} \equiv \vec{R}_3$ and $\vec{R}' \equiv \vec{R}_3'$ for brevity) and the steeply decreasing SPMD

$$N(1; \vec{p}_m) = w_1 \exp\left(-\frac{4}{3}R_o^2 p_m^2\right), \tag{5.13}$$

falling off rapidly for momenta larger than the Fermi momentum $k_F \sim 1/R_0$, showing the typical mean field behaviour. To this lowest order the normalization is given by $w_1 = R_o^3(4/3\pi)^{3/2}$. (Hereafter $N(1;\vec{p}_m)$, $N(C;\vec{p}_m)$,... indicate the contributions to $N(\vec{p}_m)$ coming from the "1","C",... terms in the expansion (5.11)). Note that in any PWIA calculation, with or without correlations, the SPMD is isotropic and depends only on $|\vec{p}_m|$.

The higher order terms in $C, C^\dagger$ in (5.11) can be considered as "interactions" which modify the one-body density matrix $\rho_0(\vec{R},\vec{R}')$ of the mean field approximation. This is shown schematically in Fig. 5.1. The first order corrections to $\rho(\vec{R},\vec{R}')$ and $N(\vec{p}_m)$ come from the terms which are linear in $C(\vec{r_i}-\vec{r_j})$ and $C^\dagger(\vec{r_i}\,'-\vec{r_j}\,')$. Leading corrections to $N(\vec{p}_m)$, which decrease slower with p_m the zeroth order term (5.13), come from interactions of Fig. 5.1a, which affect only one of the trajectories in the calculation of the OBDM. The corresponding corrections to the OBDM are long-ranged, and lead to a contribution to the single particle momentum distribution of the form

$$N(C^\dagger + C;\vec{p}_m) \approx -6w_1C_0\sqrt{\frac{27}{125}}\left(\frac{r_c}{R_o}\right)^3 \exp\left(-\frac{4}{5}R_o^2p_m^2\right). \tag{5.14}$$

For the sake of brevity, I don't show here and in the following equations correction factors $[1+\mathcal{O}(r_c^2/R_o^2)]$ to the slope and the normalization factors. Of course, those factors and the corresponding renormalization of w_1 are included in the calculations. The normalization in (5.14) contains the small factor $(r_c/R_0)^3$. This factor appears with each three-dimensional integration over the correlation function. The p_m dependence of the term linear in the correlation function is similar to that of the mean field term, just that the slope is slightly smaller in Eq. (5.14), which makes the $N(C^\dagger + C)$ term larger than the mean field term at intermediate missing momenta around the Fermi momentum k_F. In this region, the destructive interference between the mean field term $N(1;\vec{p}_m)$ and the term linear in the correlations $N(C^\dagger + C;\vec{p}_m)$ is strong.

The driving contributions to the short ranged component of the OBDM and therefore to the related large-p_m component of the SPMD come from the three identical terms of the form $C^\dagger(\vec{r}_4\,'-\vec{r}_i\,')C(\vec{r}_4-\vec{r}_i)$. They produce a short range interaction of the type shown in Fig. 5.1b between the two trajectories which enter the calculation of the OBDM and lead to a short ranged component of the OBDM of the form

$$\rho(C^\dagger C,\vec{R},\vec{R}') = 3\int d^3\vec{R}_1 d^3\vec{R}_2\,\Psi_o\Psi_o'\,C^\dagger(\vec{r_3}'-\vec{r_4}')\,C(\vec{r_3}-\vec{r_4})$$

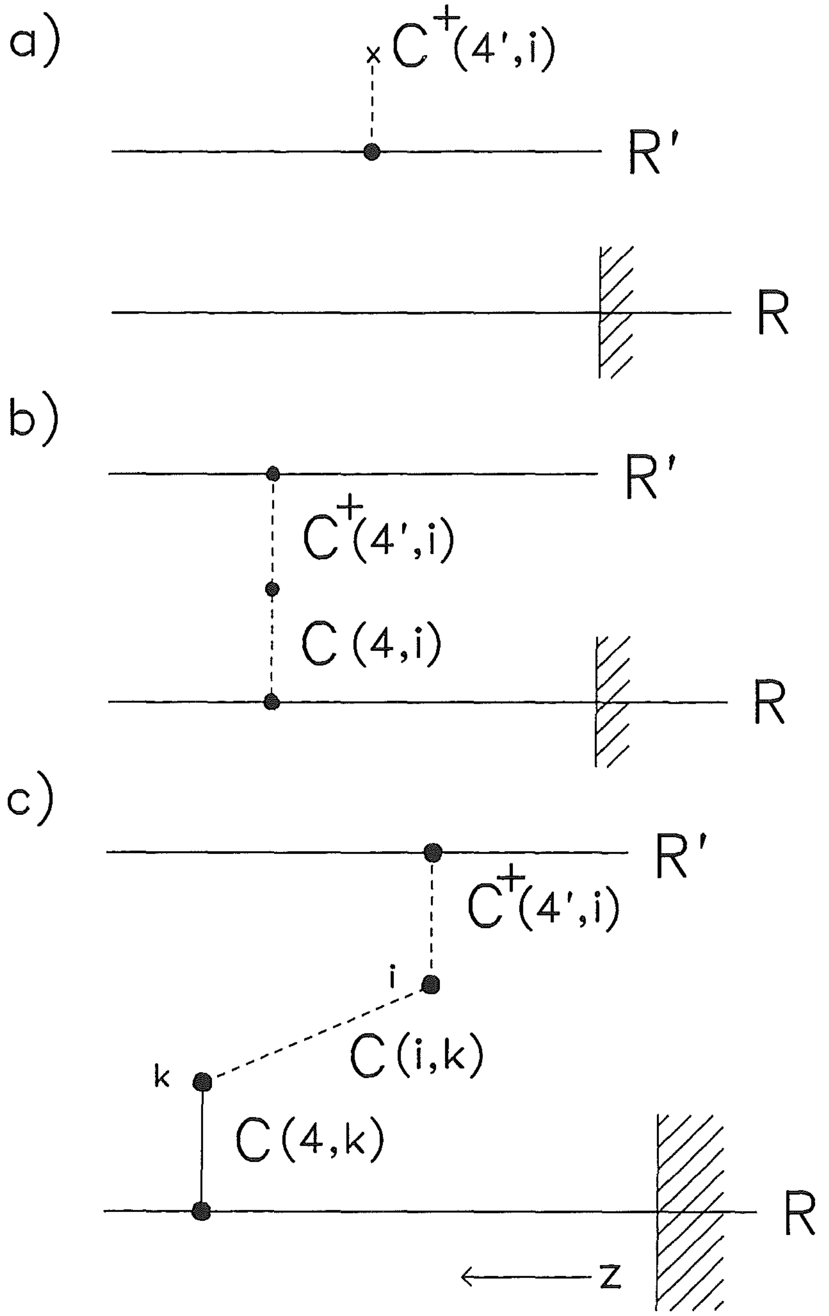

Figure 5.1: Schematic diagrams of several contributions to the one-body density matrix containing correlations. a) a linear correlation term of the type $C^\dagger(\vec{r}_i{}' - \vec{r}_4{}')$, b) the quadratic contribution $C^\dagger(\vec{r}_i{}' - \vec{r}_4{}')\, C(\vec{r}_i - \vec{r}_4)$ and c) a cyclic third order contribution of the type $C^\dagger(\vec{r}_4{}' - \vec{r}_i{}')\, C(\vec{r}_i - \vec{r}_k)\, C(\vec{r}_k - \vec{r}_4)$.

$$\approx w_1 C_o^2 \frac{1}{\pi^3} \sqrt{\frac{3^{11}}{2^{21}}} \frac{r_c^3}{R_o^9} \exp\left(-\frac{1}{4r_c^2}\left(\vec{R}-\vec{R}'\right)^2 - \frac{9}{8R_o^2}\left(\vec{R}^2+\vec{R}'^2\right)\right) . \quad (5.15)$$

The resulting large-p_m component of the SPMD directly probes the correlation function $C(\vec{R})$:

$$N(C^\dagger C;\vec{p}_m) \approx w_1 C_o^2 \frac{1}{2\pi^3} \frac{1}{R_o^6} \sqrt{\frac{243}{512}} \left| \int d^3\vec{r} C(\vec{r}) \exp(i\vec{p}_m\vec{r}) \right|^2$$
$$= N(C^\dagger C;\vec{p}_m) \approx w_1 C_o^2 \sqrt{\frac{243}{512}} \left(\frac{r_c}{R_o}\right)^6 \exp\left(-r_c^2 p_m^2\right) . \quad (5.16)$$

Notice that the large-p_m tail of the SPMD contains the small normalization factor $\propto (r_c/R_o)^6$ due to the integration over the two correlation functions. In spite of this small normalization, the contribution $N(C^\dagger C)$ is dominant at large missing momenta: the slope r_c^2 is much smaller than the slopes $\approx R_o$ of the mean field term and the linear correlation term, it therefore contributes at large missing momenta where the other terms have already vanished.

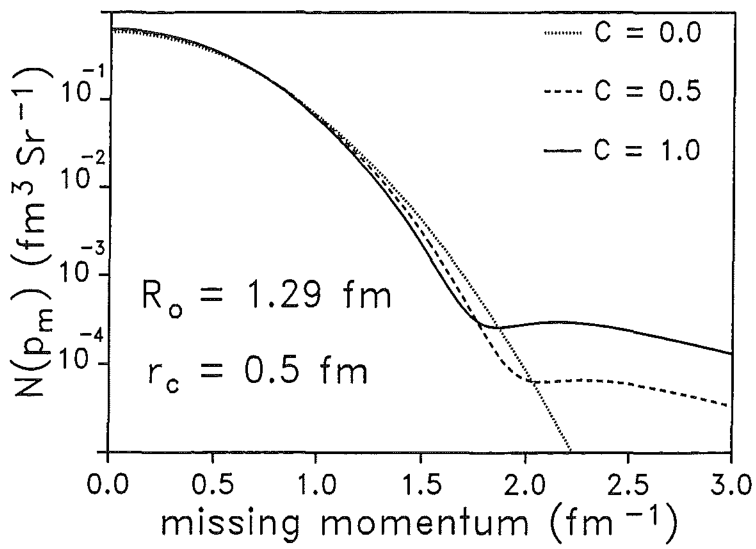

Figure 5.2: The single particle momentum distribution (SPMD) for the mean field distribution $C_o = 0$ (dotted curve), for soft core correlations $C_o = 0.5$ (dashed curve) and for hard core correlations $C_o = 1$ (solid curve). The other parameters are $R_o = 1.29fm$ and $r_c = 0.5fm$.

The correlated pair of nucleons is often treated as a quasi-deuteron ([42, 43, 66] and references therein). Indeed, Eq. (5.16) resembles the momentum distribution in the quasi-deuteron with the short-range correlation function playing the rôle of the wave function of the quasideuteron.

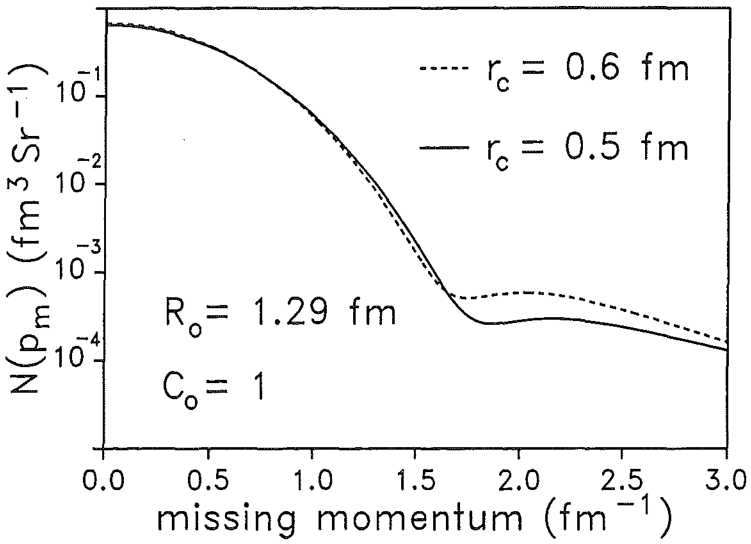

Figure 5.3: The single particle momentum distribution (SPMD) for different values of the correlation radius r_c. The solid curve shows $r_c = 0.5fm$ and the dashed curve shows $r_c = 0.6fm$. The other parameters are $R_o = 1.29fm$ and $C_o = 1$.

The terms $\propto CC, C^\dagger C^\dagger$ in expansion (5.11) correspond to interactions which involve only one of the trajectories in $\rho(\vec{R}, \vec{R}')$ and give a long ranged contribution to the OBDM and a steeply decreasing contribution to the SPMD $N(\vec{p}_m)$, similar to (5.13),(5.14). The above analysis can easily be extended to still higher order effects in the correlation function. For instance, the cyclic terms of the form $C^\dagger(\vec{r}_4 - \vec{r}_3)C(\vec{r}_4{}' - \vec{r}_2{}')C(\vec{r}_2 - \vec{r}_3)$ also lead to a short-range interaction between the two trajectories in the OBDM, as shown in Fig. 5.1c. For the presence of the extra link in the 4-2-3 chain, though, the corresponding interaction range is larger than in the diagram of Fig. 5.1b, and the resulting contribution from such cyclic terms to the SPMD has a p_m dependence steeper than in Eq. (5.16):

$$N(\left[C^\dagger CC + C^\dagger C^\dagger C\right]_{cyclic}; \vec{p}_m) \approx -6w_1 C_o^3 \sqrt{\frac{1}{8}} \left(\frac{r_c}{R_o}\right)^9 \exp(-\frac{3}{2} r_c^2 p_m^2) \qquad (5.17)$$

However, numerically more important are the non-cyclic third order terms of the form $C^\dagger(\vec{r}_4{}' - \vec{r}_i{}')C(\vec{r}_4 - \vec{r}_i)C^\dagger(\vec{r}_j - \vec{r}_k)$, which have a slow p_m^2 dependence equal to that of the leading $C^\dagger C$ contribution (5.15) but are of the opposite sign:

$$N(\left[C^\dagger CC + C^\dagger C^\dagger C\right]_{non-cyclic}; \vec{p}_m) \approx -10 w_1 C_o^3 \sqrt{\frac{243}{512}} \left(\frac{r_c}{R_o}\right)^9 \exp\left(-r_c^2 p_m^2\right) . \quad (5.18)$$

Such a destructive interference between the $C^\dagger CC + C^\dagger C^\dagger C$ and $C^\dagger C$ contributions to the SPMD demonstrates a well understood suppression of interaction between any pair of nucleons for the repulsive correlation with surrounding nucleons, for more discussion see below.

The above considerations are illustrated by the numerical results displayed in Figs. 5.2,5.3,5.4,5.5. The sensitivity of the SPMD to short range correlations is obvious from a comparison of the mean field distribution, $C_o = 0$, with the soft core correlation $C_o = 0.5$ and the hard core correlation $C_o = 1$ in Fig. 5.2. For $C_o = 0$, the mean field momentum distribution (5.13) falls off rapidly for $p_m \gtrsim k_F \sim 1/R_o$. Once the short range correlations are included, the large-p_m tail builds up. Its strength is $\propto C_o^2$. The effect of destructive interference between the mean field SPMD (5.13) and the lowest order correlation contribution (5.14) is obvious at intermediate $p_m \sim k_F$. The interference effect rises with the correlation strength C_o. One usually considers $r_c \sim 0.5\,fm$, but the exact value of the correlation radius r_c is not known precisely [84, 86, 87]. According to Eq. (5.16), the most important quadratic correlation contribution to the single particle momentum distribution rises steeply, $\propto r_c^6$, with the correlation radius r_c. However, at large values of p_m where the short range correlation component becomes more important than the mean field component, the suppression by the factor $\exp(-r_c p_m^2)$ is quite significant and the residual sensitivity to the variation of r_c is weaker than $\propto r_c^6$. This is illustrated by Fig. 5.3, where we compare the momentum distributions for $r_c = 0.5\,fm$ and $r_c = 0.6\,fm$.

Above I cited the explicit form of leading terms in the SPMD. The rate of convergence of the expansion in powers of the correlation function is of great interest on its own. For instance, the large-p_m tail of the SPMD is often discussed in terms of the quasi-deuteron configurations, neglecting the effect of the nuclear surrounding. If this were a good approximation, then one would have expected a universality of the large-p_m single particle momentum distributions for all nuclei. The accuracy of this approximation can be judged from Fig. 5.4, where I present the results for $N(p_m)$ including all terms up to the second order, i.e., $C^\dagger C^\dagger + C^\dagger C + CC$ (dotted line), to the fourth order (dashed line), to the sixth order (dash-dotted line), to the eighth order (double-dotted line), and the full cluster expansion (5.11) up to the twelfth order terms (solid line) is plotted. All the different single-particle momentum distributions are normalized to unity. Although the shape of the SPMD does not change qualitatively, we find a substantial, $\sim 40\%$, renormalization of the lowest-order quasi-deuteron contribution to $N(\vec{p}_m)$ by effects of the nuclear environment. This shows that the large-p_m behaviour of the SPMD is sensitive to details of

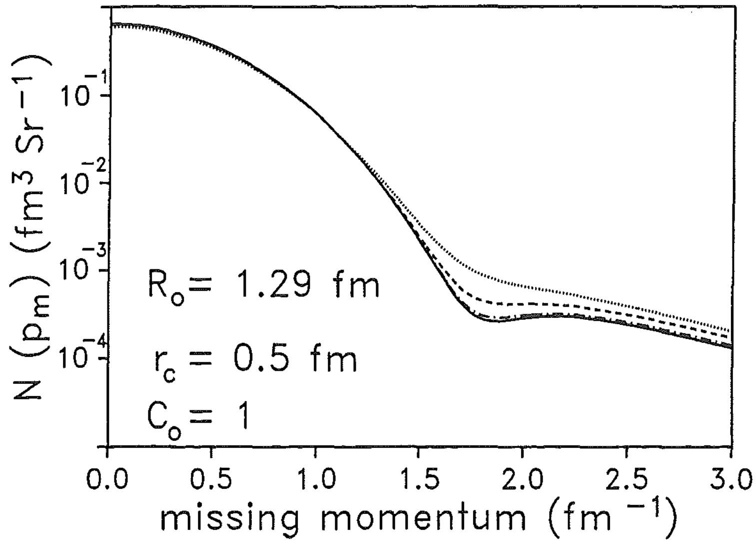

Figure 5.4: The convergence behaviour of the single particle momentum distribution for $R_o = 1.29fm$, $r_c = 0.5fm$ and $C_o = 1$. The dotted line includes all terms up to second order, the dashed line includes all terms up to fourth order, the dash-dotted line shows all terms up to sixth order, the double-dotted line includes all terms up to eighth order and the solid line shows the full calculation, i.e. it includes all terms up to twelfth order.

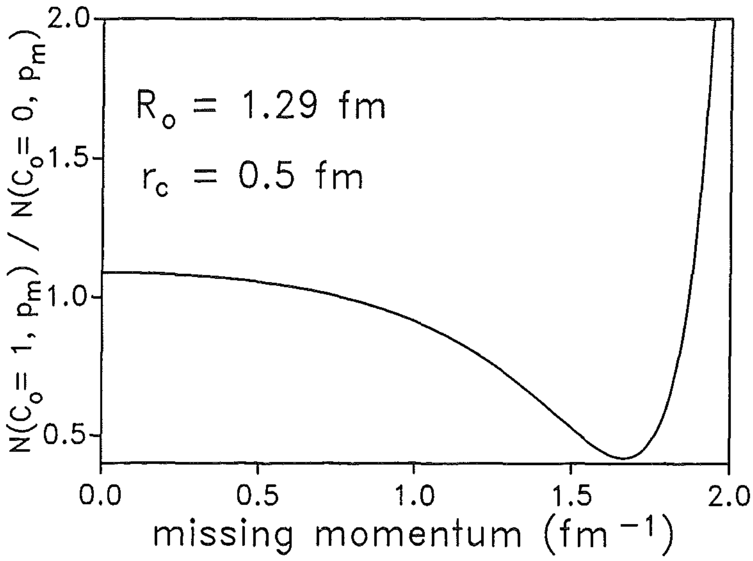

Figure 5.5: The pattern of renormalization of the SPMD due to the short range correlations represented by the renormalization factor R_C as defined in Eq. (5.19).

the nuclear wave function and a quasi-deuteron universality of the SPMD at large p_m is though a reasonable, but not a very accurate, approximation. The effect of higher order corrections is evident from the form of the Jastrow correlation factor: the mutual repulsion from surrounding nucleons suppresses the probability of short distance interaction between any pair of nucleons in the nucleus, cf. Eqs. (5.16) and (5.17),(5.18). The effect of higher order terms is particularly important at intermediate values of $p_m \sim k_F \sim 1/R_0$, where the model SPMD develops a slight minimum. The model wave function employed here contains only those many-nucleon correlation effects, which are reducible to higher orders in the pair correlation function. The fact that terms up to sixth order are non-negligible at large p_m, suggests that the at present poorly known pair-irreducible multinucleon correlations can also contribute to the SPMD at large momentum.

Fig. 5.2 shows that the shape of the SPMD changes with the correlation strength in a nontrivial way. In Fig. 5.5 I present the renormalization factor

$$R_C(p_m) = \frac{N(C_0 = 1; p_m)}{N(C_0 = 0; p_m)}, \tag{5.19}$$

which expands the difference between the mean field and correlated distributions to greater detail. At large p_m this ratio blows up, but at intermediate $p_m \lesssim k_F$ it has a nontrivial behaviour: The short range correlation effects *enhance, rather than suppress*, the SPMD and lead to $R_C(p_m) > 1$ at small p_m, the extra strength at large p_m due to short range correlations comes from a depletion of the SPMD at $p_m \sim k_F$, rather than from the region of $p_m \sim 0$.

There are no direct experimental data on the SPMD in ^4He with which one could compare the results. The model SPMD $N(\vec{p}_m)$ is close to the results from the recent Monte Carlo calculation [23] and the y-scaling analysis [66].

5.3 Final state interaction effects

Choosing the nucleon "4" as the struck proton, the FSI operator takes the form

$$\hat{S}(\vec{r}_1, ..., \vec{r}_4) = \prod_{i=1}^{3} \left[1 - \theta(z_i - z_4)\Gamma(\vec{b}_4 - \vec{b}_i)\right], \tag{5.20}$$

with the familiar profile function $\Gamma(\vec{b})$ of the nucleon-nucleon scattering. As the struck proton undergoes FSI with both neutrons and the proton, the corresponding experimental values have to be taken into account: the weighted average of ρ, the ratio of the real to imaginary part of the forward elastic scattering amplitude, takes the value $\rho = -0.33$, the total proton-nucleon cross section is given by $\sigma_{tot} \approx 43\,mb$. The value of the diffraction slope is the same for protons and neutrons, so $b_o = 0.5\,fm$ [40, 54, 55, 53, 49]. The cited values apply to $T_{kin} \approx 1GeV$, but they vary only slightly for higher energies.

Combining the final state interaction operators and the Jastrow correlation factors, one can write down the FSI-modified density matrix as

$$\rho(\vec{R}_3, \vec{R}_3{}') = \int d\vec{R}_1\, d\vec{R}_2 \Psi_o^*(\vec{R}_1, \vec{R}_2, \vec{R}_3{}')$$
$$\times \hat{F}^\dagger(\vec{r}_1{}'.., \vec{r}_4{}')\hat{S}^\dagger(\vec{r}_1{}'.., \vec{r}_4{}')\hat{S}(\vec{r}_1, ..., \vec{r}_4)\hat{F}(\vec{r}_1, ..., \vec{r}_4)\Psi_o(\vec{R}_1, \vec{R}_2, \vec{R}_3)\,. \tag{5.21}$$

The operator $\hat{F}^\dagger\hat{S}^\dagger\hat{S}\hat{F}$ which emerges in (5.21) can be expanded as

$$\begin{aligned}\hat{F}^\dagger\hat{S}^\dagger\hat{S}\hat{F} &= \prod_{i<j}^{4}\left[1 - C^\dagger(\vec{r}_i{}' - \vec{r}_j{}')\right]\left[1 - C(\vec{r}_i - \vec{r}_j)\right] \\ &\times \prod_{i\neq 4}\left[1 - \theta(z_i' - z_4')\Gamma^\dagger(\vec{b}_4{}' - \vec{b}_i{}')\right]\left[1 - \theta(z_i - z_4)\Gamma(\vec{b}_4 - \vec{b}_i)\right] = \\ 1 - \sum_{i<j}\left[C^\dagger + C\right] &- \sum_{i\neq 4}\left[\Gamma^\dagger + \Gamma\right] + \sum[C^\dagger\Gamma + C\Gamma^\dagger] + \sum C^\dagger C + \sum \Gamma^\dagger\Gamma + ...\end{aligned} \tag{5.22}$$

The rôle of the FSI terms in the cluster expansion (5.22) is very similar to that of the short-range correlation terms. There are interactions which only involve one of the trajectories in the FSI-modified OBDM, there are terms of the form $\theta(z_i' - z_4')\theta(z_i - z_4)\Gamma^\dagger(\vec{b}_4' - \vec{b}_i')\Gamma(\vec{b}_4 - \vec{b}_i)$, which lead to an interaction between the two trajectories etc. There also emerges a novel kind of an interaction between the two trajectories of the form $C^\dagger(\vec{b}_4' - \vec{b}_i)\Gamma(\vec{b}_4 - \vec{b}_i)$ (plus its hermitian conjugate and higher order short ranged interactions), which is due to the quantum-mechanical interference between the initial state correlations and final state interactions [15].

Before I discuss the numerical results for the FSI effects in the full expansion (5.22), I classify the most important FSI terms and FSI-correlation interference terms. This classification is possible due to the fact that in the considered region of high energies of the struck proton, the correlation radius r_c and the diffraction slope b_o are approximately equal: $r_c \approx b_o$, and both are much smaller than the nuclear radius R_o. Due to the presence of the theta-function in the FSI operator, it is not possible to calculate the contributions of the FSI terms analytically as it was done in the previous section for the correlation terms. However, as the dependence of the FSI operator on the transverse separation $\vec{b}_4 - \vec{b}_i$ is similar to the dependence on $\vec{r}$ of the correlations, the $\vec{p}_\perp$ dependence ($\vec{p}_m = (\vec{p}_\perp, p_{m,z})$) of the FSI terms is

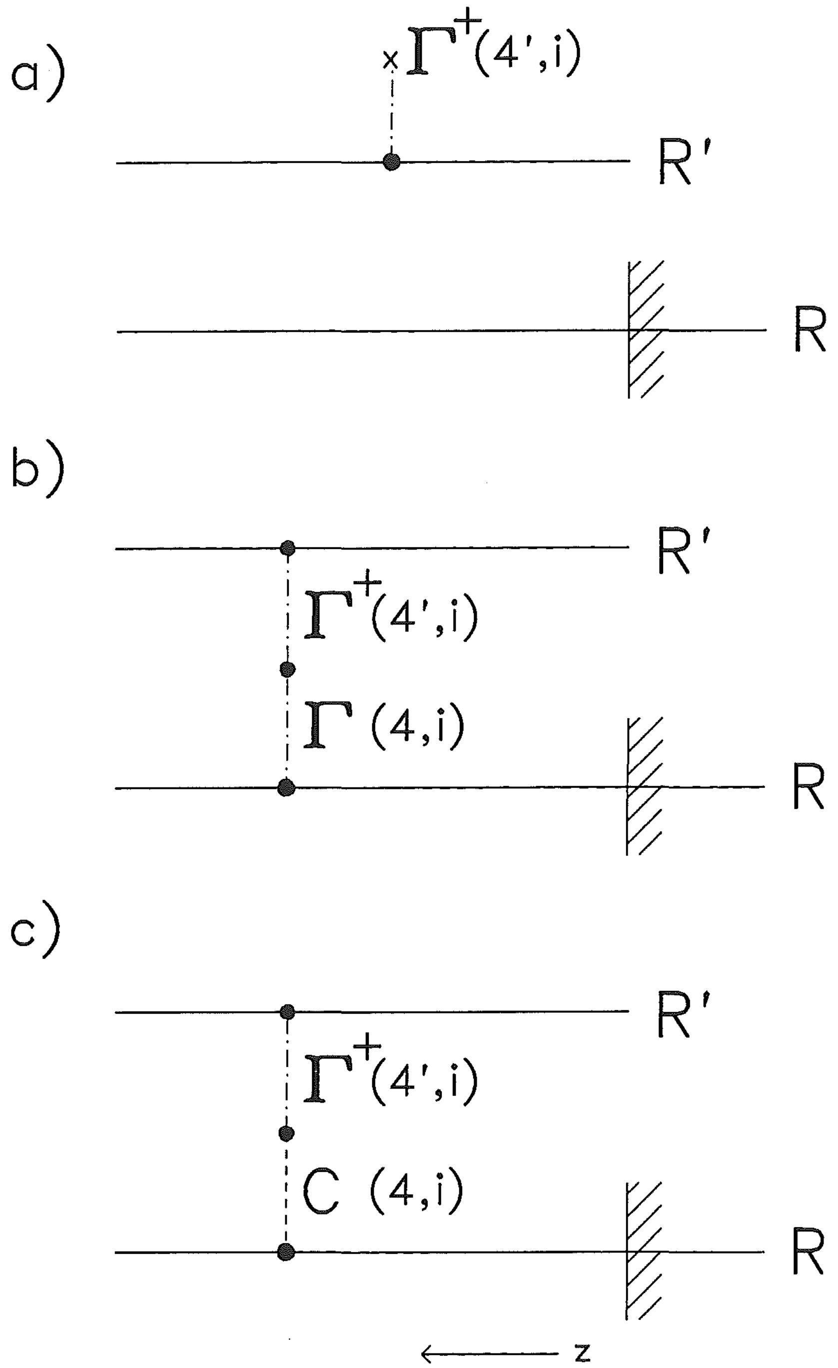

Figure 5.6: Schematic diagrams of several contributions to the one-body density matrix modified by final state interactions and correlations. Panel a) shows a linear final state interaction term of the type $\Gamma^{\dagger}(\vec{r}_i{}' - \vec{r}_4{}')$, panel b) shows the most important quadratic contribution $\Gamma^{\dagger}(\vec{r}_i{}' - \vec{r}_4{}')\,\Gamma(\vec{r}_i - \vec{r}_4)$ and panel c) shows a second order FSI-ISC interference contribution of the type $\Gamma^{\dagger}(\vec{r}_4{}' - \vec{r}_i{}')\,C(\vec{r}_i - \vec{r}_4)$.

similar to that of the correlation terms, one just has to interchange r_c and b_o and the different normalizations. The $p_{m,z}$ dependence of the FSI terms is governed by the long-ranged theta-functions. The integration over the theta-function does not lead to a factor $\frac{b_o}{R_o}$, therefore it increases the normalization of the FSI terms as compared with the correlation terms considerably.

Now, the various final state interaction terms are classified and investigated in detail: The terms linear in $\Gamma^\dagger$ and Γ correspond to an interaction with one of the two trajectories in the OBDM as shown in Fig. 5.6a. As such, they lead to a long ranged contribution to the OBDM and to a contribution $W(\Gamma^\dagger+\Gamma;\vec{p}_m)$ to the FSI-modified missing momentum distribution of the form very similar to $N(C^\dagger+C;\vec{p}_m)$ of Eq. (5.12), but with the normalization typical of the Glauber multiple scattering theory [19, 90]

$$Y \approx \frac{\sigma_{tot}}{4\pi b_0^2}\cdot\left(\frac{b_0}{R_0}\right)^2 = \frac{\sigma_{tot}}{4\pi R_0^2} \approx 0.2\,, \tag{5.23}$$

which is larger than the normalization in (5.14) by a factor of the form

$$\frac{W(\Gamma^\dagger+\Gamma;\vec{p}_m)}{N(C^\dagger+C;\vec{p}_m)} \approx \left(\frac{\sigma_{tot}}{4\pi b_0^2}\right)\cdot\left(\frac{b_0}{R_0}\right)^2\cdot\left(\frac{R_0}{r_c}\right)^3\cdot\frac{1}{C_0} \approx \frac{R_0}{r_c}\cdot\frac{1}{C_0} \approx 2.6 \gg 1\,. \tag{5.24}$$

Here I have used that $b_0 \approx r_c$ and $\sigma_{tot} \approx 4\pi b_0^2$ (actually, $\frac{\sigma_{tot}}{4\pi b_0^2} \approx 1.4$, which even leads to a still larger normalization of the FSI terms). The enhancement factor $\sim R_0/r_c$ in (5.24) derives from the fact that the Glauber operator is a long ranged function of the longitudinal separation in contrast to the short ranged correlation function and is the simplest demonstration that FSI effects in the missing momentum distribution are more important than the correlation effects. Eq. (5.24) gives an estimate of the relative normalizations of the two components of the missing momentum distribution. The transverse momentum dependence of both components is essentially identical. For the presence of the θ-function in the Glauber operator, the $p_{m,z}$ dependence of $W(\Gamma;\vec{p}_m)$ can not be written down in a simple analytical form (one can derive an involved and not very enlightening expression in terms of an error function of a complex argument); what is important is that it is a steeply decreasing function of $p_{m,z}$ on the scale k_F.

An analysis of higher order effects proceeds very similarly. The driving short ranged FSI contribution to the OBDM and to the large-p_m tail of the missing momentum distribution $W(\vec{p}_m)$ comes from diagrams of the type shown in Fig. 5.6b which correspond to terms $\propto \Gamma^\dagger(\vec{b}_4' - \vec{b}_i')\Gamma(\vec{b}_4 - \vec{b}_i)$ in the expansion (5.22). Suppressing for a while the $p_{m,z}$ dependence and making use of the strong inequality

$(b_0/R_0)^2 \ll 1$, in close similarity to $N(C^\dagger C;\vec{p}_m)$ we find

$$W(\Gamma^\dagger\Gamma;\vec{p}_m) \propto \left|\int d^2\vec{B}\Gamma(\vec{B})\exp(i\vec{p}_\perp\vec{B})\right|^2$$
$$= 4\pi\frac{d\sigma_{el}}{dp_\perp^2} = \frac{1}{4}\sigma_{tot}^2(1+\rho^2)\exp(-b_o^2p_\perp^2)\,. \qquad (5.25)$$

The result that this particular contribution to the transverse missing momentum distribution is proportional to the differential cross section of elastic pN scattering, $d\sigma_{el}/dp_\perp^2$, is self-explanatory and the effect of $\Gamma^\dagger\Gamma$ interaction admits a quasiclassical interpretation as an incoherent elastic rescattering of the struck proton on spectator nucleons.

Because of $b_o \approx r_c$ in the CEBAF range of energy, the short ranged $C^\dagger C$ and $\Gamma^\dagger\Gamma$ interactions between the two trajectories in $\rho(\vec{R},\vec{R}')$ lead to $W(C^\dagger C;\vec{p}_m) = N(C^\dagger C;\vec{p}_m)$ and $W(\Gamma^\dagger\Gamma;\vec{p}_m)$ components with very similar $p_\perp$ dependence. In close similarity to Eq. (5.24), the overall normalization is substantially larger for the FSI term. A comparison of the two components at $p_{m,z}=0$ gives

$$\frac{W(\Gamma^\dagger\Gamma;\vec{p}_m)}{W(C^\dagger C;\vec{p}_m)} \approx \frac{1}{C_o^2\sqrt{6}}\cdot\left[\frac{\sigma_{tot}}{4\pi r_c^2}\right]^2\cdot\left(\frac{R_o}{r_c}\right)^2 \approx 5 \qquad (5.26)$$

and leads to the important conclusion that the tail of the transverse missing momentum distribution must be entirely dominated by FSI effects.

As the FSI is long-ranged in $z_4 - z_i$, $W(\Gamma^\dagger\Gamma;\vec{p}_m)$ decreases steeply with $p_{m,z}$ on the scale $\sim k_F \sim 1/R_0$. This leads to a strong angular anisotropy of the elastic rescattering effect, compare with Eq. (5.25). However, the naively expected continuation of this steep decrease of the $\Gamma^\dagger\Gamma$ contribution and the dominance of the $C^\dagger C$ correlation component (5.16) of the SPMD in (anti)parallel kinematics at large $|p_{m,z}| \gtrsim k_F$ are not borne out by the numerical results. The $p_{m,z}$ dependence of $W(\Gamma^\dagger\Gamma;\vec{p}_m)$ has peculiarities of its own. The θ-function, which is present in the Glauber operator, has a slowly decreasing Fourier transform at large $p_{m,z}$. The contribution from the $\Gamma^\dagger\Gamma$ interaction to the integrand of the OBDM contains the product of the θ-functions of the form $\theta(z_i'-z_4')\theta(z_i-z_4) = \theta(z_i - z_{max})$, where

$$z_{max} = \frac{1}{2}(z_4+z_4') + \frac{1}{2}|z_4-z_4'|. \qquad (5.27)$$

The nonanalytic function $|z_4 - z_4'|$ in z_{max} gives rise to a $p_{m,z}^{-2}$ tail of the longitudinal missing momentum distribution after the calculation of the Fourier transform in z_4-z_4' (for a detailed discussion of the case of heavy nuclei see [91]). The factor $\theta(z_i'-$

$z_4')\theta(z_i - z_4)$ implies that the $\Gamma^\dagger\Gamma$ interaction is forbidden on the part of either one or the other of the trajectories in the calculation of the OBDM as shown schematically in Fig. 5.6. This ban on the $\Gamma^\dagger\Gamma$ interaction is of purely quantum-mechanical origin and the $\propto p_{m,z}^{-2}$ tail of the longitudinal missing momentum distribution defies any classical interpretation, in contrast to the strong FSI enhancement of the transverse missing momentum distribution, which admits a semiclassical interpretation to a certain extent. For the reasons explained in detail in [91], the $\Gamma^\dagger\Gamma$ interaction and the resulting $\propto p_{m,z}^{-2}$ tail of the missing momentum distribution are missed in the conventional DWIA.

Another nontrivial and important effect, the quantum-mechanical interference of correlations and final state interactions, comes from the terms $\propto C^\dagger(\vec{r}_4\,' - \vec{r}_i\,')\Gamma(\vec{b}_4 - \vec{b}_i)$ and $\propto C(\vec{r}_4 - \vec{r}_i)\Gamma^\dagger(\vec{b}_4\,' - \vec{b}_i\,')$. These and higher order cyclic and non-cyclic terms lead to a short range interaction as shown in Fig 5.6c in the transverse separation between the trajectories in the calculation of the OBDM (5.20) and to a large-p_m tail of the transverse missing momentum distribution of the form

$$w(C\Gamma^\dagger + C^\dagger\Gamma; \vec{p}_m) \propto \int d^2\vec{R}C^\dagger(\vec{R})\exp(i\vec{p}_\perp\vec{R}) \cdot \mathrm{Re}\int d^2\vec{B}\Gamma(\vec{B})\exp(-i\vec{p}_\perp\vec{B})$$
$$\propto \exp\left[-\frac{1}{2}(r_c^2 + b_o^2)p_\perp^2\right]\,. \quad (5.28)$$

Considering that $b_0 \sim r_c$, at large $p_\perp$ the effects of the $C\Gamma^\dagger + C^\dagger\Gamma$ interaction are as important as those of the $C^\dagger C$ and $\Gamma^\dagger\Gamma$ interactions. Furthermore, the remarkable feature of the FSI-correlation interference term is that owing partly to numerical factors, it has a large normalization. At $p_{m,z} = 0$ we find

$$\frac{W(C\Gamma^\dagger + C^\dagger\Gamma; \vec{p}_m)}{W(\Gamma^\dagger\Gamma; \vec{p}_m)} \approx 4\sqrt{\frac{3}{5}}C_o\left(\frac{4\pi r_c^2}{\sigma_{tot}}\right) \cdot \frac{r_c}{R_o} \approx 0.9\,. \quad (5.29)$$

This clearly shows that the interference between final state interactions and correlations is much more important than the pure correlation component of the missing momentum distribution. Notice that any semiclassical consideration would completely miss this large correlation-FSI interference effect. Furthermore, the numerical significance of this interference effects shows that even in perpendicular kinematics, the semiclassical treatment of FSI misses important quantum mechanical effects and must be taken with great caution. The $p_{m,z}$ dependence of this contribution to $W(\vec{p})$ is controlled by the long range character in the longitudinal separation of the Glauber operator.

The terms of higher order than the already discussed quadratic terms have a still smaller normalization. Some of them also contribute to the missing momentum distribution at higher missing momenta, and their small normalization is compensated by the larger number of higher order terms (the convergence behaviour is discussed below). The most important types of higher order terms are briefly discussed here. The leading short-range correlation correction to the elastic rescattering effect comes from the terms $\propto C(\vec{r}_4 - \vec{r}_i)\Gamma(\vec{b}_4 - \vec{b}_i)\Gamma^*(\vec{b}_4{}' - \vec{b}_i{}')$, which have the $p_\perp$ dependence with the slope

$$\frac{1}{2}\left(b_o^2 + \frac{b_o^2 r_c^2}{b_o^2 + r_c^2}\right) < b_o^2\,, \tag{5.30}$$

a steep $p_{m,z}$-dependence and the normalization

$$\frac{W(C\Gamma'\Gamma + C'\Gamma'\Gamma)}{W(\Gamma'\Gamma)} = -2C_o\sqrt{\frac{3}{5}} \cdot \frac{r_c^2}{b_o^2 + r_c^2} \cdot \frac{r_c}{R_o} \sim -0.3. \tag{5.31}$$

These corrections are not small. In a different form, a similar result is contained in Eq. (7) of Ref.[92]. The FSI correction to the correlation effect comes from terms $\propto C(\vec{r}_4{}' - \vec{r}_i{}')C(\vec{r}_4 - \vec{r}_i)\Gamma(\vec{b}_4 - \vec{b}_i)$, which give

$$W(C'C\Gamma + C'C\Gamma'; \vec{p}_m) \propto \exp(-r_c^2 p_{m,z}^2)\exp\left[-\frac{1}{2}\left(\frac{b_o^2 r_c^2}{b_o^2 + r_c^2} + r_c^2\right)p_\perp^2\right], \tag{5.32}$$

slow decrease with p_z and the relative normalization

$$\frac{W(C'C\Gamma + C'C\Gamma')}{W(C'C)} \approx -\frac{r_c^2}{r_c^2 + b_o^2} \cdot \frac{\sigma_{tot}}{4\pi r_c^2} \sim -\frac{2}{3}\,. \tag{5.33}$$

The still higher order terms of the form $\propto \Gamma^\dagger(\vec{b}_4' - \vec{b}_i')\Gamma(\vec{b}_4 - \vec{b}_i)\Gamma^\dagger(\vec{b}_4' - \vec{b}_k')\Gamma(\vec{b}_4 - \vec{b}_k)$ lead to a second order short ranged interaction between the trajectories in the FSI-modified OBDM. The transverse momentum dependence of such a contribution to $W(\vec{p}_m)$ also admits a semiclassical form of the convolution of differential cross sections of consecutive incoherent elastic scatterings and

$$W(\Gamma^\dagger\Gamma\Gamma^\dagger\Gamma; \vec{p}_m) \propto Y^4 \exp(-\frac{1}{2}b_o^2 p_\perp^2)\,. \tag{5.34}$$

The $\propto (b_0/R_0)^2$ corrections to the slopes in (5.25) can readily be derived and correspond very qualitatively to a slight smearing of the elastic scattering cross section due to the -compared to the momentum transfer in elastic pN scattering- small initial Fermi motion of the struck proton and the spectator nucleon (for a critical discussion of semiclassical considerations see [91]).

5.4 Final State Interaction and Missing Momentum Distribution: the Numerical Results

The full calculation of the FSI-modified OBDM is quite involved, because the full expansion (5.21),(5.22) for the integrand of the OBDM contains 2^{18} terms. The θ-function in the Glauber operator leads to the slow convergence of the Fourier transform and requires very tight control of numerical accuracy in the calculation of the FSI-modified missing momentum distribution, especially at large $|p_{m,z}|$. With the generic wave function, an accurate calculation of the large-p_m behaviour of $W(\vec{p}_m)$ would have required enormous computing time. The chosen Ansatz wave function, complemented by the usual Gaussian form of the profile function, simplifies the task greatly, because all the transverse coordinate integrations and the corresponding Fourier transform in the transverse missing momentum can be performed analytically to all orders in correlations and final state interactions. Only the longitudinal coordinate integrations and the corresponding Fourier transform must be performed numerically. Now I present some of the results for the missing momentum distribution $W(\vec{p}_m)$. Unless specified otherwise, all the numerical results are for the hard core correlation, $C_0 = 1$.

As the PWIA missing momentum distribution including the correlation functions is completely isotropic, any anisotropy in $W(\vec{p}_m)$ is a clear signal of FSI. In Fig. 5.7, I show the angular distribution of $W(\vec{p}_m)$ for different missing momenta for the full calculation with FSI (solid line) and the PWIA result (dashed line). Already at the rather low missing momentum of $p_m = 1.0 fm^{-1}$, there is a strong deviation from the isotropic PWIA behaviour. With growing missing momentum, the dip around 90^o evolves through a very asymmetric stage into a pronounced peak at $p_m \gtrsim 1.6\, fm^{-1}$, the signal of complete FSI (plus correlation-FSI interference) dominance. The evolution of the angular distribution is especially fast around $p_m \sim 1.5\, fm^{-1}$. As for the case of the deuteron targets, the forward-backward asymmetry $W(p_\perp, p_z) \neq W(p_\perp, -p_z)$ is present in the angular distributions. This forward-backward asymmetry has its origin in the nonvanishing real parts of the $p-n$ and $p-p$ scattering amplitudes $\rho \neq 0$, leading to $\hat{S}^\dagger(\vec{b}'_1, z'_1, \ldots \vec{b}'_4, z'_4)\hat{S}(\vec{b}_1, z_1, \ldots \vec{b}_4, z_4) \neq \hat{S}^\dagger(\vec{b}_1, z_1, \ldots \vec{b}_4, z_4)\hat{S}(\vec{b}'_1, z'_1, \ldots \vec{b}'_4, z'_4)$ in the integrand of (5.5).

The same features of $W(\vec{p}_m)$ can be seen in the missing momentum distributions

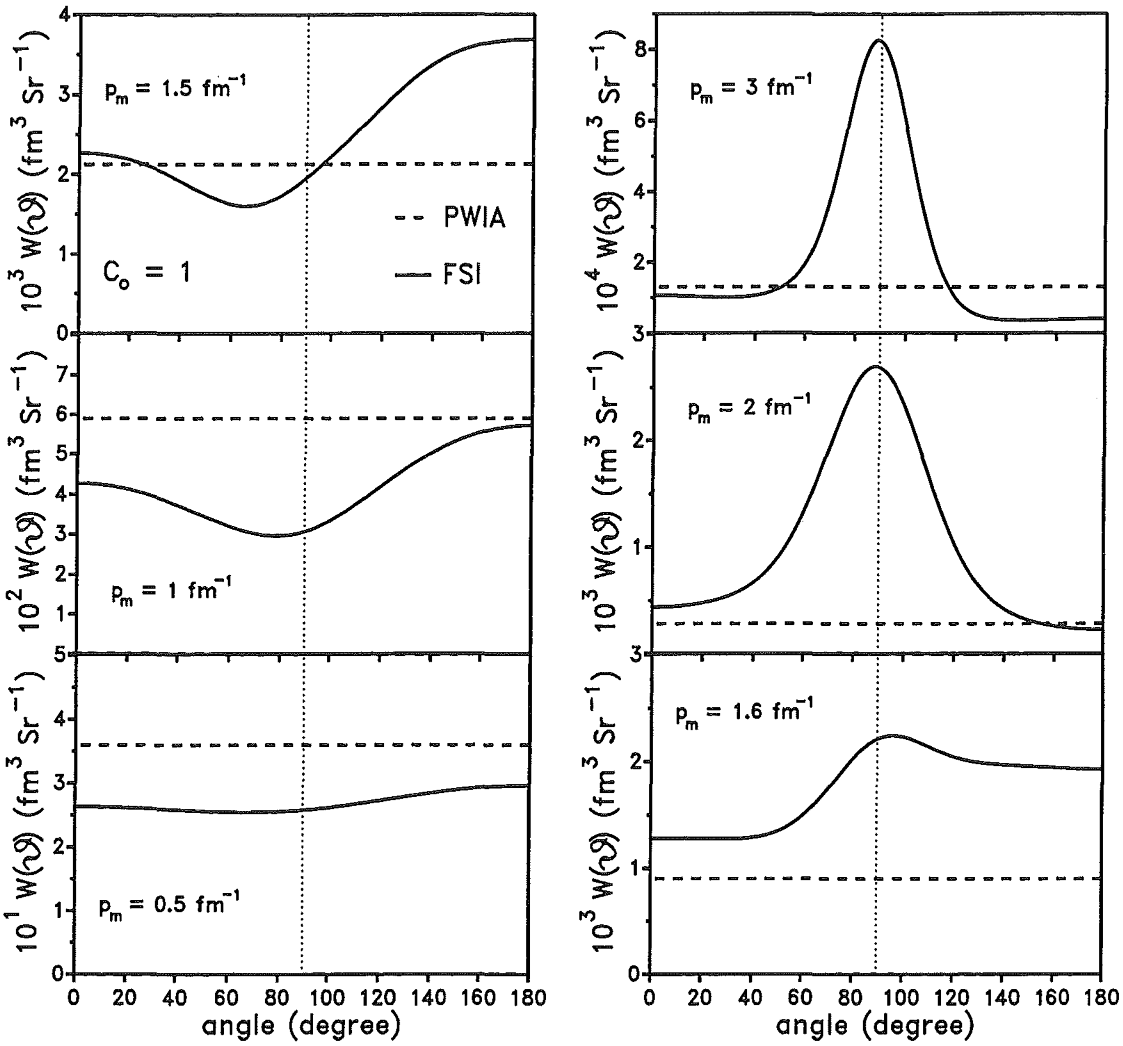

Figure 5.7: The angular dependence of the missing momentum distribution $W(\vec{p}_m)$ for different missing momenta p_m (full line). For comparison, the corresponding value of the single particle momentum distribution $N(p_m)$ is also plotted (dotted line).

displayed for (anti)parallel and perpendicular kinematics in Fig. 5.8. For small missing momentum, the FSI leads to a reduction of strength. At $p_m = 0$ the PWIA distribution is depleted by approximately 24%, which is about twice as large as the nuclear shadowing effect in the total $p\,{}^4He$ cross section [90]. Two mechanisms contribute to this depletion which is mostly due to the $\Gamma^\dagger + \Gamma$ terms in the expansion (5.22): i) attenuation of the flux of struck protons due to absorption by inelastic interaction with the spectator nucleons, ii) deflection of the struck protons by elastic

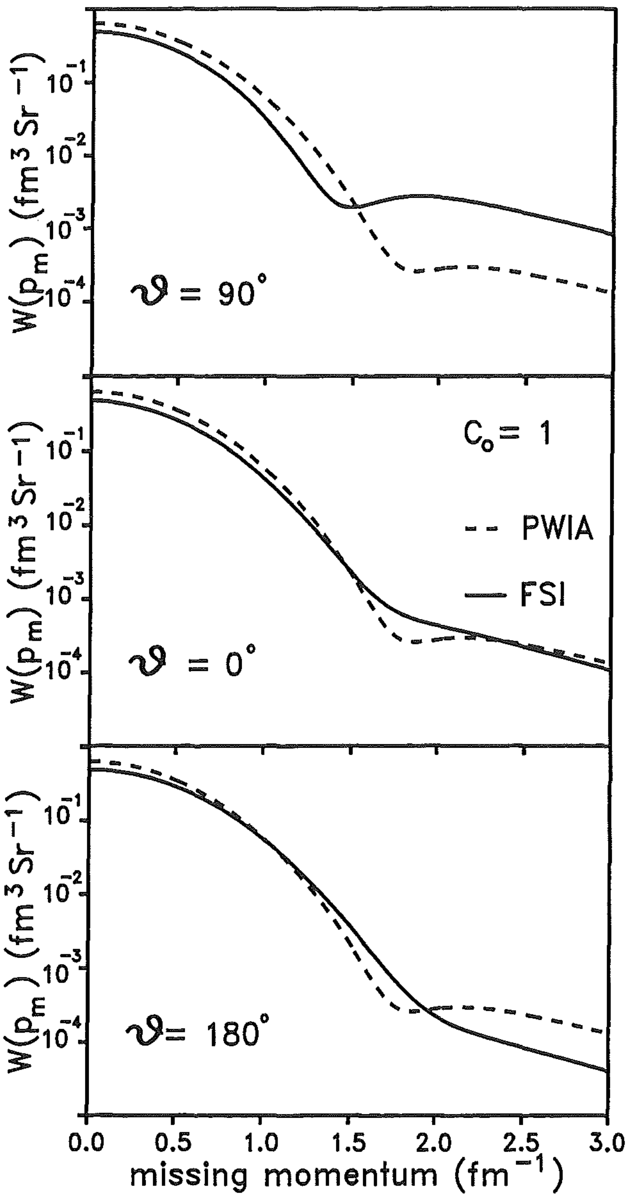

Figure 5.8: The missing momentum distribution $W(\vec{p}_m)$ (full line) and the single particle momentum distribution $N(p_m)$ (dashed line) for $\theta = 90^o$ (upper panel), $\theta = 0^o$ (middle panel), and for $\theta = 180^o$ (lower panel). The parameters for the nuclear ground state are $R_o = 1.29fm$, $r_c = 0.5fm$ and $C_o = 1$.

scattering on the spectator nucleons. Such a semiclassical interpretation must be taken with the grain of salt, though: because of the quantum-mechanical interference effects, FSI leads to quite a complicated, strongly $\vec{p}_m$ dependent, pattern of depletion and/or enhancement of the FSI modified missing momentum distribution $W(\vec{p}_m)$ as compared to the PWIA distribution $N(\vec{p}_m)$. With increasing missing momentum, up to $p_m < 0.5 fm^{-1}$, the angular distribution is almost isotropic, from $p_m = 0.5 fm^{-1}$ on, the deviations from the isotropic PWIA behaviour grow larger. In perpendicular kinematics, from $p_m = 1.5 fm^{-1}$ on, the full calculation including FSI (solid line) shows a large tail at high missing momenta, which is one order of magnitude larger than the tail of the PWIA distribution $N(p_m)$ for hard core correlations (dotted line).

The peculiarities of the Fourier transform of the θ-function factors do not show up in perpendicular kinematics, at $p_{m,z} = 0$. Here the rôle of the Glauber operator $\Gamma(\vec{b})$ in the evaluation of the FSI-modified OBDM is nearly identical to the rôle of the correlation function $C(\vec{r})$ in the modification of the mean-field OBDM. The only difference is in a much larger strength of FSI effects, which is the reason why $W(\vec{p}_m)$ develops a minimum at $p_m \approx 1.4\, fm^{-1}$ as compared to the minimum of the PWIA distribution at $p_m \approx 1.7\, fm^{-1}$.

To this end, notice that $p_m \approx 1.4\, fm^{-1}$ corresponds to a region of p_m in which the effect of short range correlations in the SPMD is still marginal. Already this observation suggests very strongly that in perpendicular kinematics, $\theta = 90°$, the missing momentum distribution $W(\vec{p}_m)$ can only weakly depend on the short-range correlation effects in the nuclear wave function. This is indeed the case. The results shown in Fig. 5.9 demonstrate that, in striking contrast to the strongly correlation dependent PWIA distribution $N(\vec{p}_m)$ of Fig. 5.2, the FSI-modified $W(\vec{p}_m)$ is extremely insensitive to the strength of the short range correlations. Namely, even at large $p_m \gtrsim 1.5 fm^{-1}$ the missing momentum distribution $W(\vec{p}_m)$ calculated with $C_o = 1$ is only by $\sim$ 50% larger than $W(\vec{p}_m)$ calculated with $C_o = 0$, in contrast to a difference of several orders in magnitude in the PWIA distributions for $C_o = 0$ and $C_o = 1$. This enhancement is much stronger than expected from the pure correlation contribution of PWIA, though. In a classical consideration, such an enhancement of $W(\vec{p}_m)$ with the correlation strength is quite counterintuitive: the classical probability of elastic rescattering of the struck proton on the spectator nucleon is higher for close configurations, which are suppressed by the hard core correlation. The found enhancement of $W(\vec{p}_m)$ from the mean field, $C_0 = 0$, to the hard core correlation, $C_0 = 1$, wave function must be attributed to the above discussed correlation-FSI interference effect, see Eq. (5.27), which is numerically larger than the effect of the suppression of the $\Gamma^\dagger\Gamma$ elastic rescattering contribution by the short range correlation (see the discussion above). Fig. 5.10 shows that the situation

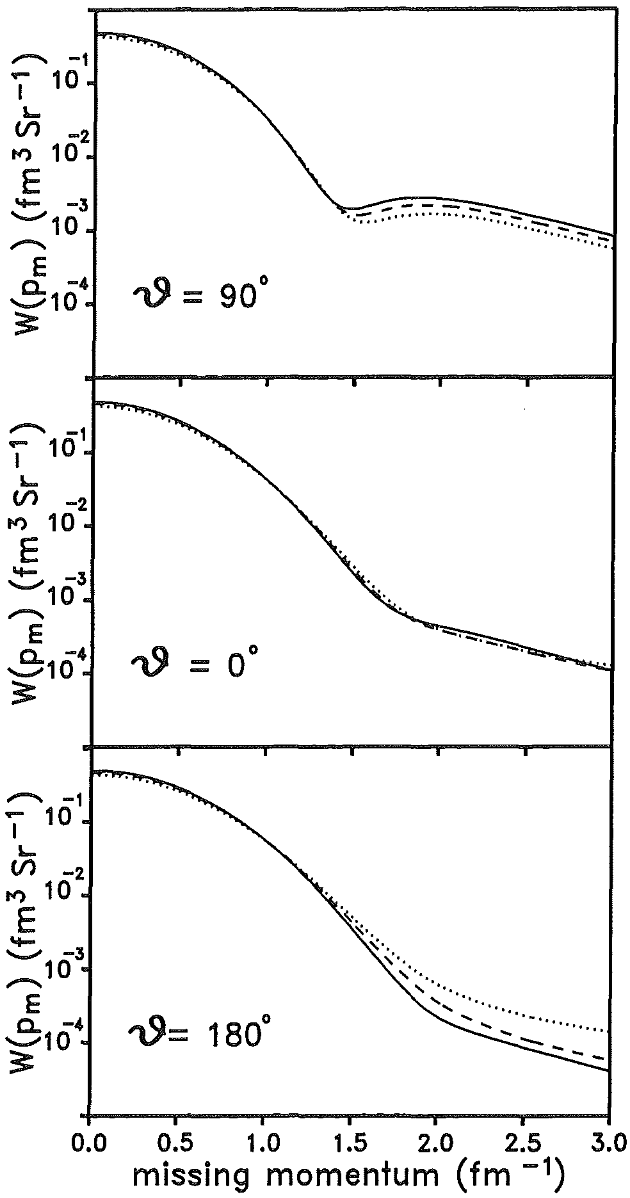

Figure 5.9: In each panel the missing momentum distribution $W(\vec{p}_m)$ is plotted for hard core correlations, $C_o = 1$, (solid line), soft core correlations, $C_o = 0.5$, (dashed line) and no correlations at all, $C_o = 0$ (dotted line). The upper panel shows the results for $\theta = 90^o$, $\theta = 0^o$ is shown in the middle panel and $\theta = 180^o$ is shown in the lower panel. The parameters for the nuclear ground state are $R_o = 1.29fm$ and $r_c = 0.5fm$.

changes neither qualitatively nor quantitatively if the correlation radius is increased from $r_c = 0.5\,fm$ to $r_c = 0.6\,fm$. Thus, the conclusion is that FSI is dominating

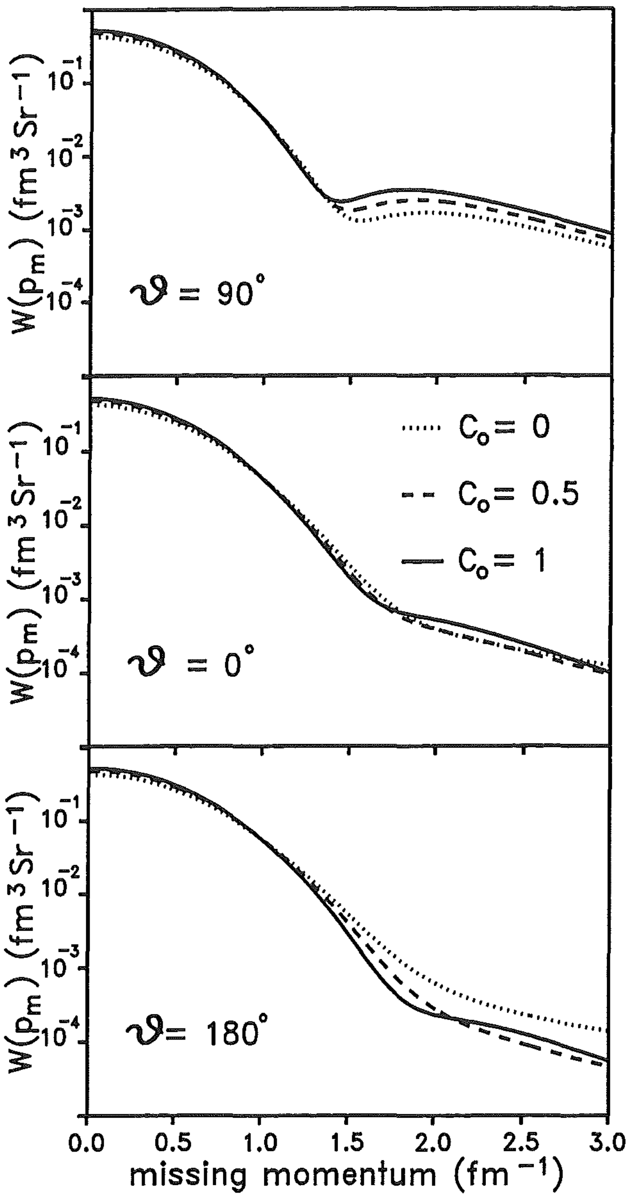

Figure 5.10: The same as in the previous figure, only with the correlation radius $r_c = 0.6fm$ instead of $r_c = 0.5fm$ as above.

completely and that it will be extremely difficult to disentangle the effects of short range correlations in the ground state of the target nucleus from the FSI-affected experimental data on $A(e, e'p)$ scattering in perpendicular kinematics.

Let's have a look at (anti)parallel kinematics, $\theta = 0^o$ and $\theta = 180^o$, to check if the situation there is more promising. In the angular distributions of Fig. 5.7 one can see that also in (anti)parallel kinematics, deviations from the PWIA behaviour are present and large. The missing momentum distributions for (anti)parallel kinematics displayed in Figs. 5.8b,c differ strongly from $W(\vec{p}_m)$ in perpendicular kinematics. In antiparallel kinematics, at $\theta = 180^o$, the nuclear depletion of $W(\vec{p}_m)$ at $p_m = 0$ of approximately 24% vanishes with increasing p_m and is superseded by nuclear enhancement at $p_m \gtrsim 1\,fm^{-1}$. In parallel kinematics, at $\theta = 0^0$, a similar transition from nuclear depletion to nuclear enhancement takes place at $p_m \gtrsim 1.5\,fm^{-1}$. This difference between parallel and antiparallel kinematics is due to the before-mentioned forward-backward asymmetry generated by the nonvanishing value of ρ. The minimum or shoulder-like irregularity that is present in PWIA at $p_m \approx 1.7 fm^{-1}$, and which in perpendicular kinematics is shifted by FSI to $p_m \approx 1.4 fm^{-1}$, is washed out by the FSI both in parallel and antiparallel kinematics. Now, $W(\vec{p}_m)$ is decreasing monotonously.

The results for parallel kinematics, $\theta = 0^o$, show that the PWIA distribution $N(p_m)$ and the FSI-modified distribution $W(\vec{p}_m)$ are very close to each other for missing momenta $p_m > 2 fm^{-1}$, although $W(\vec{p}_m)$ slightly undershoots the PWIA values. Must this be taken as evidence that FSI is unimportant in parallel kinematics, at $\theta = 0^o$? The results shown in Figs. 5.9b,c demonstrate that this is not the case. In parallel kinematics, Fig. 5.9b, $W(\vec{p}_m)$ hardly changes from the mean field, $C_0 = 0$, (dotted line) to the soft core correlation, $C_o = 0.5$, (dashed line) to the hard core correlation, $C_0 = 1$, (solid line), which must be contrasted to a dramatic sensitivity of the SPMD to the correlation strength C_0 in the same region of large p_m. In antiparallel kinematics, for $\theta = 180^o$, the FSI-modified distribution $W(\vec{p}_m)$ of Fig. 5.9 exhibits a stronger sensitivity to short range correlations. However, this dependence on the correlation strength C_0 is quite counterintuitive, as $W(p_m)$ decreases substantially when short range correlations are switched on, remaining lower than both the PWIA distribution $N(p_m)$ and the FSI-modified distribution $W(\vec{p}_m)$ evaluated in the mean field approximation $C_0 = 0$. Notice also that the difference between the cases of the soft core and hard core correlations in Fig 5.9 is much smaller than the difference between the PWIA distribution $N(\vec{p}_m)$ and the FSI-modified distribution $W(\vec{p}_m)$ for $C_0 = 1$ in Fig 5.8. The predominance of FSI effects is further emphasized by the close similarity of the curves corresponding to $r_c = 0.5\,fm$ and $r_c = 0.6\,fm$, shown in Fig. 5.9 and Fig. 5.10, respectively.

What actually happens in parallel and anti-parallel kinematics is a manifestation of still another strong correlation-FSI interference effect, which in this case is connected with the real part of the pN elastic scattering amplitude. In Fig. 5.11 we show

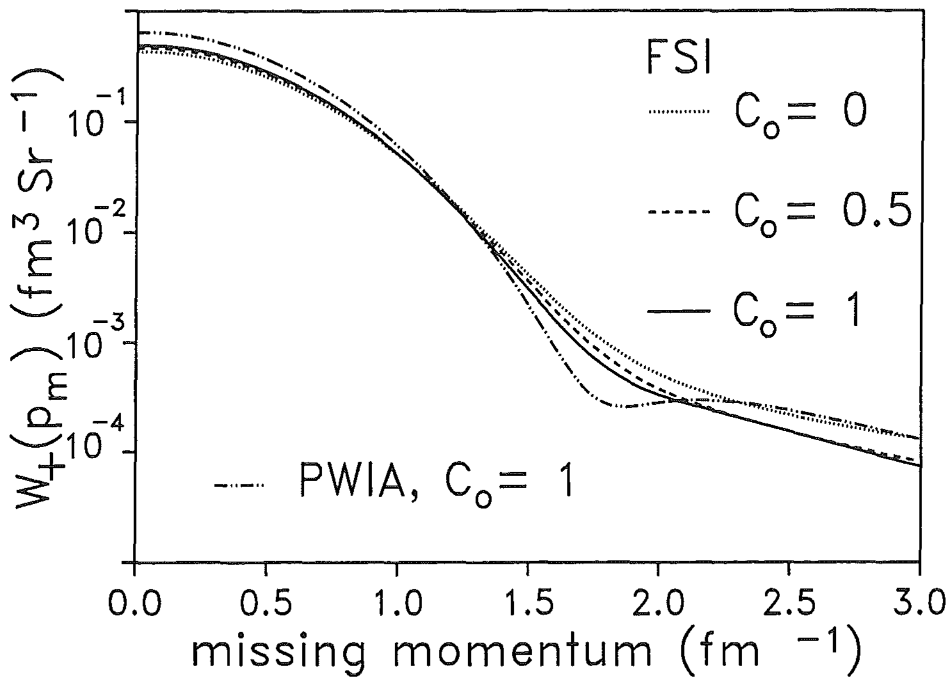

Figure 5.11: The distribution $W_+(p_m) = \frac{1}{2}[W(\theta = 0^o; p_m) + W(\theta = 180^o)]$ is shown for hard core correlations, $C_o = 1$, (solid line), soft core correlations, $C_o = 0.5$, (dashed line), and no correlations at all, $C_o = 0$,(dotted line). The other parameters are $R_o = 1.29 fm$ and $r_c = 0.5 fm$. For comparison, the single particle momentum distribution for hard core correlations, $C_o = 1$, is also shown (dash-dotted line).

separately the large-p_m behaviour of $W_+(p_m) = \frac{1}{2}[W(\theta = 0^o; p_m) + W(\theta = 180^o)]$, which is free of the FSI contribution linear in ρ (the terms $\propto \rho^2$ that are present in W_+ are very small). The influence of ρ on the missing momentum distribution is slightly larger in ^4He than in the deuteron. In the mean field approximation, $C_0 = 0$, the large-p_m tail of $W_+(p_m)$ is entirely due to the θ-function effects. As it was discussed in detail above and in [15, 14, 91], this tail is suppressed by the correlation effects, which naturally smooth out the idealized θ-function in the Glauber operator which assumes idealized pointlike nucleons. On the other hand, the PWIA distribution at $C_0 = 1$ is numerically very close to the FSI effect at $C_0 = 0$. When both the FSI and ISC effects are included, with the increase of C_0 the rising correlation contribution compensates partly for a decrease of the FSI contribution. The net effect is a weak depletion of $W_+(p_m)$ from the mean field, $C_0 = 0$, value to the soft core correlation value at $C_0 = 0.5$. However, there is hardly any change in $W_+(p_m)$ from the soft core to hard core correlation result for $W_+(p_m)$. This is due to a certain numerical conspiracy between the correlation and FSI parameters. From the practical point of view it is important that for a weak energy dependence of the pN scattering parameters, such a conspiracy will persist over the whole range of T_{kin} and Q^2 to be explored at CEBAF.

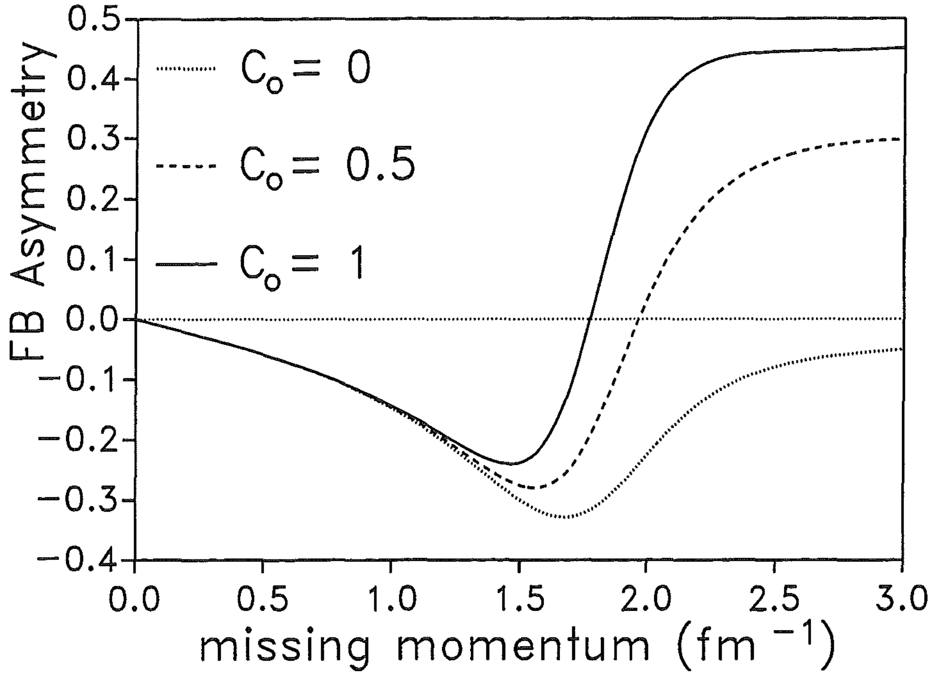

Figure 5.12: The forward-backward asymmetry $A_{FB}(p_m)$ as defined in (5.35) is shown for hard core correlations, $C_o = 1$, (solid line), soft core correlations, $C_o = 0.5$, (dashed line), and no correlations at all, $C_o = 0$, (dotted line). The other ground state parameters are $R_o = 1.29fm$ and $r_c = 0.5fm$.

The substantial rôle of the real part of the pN scattering amplitude in this region of large p_m is obvious from the FSI-induced forward-backward asymmetry

$$A_{FB}(p_m) = \frac{W(\theta = 0^o; p_m) - W(\theta = 180^o; p_m)}{2W_+(p_m)}, \tag{5.35}$$

which is shown in Fig. 5.12. It exhibits a strong dependence on the correlation strength and is quite large for the hard core correlation $C_0 = 1$. The forward-backward asymmetry is an intricate FSI-PWIA interference effect proportional to the real part of the pN scattering amplitude. In the absence of short range correlations, $C_0 = 0$, the asymmetry stays negative valued at all p_m. It changes sign when correlation effects are included. In the latter case one can compare the results for ^4He with the results for the deuteron (see Fig. 3.6), which should resemble each other. Indeed, for the soft and hard core correlations, both the magnitude and p_m dependence of the asymmetry shown in Fig. 5.12 are remarkably similar to the forward backward asymmetry in $D(e, e'p)$ scattering. For the deuteron target, the calculations are performed using the realistic wave functions which directly include the effects of short distance proton-neutron interaction. From this comparison one can conclude that, first, the simple Ansatz wave function for ^4He correctly models gross features of short-distance nucleon-nucleon interaction in ^4He and, second, the found change of the sign of $A_{FB}(p_m)$ and its rise with the correlation strength at large p_m are on firm grounds. It is this enhancement of $A_{FB}(p_m)$ which effectively cancels the effect of slight decrease of $W_+(p_m)$ and produces the correlation independent $W(\theta = 0°; p_m)$. This enhancement of $A_{FB}(p_m)$ also amplifies the slight decrease of $W_+(p_m)$ and produces the counterintuitive substantial decrease of $W(\theta = 180^o, p_m)$ with the correlation strength C_0. The sensitivity of $W(\theta = 0°, 180°; p_m)$ to the correlation strength C_o decreases with the value of ρ. Having established the origin of masking effects of FSI on $W(\vec{p}_m)$ in (anti)parallel kinematics, I wish to point out that even a measurement of $W_+(p_m)$, which is free of the FSI effects proportional to ρ, would not yield much information on the correlations in ^4He, as the sensitivity of this quantity to the value of C_o is not sufficiently strong for a reliable separation of the correlation component of $N(p_m)$.

5.5 On the Convergence of the Power Expansion in SRC and FSI

In section 5.2 I already have commented on the importance of higher order effects in the two-body correlation function $C(\vec{r}_i - \vec{r}_j)$. Roughly, the important terms of each order differ by a factor of $\left(\frac{r_c}{R_o}\right)^3$, i.e. by 0.06 for $r_c = 0.5fm$ and by 0.1 for $r_c = 0.6fm$. Indeed, the rate of convergence for $r_c = 0.6fm$ is distinctly slower than for $r_c = 0.5fm$. However, there are also large combinatorial factors, which make the higher order terms non-negligible. In the PWIA case, the highest existent order is twelve, and the number of terms in the n-th order is $\binom{12}{n}$, so we have 66 second order terms compared to 495 terms of fourth order to 924 terms of sixth order and still 495 terms of eighth order. This is a reason why the contribution of sixth order terms to $N(p_m)$ is still non-negligible. As a general rule, for a specific term to be important at high p_m, it has to connect the two trajectories of the OBDM with correlations, i.e. it has to contain an interaction of the type $C^\dagger(\vec{r}_4 - \vec{r}_i)C(\vec{r}_4{}' - \vec{r}_i{}')$ (plus any number of other correlations between the spectator nucleons and/or the spectator and struck nucleon trajectories) and/or a cyclic chain of correlations , e.g. $C(\vec{r}_4 - \vec{r}_i)C(\vec{r}_i - \vec{r}_j)C(\vec{r}_4{}' - \vec{r}_j{}')$. To the leading order, only three of the possible 66 $C^\dagger C, CC, C^\dagger C^\dagger$ terms contribute at large p_m, and the percentage of important terms per order increases with the order. The above points are illustrated by a comparison of specific higher terms (5.17) and (5.18) with the leading term (5.16). The importance of higher order effects is further enhanced when FSI is included. Here, the expansion (5.22) contains 2^{18} terms.

From the point of view of practical calculations, the major complication with FSI is that the longitudinal coordinate integrations and the corresponding Fourier transforms have to be carried out numerically. At $p_{m,z} = 0$, though, the rôle of the correlation and FSI terms in the expansion (5.22) is very similar, and so are the convergence properties. First I discuss the convergence of the pure FSI terms in the absence of correlations, $C_o = 0$. Fig. 5.13a shows the convergence of $W(\theta = 90^o, p_m)$ for perpendicular kinematics. To higher orders in FSI, one introduces attenuation of the proton wave which leads to a depletion of $W(\theta = 90^o, p_m)$. Although to the fourth-order approximation one finds the positive valued, and slowly decreasing, contribution (5.34) from the double incoherent elastic rescattering, which could have enhanced $W(\theta = 90^o; p_m)$ somewhat, its normalization is too small to have an appreciable impact on the $p_\perp$ distribution in the considered region of p_m. The situation in parallel and anti-parallel kinematics is very similar, see Figs. 5.13b,c. Here the crucial point is that FSI generates the large-p_m tail in $W(\vec{p}_m)$ even in the absence of short range correlations. The convergence is good and the change from the fourth to sixth order is marginal. In the considered case, the precocious convergence in (anti)parallel kinematics is due to an absence of correlations, see below and the discussion in section 5.4.

The convergence of the expansion in the correlation function, which was quite slow already in the PWIA, worsens when final state interactions are included. To have some idea on the interplay of FSI and SRC terms, in Fig. 5.14 I show how $W(\vec{p}_m)$ evolves when the expansion (5.22) is truncated at terms $\sim \Gamma^k C^{N-k}$. The results for $N \geq 6$ include the numerically stronger pure FSI effects to all orders. For perpendicular kinematics, we find a convergence at large p_m only for $N \geq 10$. In parallel and antiparallel kinematics, the contribution from $N = 12$ is still non-negligible. Here a part of the problem is an unexpectedly strong FSI-SRC interference effect

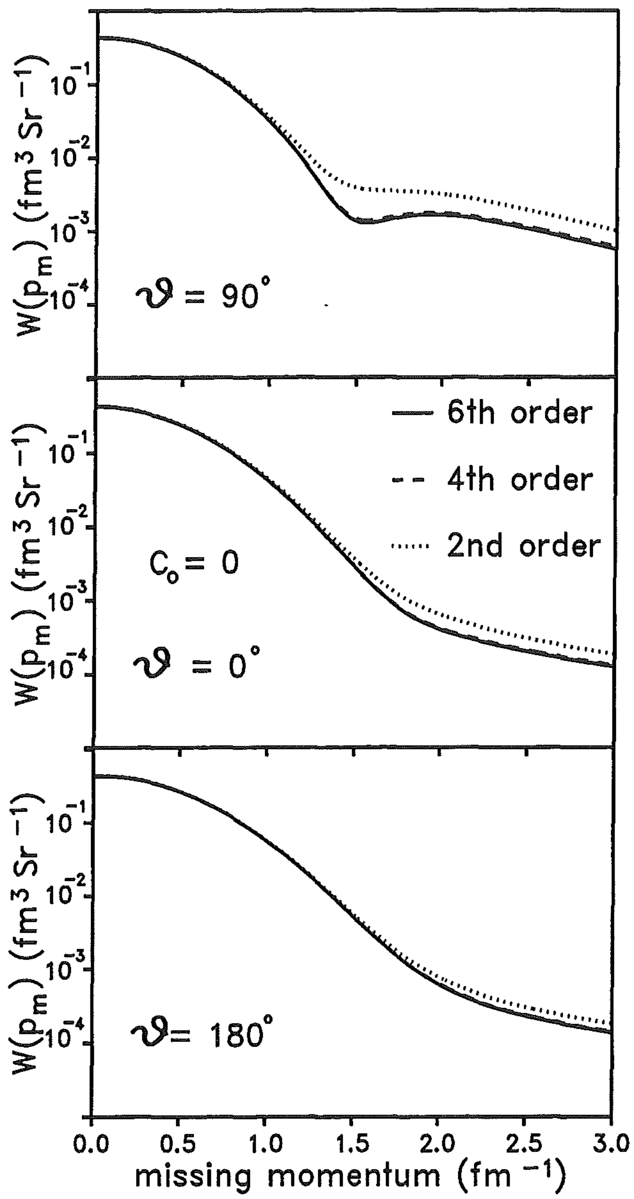

Figure 5.13: The convergence behaviour of the missing momentum distribution $W(\vec{p}_m)$ without any correlations, i.e. $C_o = 0$, for different angles θ. The dotted line shows all the terms up to second order, the dashed line represents all terms up to fourth order, and the full line shows the complete result, i.e. all terms up to sixth order. The upper panel shows the results for $\theta = 90^o$, $\theta = 0^o$ is shown in the middle panel and $\theta = 180^o$ is shown in the lower panel. The other parameters are $R_o = 1.29 fm$ and $r_c = 0.5 fm$.

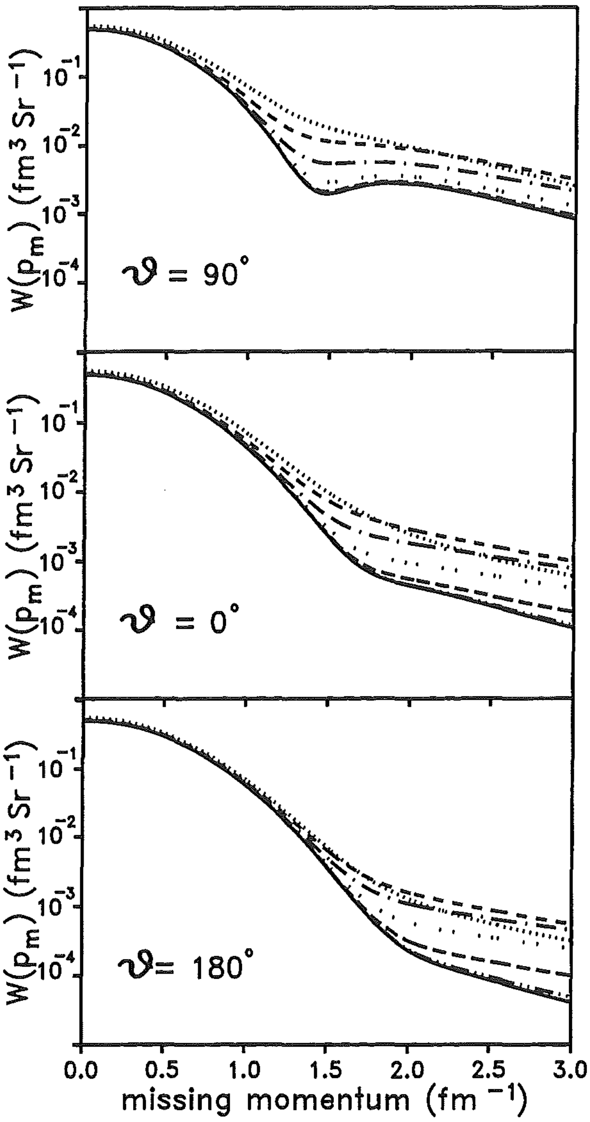

Figure 5.14: The convergence behaviour of the missing momentum distribution $W(\vec{p}_m)$ with hard core correlations, i.e. $C_o = 1$, for different angles θ. The dotted line shows all the terms up to second order, the dashed line represents all terms up to fourth order, the dash-dotted line shows all terms up to sixth order, the double-dotted line includes all terms up to eighth order, the long-dashed line shows the calculation up to the tenth order, the dash-double-dotted line represents all terms up to twelfth order, and the full line shows the complete result, i.e. all terms up to 18th order. The upper panel shows the results for $\theta = 90^o$, $\theta = 0^o$ is shown in the middle panel and $\theta = 180^o$ is shown in the lower panel. The other parameters are $R_o = 1.29 fm$ and $r_c = 0.5 fm$.

associated with the real part of the pN scattering amplitude, which exhibits a strong sensitivity to short range correlations. For the soft core correlation, $C_o = 0.5$, the convergence is much faster. To summarize, these results demonstrate that estimates of the missing momentum distribution to lowest orders in the correlation function, i.e. in the quasi-deuteron approximation, are too crude for making quantitative conclusions. This may partially be due to the form of correlations I employed. However, it indicates that the effects of higher order correlations and multi-particle correlations should be taken into account in a precise calculation of the nuclear ground state.

5.6 Implications for Nuclear Transparency Studies

Nuclear effects in $A(e,e'p)$ scattering are often discussed in terms of the transparency ratio

$$T_A(\vec{p}_m) = \frac{W(\vec{p}_m)}{N(\vec{p}_m)}.$$

The above presented results strongly support the point that the FSI effects do not reduce to an overall renormalization of the observed missing momentum distribution by the nuclear attenuation factor, which is an often uncritically made assumption. Only at $p_m \approx 0$ the found depletion of approximately 24% can be interpreted as a pure nuclear attenuation effect; at larger missing momenta, a strong interplay of attenuation and distortion effects leads to a nuclear transparency $T_A(\vec{p}_m)$ which exhibits both much stronger depletion and "antishadowing" behaviour $T_A(\vec{p}_m) \gg 1$. This is clearly seen in Fig. 5.15, in which I show nuclear transparency for perpendicular, parallel and anti-parallel kinematics for the hard core correlation. In the latter two cases, the nuclear transparency is very strongly affected by the real part of the pN scattering amplitude, the effect of which can not be interpreted in terms of attenuation altogether.

In the experimental determination of nuclear transparency one inevitably runs into a sort of vicious circle: What is measured experimentally is the FSI-distorted missing momentum distribution $W(\vec{p}_m)$ and one is forced to rely upon some model calculations of the PWIA distribution $N(\vec{p}_m)$. Still further complications and extra model dependence will be involved if the experimentally measured cross section does not allow an integration over a sufficiently broad range of missing energy E_m. To

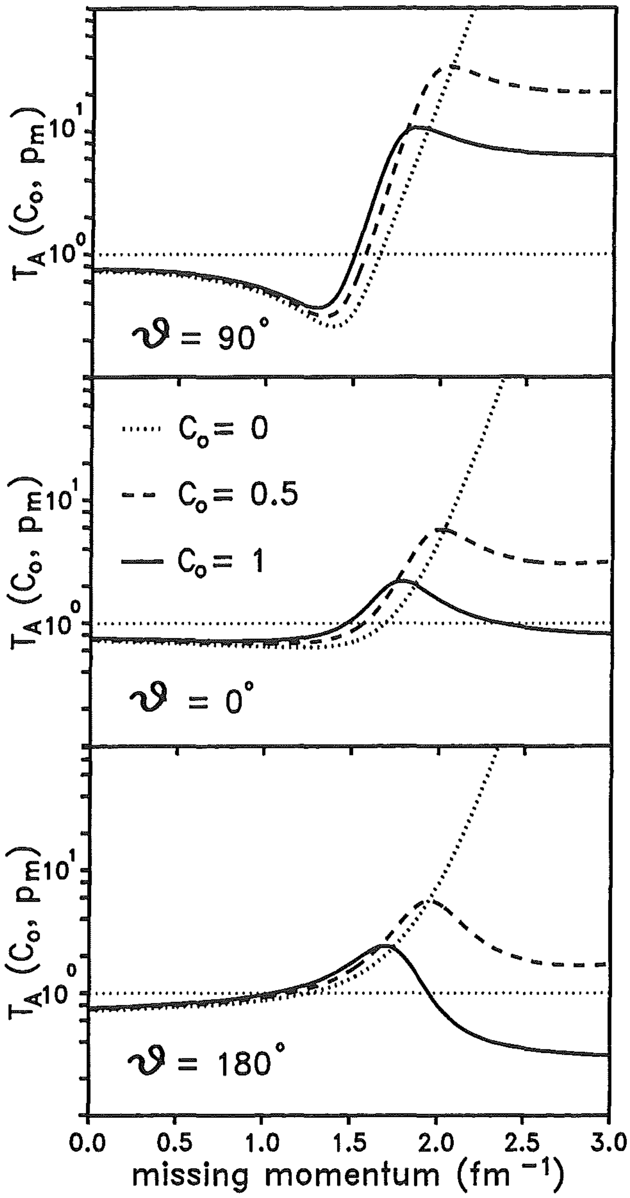

Figure 5.15: The nuclear transparency $T_A(\vec{p}_m)$ as defined in (5.36) is shown for hard core correlations, $C_o = 1$, (solid line), soft core correlations, $C_o = 0.5$, (dashed line) and no correlations at all, $C_o = 0$, (dotted line). The upper panel shows the results for $\theta = 90^o$, $\theta = 0^o$ is shown in the middle panel and $\theta = 180^o$ is shown in the lower panel. The other ground state parameters are $R_o = 1.29fm$ and $r_c = 0.5fm$.

a certain extent, this model SPMD $N(\vec{p}_m)$ can be checked against the experimentally measured missing momentum distribution $W(\vec{p}_m)$, implicitly and/or explicitly assuming that the FSI effects can be factored out as an overall attenuation factor.

The above presented results (see also [91]) very clearly show this is not the case and in large parts of the phase space such an evaluation of nuclear transparency can lead astray. Such a procedure was used, for instance, in an analysis of the data from the recent NE18 experiment [67, 68, 69]. Apart from the factorization assumption, in the NE18 analysis quite a large p_m-independent renormalization was applied to the model SPMD $N(\vec{p}_m)$ in anticipation of the short-range correlation induced reshuffling of strength from the small to large missing momenta. Here I only want to point out that the results of section 5.2, see Fig. 5.5, cast a shadow on such an oversimplified treatment of the correlation effects.

Having performed a full analysis of the combined SRC and FSI effects and having established a primacy of FSI effects, I now address the question of how strongly nuclear transparency is sensitive to correlation effects. In Fig. 5.15 I present the nuclear transparency calculated for different correlation strength,

$$T_A(C_0;\vec{p}_m) = \frac{W(C_0;\vec{p}_m)}{N(C_0;\vec{p}_m)}\,. \tag{5.36}$$

At large missing momenta, $p_m \gtrsim 1.5\,fm^{-1}$, the transparency becomes very sensitive to the correlation strength, this sensitivity comes entirely from $N(C_o, p_m)$. In the region of moderate missing momenta, $p_m \lesssim 1.3\,fm^{-1}$, though, nuclear transparency exhibits hardly any sensitivity to the correlation strength, which confirms the anticipation in [91].

The experimental data are often presented in terms of a nuclear transparency ratio for the cross sections integrated over a certain momentum window. I present the results for the longitudinal and perpendicular partially integrated transparencies T_L and $T_\perp$ defined as follows:

$$T_L(p_\perp = 0, p_z) = \frac{\int_0^{p_z} dp'_z\, W(p_\perp = 0, p'_z)}{\int_0^{p_z} dp'_z\, N(p_\perp = 0, p'_z)} \tag{5.37}$$

$$T_\perp(p_\perp, p_z = 0) = \frac{\int_0^{p_\perp} dp'_\perp\, p'_\perp\, W(p'_\perp, p_z = 0)}{\int_0^{p_\perp} dp'_\perp\, p'_\perp\, N(p'_\perp, p_z = 0)} \tag{5.38}$$

and the integrated transparency T_{int}

$$T_{int}(p_\perp) = \frac{\int_0^{p_\perp} dp'_\perp\, p'_\perp \int_{-\infty}^{\infty} dp_z\, W(p'_\perp, p_z)}{\int_0^{p_\perp} dp'_\perp\, p'_\perp \int_{-\infty}^{\infty} dp_z\, N(p'_\perp, p_z)}\,. \tag{5.39}$$

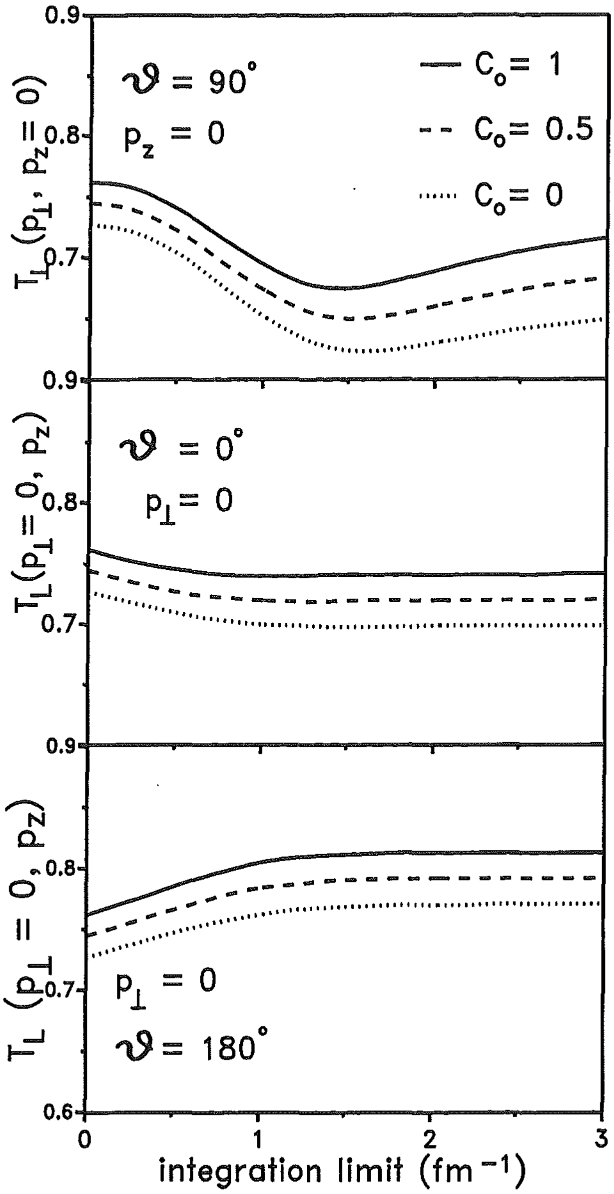

Figure 5.16: The ratios T_L ($T_\perp$) of the p_z ($p_\perp$) integrated spectral functions as function of the integration limit p_{max} as defined in (5.37), (5.38) are shown for hard core correlations, $C_o = 1$, (solid line), soft core correlations, $C_o = 0.5$, (dashed line) and no correlations at all, $C_o = 0$, (dotted line). The upper panel shows the results for $\theta = 90^o$, $\theta = 0^o$ is shown in the middle panel and $\theta = 180^o$ is shown in the lower panel. The other ground state parameters are $R_o = 1.29 fm$ and $r_c = 0.5 fm$.

In agreement with the discussion in [93] the integrated transparencies are larger when correlation effects are included. However, the overall effect is very small confirming

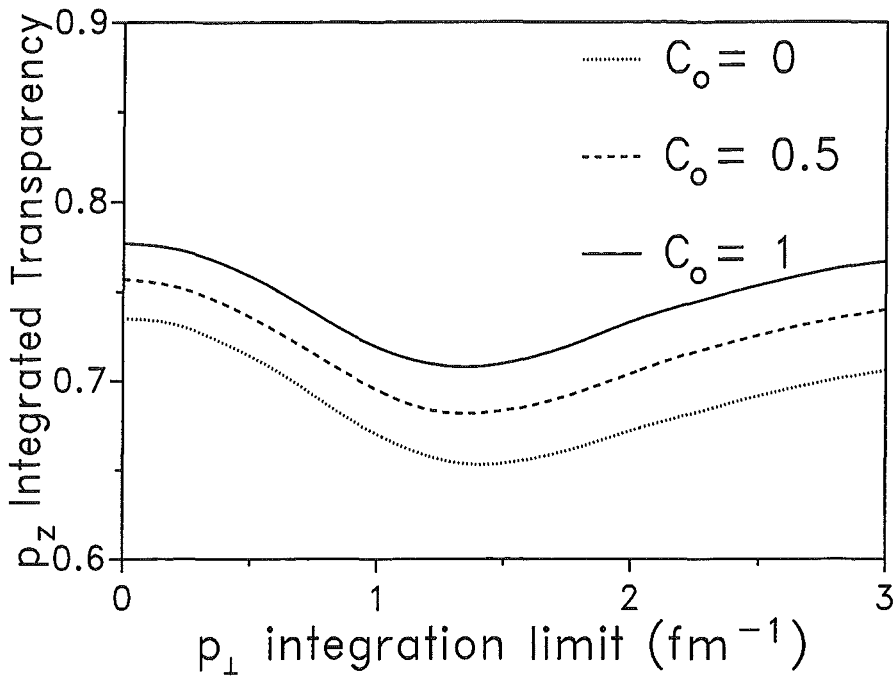

Figure 5.17: The fully integrated transparency T_{int} as function of the integration limit $p_{\perp,max}$ as defined in (5.39) are shown for hard core correlations, $C_o = 1$, (solid line), soft core correlations, $C_o = 0.5$, (dashed line) and no correlations at all, $C_o = 0$, (dotted line). The other ground state parameters are $R_o = 1.29 fm$ and $r_c = 0.5 fm$.

the conclusions of Ref. [94].

The variation of the partially integrated transparencies $T_\perp(p_\perp)$ and $T_L(p_z)$ with the upper limit of integration $p_\perp$ (p_z) is quite natural because the larger $p_\perp$ (p_z) is, the larger fraction of struck protons deflected by elastic scattering is included. What is not so obvious is that $T_{int}(p_\perp \sim 0)$ is not really smaller than the fully integrated transparency $T_{int}(\infty)$. The naive semiclassical expectation is that $1 - T_{int}(p_\perp \sim 0) \propto \sigma_{tot}(pN)$ vs. $1 - T_{int}(\infty) \propto \sigma_{in}(pN)$, because in distinction to the former case in the latter case the deflection of struck protons by elastic rescatterings cannot contribute to nuclear attenuation. This expectation is not borne out by exact calculation, which demonstrates the pitfalls of the semiclassical treatment of $W(\vec{p}_m)$ and the importance of the point that FSI distortions do not admit a classical interpretation.

5.7 Sensitivity of the Results to the Ansatz Wave Function

Quasielastic $A(e, e'p)$ scattering at large missing momentum p_m is a natural place to look at the large-p_m component of the single-particle momentum distribution, which is expected to be generated by short range correlations of nucleons in the ground state of a target nucleus and which is well known to rise with the correlation strength. The principal finding is that the large-p_m behavior of the observed missing momentum distribution in $^4He(e, e'p)$ is dominated by final state interaction of the struck proton with spectator nucleons and by the intricate interplay and quantal interference of the FSI and ground state correlation effects. In perpendicular kinematics, the FSI contribution to $W(\vec{p}_m)$ exceeds the SRC contribution to the SPMD by an order of magnitude. Even here, a substantial part of the FSI effect comes from a quantum-mechanical FSI-SRC interference effect in the one body density matrix, which defies a semiclassical interpretation. The pattern of FSI-SRC interference effects is still more complex in (anti)parallel kinematics, where a novel effect of strong enhancement of the forward-backward asymmetry by short range correlations in the ground state was found. In antiparallel kinematics, this SRC-FSI interference effect and the non-vanishing real part of the pN scattering amplitude lead to a decrease of the FSI-modified missing momentum distribution $W(\vec{p}_m)$ with the correlation strength, in contrast to the increase with the correlation strength of the single particle momentum distribution. FSI effects make a model-independent determination of the SPMD $N(\vec{p}_m)$ from the experimentally measured missing momentum distribution $W(\vec{p}_m)$ impossible. Large FSI effects are of quite a generic origin and are not an artifact of the employed semi-realistic Ansatz wave function.

The origin of the dominance of the final state interaction effects at large missing momenta is simple and well understood: the fact that the final state interactions are short ranged, with the interaction radius $b_o \approx 0.5 fm \ll R_A$, leads to large contributions at large missing momenta. In contrast to the short range correlations, the final state interactions are a short ranged function of the transverse separation only, in the longitudinal separation of two nucleons, they are long-ranged, therefore the FSI terms pick up a larger normalization, see Eqs. (5.24),(5.26).

There remains the intriguing possibility of the forward-backward asymmetry as a probe of short range correlations and further studies of the model dependence of this observable are worth while.

The Ansatz for the wave function was motivated by a desire to have a complete calculation of both short range correlation and final state interaction effects, rather than an evaluation of several lowest order terms. Even though much of the integrations and Fourier transforms can be performed analytically, the numerical calculations present quite a formidable task. The above presented results show that higher order correlation and FSI effects are indeed important. The simple Jastrow function only includes the S-wave correlations. The investigation of the missing momentum distribution for $^2H(e,e'p)$ scattering in the previous chapters suggests that the D-wave effects are not that important. Specifically, it has been shown that the sensitivity to different models for the deuteron wave function, which give D-wave contributions to $N(\vec{p}_m)$ differing at large p_m by an order of magnitude, is completely lost when including FSI. This insensitivity towards the D-wave is due to the fact that the FSI operator is short ranged and therefore does not affect the D-wave very much, as the D-wave is suppressed at small distances by the centrifugal barrier. At the interesting higher missing momenta, the missing momentum distribution was found to be dominated by FSI distortions of the S-wave contribution. Therefore, one can expect that the D-wave effects would not change the conclusions on the relative importance of the FSI and SRC effects at large p_m. One of the interesting findings is a substantial effect of higher order terms in the pair correlation function, which clearly shows an inadequacy of the simple quasi-deuteron model for the large-p_m component of the missing momentum distribution, both in PWIA and with allowance for FSI.

One interesting implication of the dominance of FSI effects at large p_m in both $^2H(e,e'p)$ and $^4He(e,e'p)$ scattering is the similarity of the missing momentum spectra, which will be discussed in the next chapter.

Chapter 6

Universality and Final State Interaction

In the past decades, a great theoretical effort has been devoted to the study of the nuclear single particle momentum distribution $N(k)$. Particular importance is attributed to the large momentum tail of $N(k)$, which is expected to be dominated by two nucleon short-range correlations, or "quasi-deuteron" configurations [44, 24, 45, 46, 13]. This name originates in the predicted analogous behavior of short-range interactions in all nuclei, from deuteron to nuclear matter. This should be reflected in a similar shape for the large k tail ($k > 1.5 - 2fm^{-1}$) of $N(k)$ in deuteron or in any other nucleus (hereafter the universality of $N(k)$ refers to the k dependence, apart from a k independent normalization factor). An example can be seen, e.g., in Fig. 5 of [23] where the ratio between the ^4He and D distributions varies roughly between 2.5 and 4.5 in the range $1fm^{-1} < k < 4fm^{-1}$. The earliest application of the quasi-deuteron idea can be found in the calculation of the nuclear photo effect for photons of energy larger than $150\,MeV$ (see [42], and references therein). However, the nucleon momenta considered there are slightly smaller than the momenta at which one expects the quasi-deuteron universality now. In [43], a microscopic evaluation of the nuclear momentum distributions for the ground states of ^4He and ^{16}O in two-body approximation was presented. The major finding of [43] was that beyond momenta of $2\,fm^{-1}$ the correlation part becomes dominating and that the general behaviour of the deuteron momentum distribution is quite similar to the one obtained for the closed shell nuclei.

Considering the results of the last chapter, where I found an important contribution also from higher order correlations to the ^4He ground state, it seems unclear if the quasi-deuteron hypothesis gives a quantitatively correct description of the nuclear ground states. However, here I would like to discuss the question if it is possible to find experimental evidence for the dominance of the quasi-deuteron at large momenta k from $(e, e'p)$ experiments, assuming that this dominance really is present. The results of this chapter have been published in [17].

In the previous chapters it was shown that the final state interaction completely dominates the missing momentum distribution at higher p_m in perpendicular kinematics and is very important in (anti)parallel kinematics. Moreover, the sensitivity of the missing momentum distribution $W(\vec{p}_m)$ to details of the ground state wave function like the D-wave or short range correlations is lost when FSI is included.

6.1 FSI-Induced Universality

As a further illustration of this point, I show the PWIA and the full transverse momentum distribution $W(\vec{p}_m)$ including FSI for the deuteron wave functions calculated from the Bonn and Paris models in Fig. 6.1. The well known smaller D-wave content of the Bonn model makes the corresponding PWIA much smaller than in the Paris model at large p_m. This difference gives an estimate of the uncertainties in the predictions of modern theories of the NN interaction at large $p_m \gtrsim 1.5 fm^{-1}$. However, when FSI are included the differences between the two distributions disappear: FSI, which distort the struck proton's wave function only at small distances $|\vec{b}| \lesssim b_o \ll R_A$, are hardly sensitive to the deuteron D-wave (where the centrifugal barrier keeps nucleons apart). In Fig. 6.1b I show how the distribution $W(\vec{p}_m)$ for the $^4He(e,e'p)$ reaction is changed for different types of short range correlations, going from $C_o = 0$ (pure mean field) to $C_o = 1$ (hard core). For perpendicular kinematics, the FSI-dominated distributions are not very sensitive to such drastic changes in the ground state wave function. The origin of this FSI dominance was discussed previously. These results for ^4He, as well as the washed out difference between the predictions from the Bonn and Paris potentials for the deuteron, nicely illustrate the main point: the transverse missing momentum distribution including FSI effects shows marginal sensitivity to the large-k components of the nuclear ground state Ψ_A, gross features of the bulk of the nuclear ground state only enter through the overall normalization and small corrections $\propto \frac{b_o^2}{R_A^2}$ to the slope of the p_m dependence. The behaviour of the transverse missing momentum distribution including FSI for large p_m is completely governed by the properties of the NN rescattering, which are universal for all nuclei.

In Fig. 6.2, the main quantitative point is presented: in perpendicular and (anti)parallel kinematics we show the missing momentum distributions $W(\vec{p}_m)$ including FSI for ^4He and for the deuteron. The latter is multiplied by 3 to take into

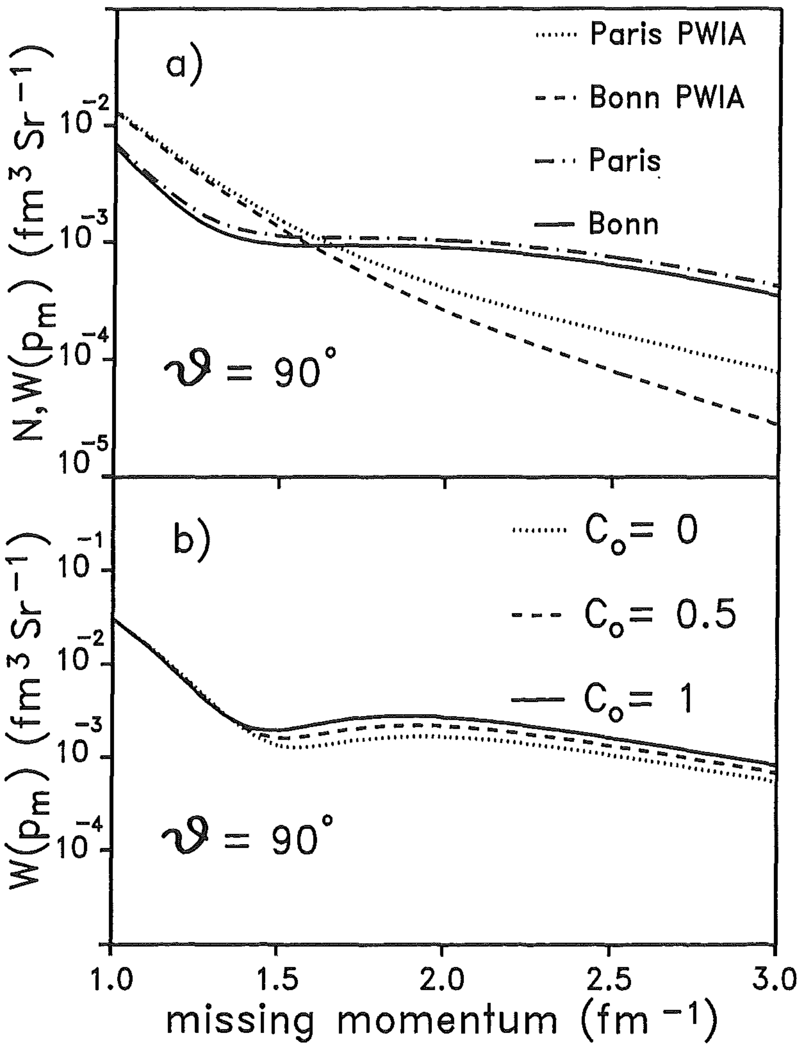

Figure 6.1: a) The PWIA missing momentum distribution $N(p_m)$ in the $D(e,e'p)$ reaction calculated with the Bonn wave function [25] (dashed line) and with the Paris wave function [26] (dotted line) and the full missing momentum distribution $W(\vec{p}_m)$ including FSI in the $D(e,e'p)$ reaction at $\theta = 90^o$ calculated with the Bonn wave function (solid line) and the Paris wave function (dash-dotted line). b) The full missing momentum distribution $W(\vec{p}_m)$ including FSI in the $^4He(e,e'p)$ reaction for hard core correlations $C_o = 1$ (solid line), soft core correlations $C_o = 0.5$ (dashed line), and pure mean field, $C_o = 0$ (dotted line).

account that in ^4He we have 3 FSI scatterers. The similarity between the distributions including FSI for ^4He and deuteron at p_m larger than $1.5 fm^{-1}$ is impressive, especially in perpendicular kinematics. It is even more striking if one compares the

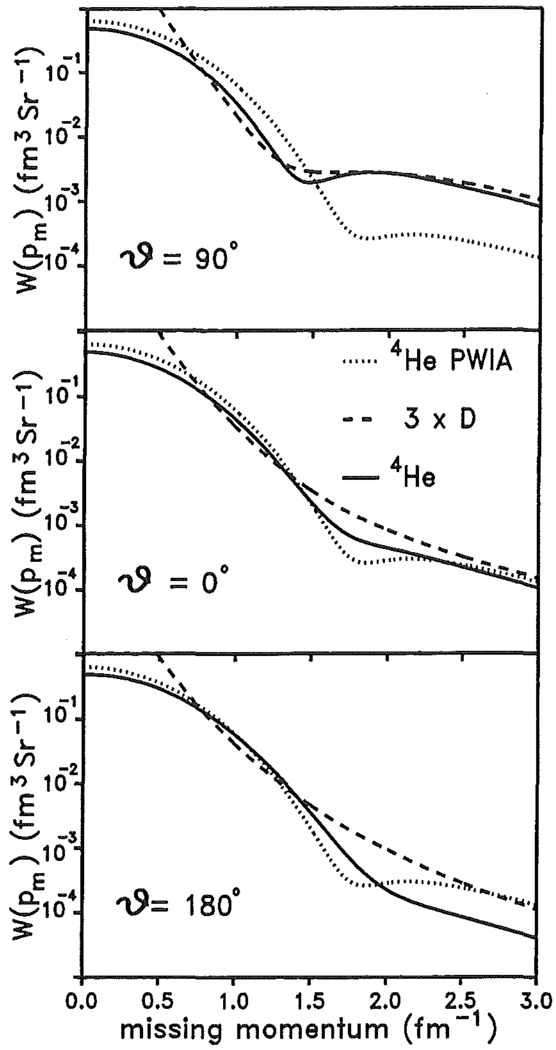

Figure 6.2: The full missing momentum distribution $W(\vec{p}_m)$ for the $^4He(e,e'p)$ reaction (solid line) and for the $D(e,e'p)$ reaction (dashed line) multiplied with a factor of 3 to account for the higher number of FSI scatterers in ^4He. For comparison, the PWIA missing momentum distribution $N(p_m)$ for ^4He is also shown (dotted line). On top, we show transverse kinematics, $\theta = 90^o$, and in the middle and the lower panel we show parallel and antiparallel kinematics, $\theta = 0^o$ and $\theta = 180^o$.

perpendicular and parallel distributions corresponding to one and the same nucleus (either deuteron or ^4He). They are equal in the fully isotropic PWIA prediction. On the contrary, at large p_m the full distributions $W(\vec{p}_m)$ for parallel and perpendicular kinematics differ by one order of magnitude, attesting the FSI dominance. So, at last, universality appears, but it is driven by the dominance of FSI effects rather

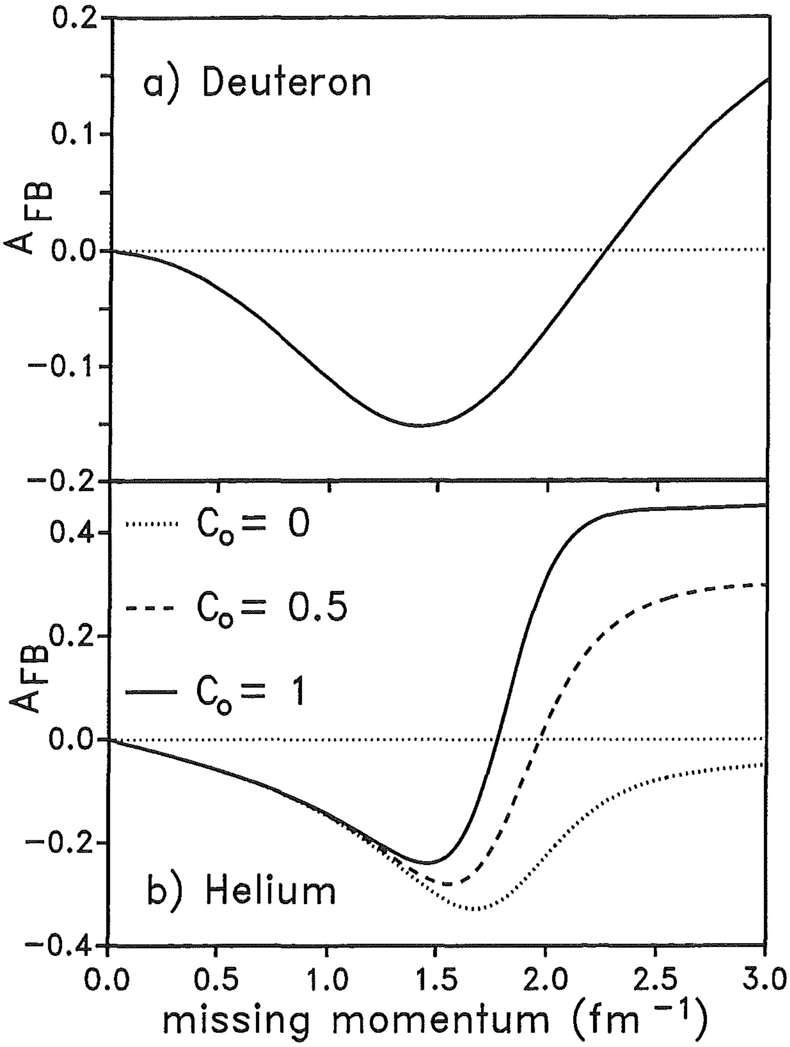

Figure 6.3: The forward-backward asymmetry A_{FB} defined in Eq. (3.11) is shown for the reaction $D(e,e'p)$ in a) and for the reaction ${}^4He(e,e'p)$ in b). For ${}^4He$, different correlations were used: hard core, $C_o = 1$, (solid line), soft core, $C_o = 0.5$, (dashed line), and pure mean field, $C_o = 0$ (dotted line).

than by an intrinsic feature of the nuclear ground state wave function.

In perpendicular kinematics, the PWIA curve is overwhelmed by the FSI effect by orders of magnitude. There is no hope to find *direct* quasi-deuteron effects in experiments performed in *perpendicular* kinematics. Even more confusion can arise from experiments in which events which are taken at different angles θ of the missing momentum $\vec{p}_m$ are put together as a function of $|\vec{p}_m|$ and are not presented in separate distributions. In perpendicular kinematics the FSI dominance is so marked that it seems difficult to think that a more refined ^4He ground state can modify this situation, especially as the missing momentum distribution for the $D(e,e'p)$ reaction in perpendicular kinematics calculated with realistic wave functions is also dominated by FSI and as the FSI effects in ^4He should be stronger than in the rather dilute deuteron.

In parallel kinematics, the situation seems more interesting. There, the results which were obtained previously suggest the FSI dominance in (anti)parallel kinematics is less pronounced than in perpendicular kinematics and that PWIA and FSI effects are in competition, and a quantitative understanding of their interplay can become decisive. At these kinematics, at large $p_{m,z}$, FSI effects are mainly due to the θ-function in the final state interaction operator. The related discontinuity introduces high-momentum longitudinal components. This is again a universal property of the FSI. Its presence does not depend on the specific target nucleus, although there is a slight sensitivity to the form of the correlation function.

Apart from this large $p_{m,z}$ tail, the interference between the PWIA amplitude and the component $\propto \rho$ of the FSI amplitude, leads to a forward-backward asymmetry, shown in Figs. 6.3a,b for ^4He and D. The mere presence of a large forward-backward asymmetry suggests strong FSI effects, and again its p_m dependence for deuteron and ^4He with soft core/hard core correlations included is qualitatively similar. The realistic deuteron wave functions do already include effects of the short range NN interaction. However, as the forward-backward asymmetry is a PWIA-FSI interference effect, it also contains some information on the nuclear ground state, as was shown in detail in chapter 4 and [16] for the special case of the polarized deuteron target, and therefore and due to the different values of ρ for D and ^4He the similarity is less pronounced than in perpendicular kinematics.

Concluding, the final state interaction creates strong similarity patterns in the energy-integrated momentum distributions for $(e,e'p)$ on ^4He and $(e,e'p)$ on deuteron at large missing momenta. This will permit detailed studies of universal features of nuclear FSI in the diffractive regime, but it makes tests of the short range structures in the nuclear ground state much more difficult. In particular, in perpendicular kinematics this task seems hopeless. It has to be stressed that FSI effects cannot be described by a simple overall renormalization factor as they depend strongly on the specific kinematics. A further analysis of the situation in longitudinal kinematics requires more sophisticated models for ^4He, due to the complex interplay of FSI and PWIA effects there.

Chapter 7

Summary and Conclusions

In this thesis, the effects of the final state interaction on the observables in $(e, e'p)$ reactions on light nuclei at GeV energies have been calculated using Glauber theory. In order to concentrate on the FSI effects, the photon was considered as a scalar operator, i.e. the longitudinal response function was calculated. The signature of final state interaction is a marked anisotropy in the observed missing momentum spectra, leading to a pronounced peak in perpendicular kinematics at higher missing momenta and a forward-backward asymmetry. The final state interaction induces a complicated pattern of shadowing and anti-shadowing in the nuclear transparency ratios, as the FSI effects depend strongly on the kinematics and the value of the missing momentum. It is impossible to describe the FSI effects by a simple overall factor. In all cases, a dominance of the final state interaction effects is found for higher missing momenta in perpendicular kinematics and their rôle in parallel and antiparallel kinematics is also important.

Even for the deuteron, which is a very dilute nucleus, the FSI effects lead to a deviation from the PWIA behaviour at $p_m \gtrsim 1\,fm^{-1}$ and they dominate the missing momentum distribution for $p_m \gtrsim 2\,fm^{-1}$ in perpendicular kinematics completely [14]. At missing momenta larger than $3\,fm^{-1}$, the FSI leads to smaller peaks in parallel and antiparallel kinematics. In PWIA, the influence of the D-wave contribution at higher momenta is large and the predictions of different models vary by almost one order of magnitude in this regime. However, the sensitivity of the missing momentum distribution to the D-wave is washed out entirely by FSI and an experimental discrimination of different models for the deuteron wave function seems to be impossible. Those results are contrary to the conventional expectation that FSI effects in the deuteron should be small in general and practically nonexistent in (anti)parallel kinematics. The FSI effects in (anti)parallel kinematics are substantial and lead to large FSI corrections of approximately 40% in the longitudinal missing momentum distribution. As the longitudinal missing momentum distribution is related to the asymptotic y-scaling function, those results indicate that FSI effects will have an important influence on the y-scaling analysis.

Also in electron scattering from tensor polarized deuterons [16], the FSI effects are strong. They dominate the missing momentum distribution in perpendicular kinematics from $1.5 fm^{-1}$ on and they are important in (anti)parallel kinematics, too. Because the FSI is sensitive to the alignment of the deuteron, the FSI effects depend strongly on the polarization of the deuteron, which leads to a rich pattern of the angular and p_m dependence of momentum distributions and tensor analyzing power. The departure of the nuclear transparency ratio $T(\vec{p}_m)$ is small only at small $p_m \approx 0 fm^{-1}$. At larger missing momenta, in the regions of strong PWIA-FSI interference and FSI dominance, one finds both $T \ll 1$ and $T \gg 1$. The antishadowing effect $T > 1$ is particularly strong in perpendicular kinematics. The tensor analyzing power is dominated by FSI even from the relatively low missing momentum of $p_m \approx 1\, fm^{-1}$ on, as the FSI is sensitive to the alignment of the deuteron. Although the S-wave and D-wave components of the deuteron wave function can interfere in scattering from polarized deuterons, in contrast to the situation in electron scattering from unpolarized deuterons, the sensitivity to the D-wave is lost when FSI is included. A unique possibility of determining properties of the ground state wave function directly from the experiment by measuring the zero of the forward-backward asymmetry for transversely polarized deuterons was pointed out. The forward-backward asymmetry arises from the interference of the PWIA and FSI and it seems to be a well suited tool for the investigation of the subtle interplay of FSI and PWIA effects in (anti)parallel kinematics.

As a representative example for heavier nuclei, ^4He was chosen and the FSI effects in inclusive $^4He(e,e'p)$ scattering were evaluated [15, 18]. ^4He is a very tightly bound nucleus and therefore its properties, e.g. the nucleon momentum distribution inside the nucleus, are expected to resemble the properties of heavier nuclei [43, 66]. In this thesis, a complete treatment of the inclusive $^4He(e,e'p)$ scattering to all orders in the correlation and final state interaction was presented. The simple though realistic model wave function that I use allows one to reduce the numerical calculations to a still lengthy and complicated but feasible task and enables one to identify the origin of specific effects. The investigation of FSI effects in inclusive $^4He(e,e'p)$ scattering shows an impressive dominance of FSI effects. In perpendicular kinematics, the missing momentum distribution including FSI overshoots the single particle momentum distribution by one order of magnitude for large missing momenta. Already at small p_m, the FSI leads to a distinct deviation from the PWIA behaviour, and for intermediate and large missing momenta, the FSI terms and the novel quantal FSI-SRC interference effects give large contributions. The influence of the strength of the short range correlations, which is remarkably large in PWIA, reduces so much once FSI is accounted for that it seems very difficult, almost impossible, to extract information on the strength or form of the correlations from the forthcoming experimental data. Actually, even the novel effect of the quantum-mechanical interference of FSI and SRC contributes much more to the missing momentum distribution than the pure SRC term. Those interference terms would be missed in any semi-classical treatment of FSI effects and defy any semi-classical interpretation. For a critical discussion of semiclassical approaches, see [91]. They are especially important in parallel and antiparallel kinematics, where they lead both to depletion and enhancement of the FSI-distorted missing momentum distribution. In parallel kinematics, the interplay of FSI and SRC terms leads to a virtual independence of the missing momentum distribution on the strength of the correlations. The strong interplay of the attenuation and distortion effects leads to a nuclear transparency T which exhibits both an even stronger depletion than the one of 24% for vanishing missing momentum and antishadowing behaviour. In the region of moderate missing momenta, $p_m \lesssim 1.3 fm^{-1}$, the nuclear transparency exhibits hardly any sensitivity to the correlation strength, thus confirming the anticipation in [91]. At large missing momenta, $p_m \gtrsim 1.5 fm^{-1}$, the transparency becomes very sensitive to the correlation strength. However, this does not yield any direct experimental information on the correlations since the transparency is not an observable because additional model assumptions about the single particle momentum distribution are needed to extract it from the data. The large FSI effects are of quite a generic origin and they are not an artifact of the model wave function used in the calculations.

The origin of the overwhelming FSI dominance at higher missing momenta is well understood: the radius of the final state interaction, b_o, is much smaller than the nuclear radius R_A. For this reason, the FSI contribution at large missing momenta $p_m \gtrsim \frac{1}{b_o}$ is large. The anisotropy of the final state interaction, which is short ranged in the transverse direction and long ranged in the longitudinal direction, leads to a large normalization of the FSI terms, in contrast to the isotropically short ranged correlation terms.

This property of FSI, which is universal for all target nuclei, leads to an approximate universality of the missing momentum spectra for different target nuclei [17]. In perpendicular kinematics, the distributions for ^4He and D (the latter is scaled by a factor of three to account for the larger number of spectator nucleons in ^4He) coincide almost perfectly for larger missing momenta. In (anti)parallel kinematics, the interplay of FSI and PWIA effects is more important and the similarity is not as striking as in perpendicular kinematics, although an approximately universal behaviour is clearly present. For a quantitative treatment of FSI in heavy nuclei, see [63, 35, 64]. Indeed, a strong effect of FSI in $(e, e'p)$ scattering on carbon and lead was found in [35].

The calculations in this thesis have been carried out for light nuclei. It is well known that due to the high density of ^4He, the correlation-induced large-p_m tail of the single particle momentum distribution does not change substantially from ^4He to heavy nuclei [66, 87, 95, 88]. It is also well known that the FSI effects rise steeply with the mass number. For instance, the nuclear transparency decreases from ~ 0.75 for ^4He down to ~ 0.25 for ^{197}Au [67, 68, 69]. This suggests strongly that FSI distortions will be still stronger and correlation effects will become marginal in $A(e, e'p)$ on heavy nuclear targets.

The results reported here will also affect the interpretation of the y-scaling analysis of $(e, e'p)$ scattering in terms of the single particle momentum distribution. To the extent that according to the experimental data, the FSI parameters - the total $p - N$ cross section, diffraction slope, the ratio ρ of real to imaginary part of the forward elastic scattering amplitude - vary only slightly for Q^2 of several GeV^2, the FSI dominated missing momentum distribution also shall stay approximately Q^2 independent over the CEBAF range of Q^2. This fact leads to an "FSI-scaling" effect that should not be confused with real y-scaling.

Although there are many publications on FSI at lower energies, e.g. in [96] FSI and SRC effects in the exclusive $^4He(e, e'p)^3He$ reaction at low energy and low missing momentum are discussed using a very different description of FSI, the FSI effects at energies of a few GeV, which are still lower than the energies where one expects color transparency effects, have not been investigated thoroughly up to now. The considered aspects of FSI and SRC were not discussed in previous work on semi-inclusive $A(e, e'p)$ scattering [97, 63, 98]. FSI effects in $D(e, e'p)$ scattering were discussed also in the recent work [99] using a different technique. These authors focused on corrections to the y-scaling analysis and did not consider the angular anisotropy of FSI effects. The results of [100] also show a strong influence of FSI effects on the $D(e,e'p)n$ and $\vec{D}(e,e'p)n$ reactions, confirming the earlier results of [14] and the findings in [16], which are presented in this thesis.

Another interesting application of the work presented here is the calculation of a sum rule for the Coulomb reacceleration of neutrons in the electro-dissociation of the deuteron [101]. In [101], the contribution of the final state interaction between the fragments of the electro-dissociation into the shift of the average velocity of fragments from the beam velocity was calculated. The reacceleration is related to the FSI-induced forward-backward asymmetry of the missing momentum distribution in the related $D(e,e'p)n$ scattering. Both acceleration and deceleration effects are possible depending on the sign of ρ. This contribution of FSI might help to explain the velocity shift between the neutrons and the ^9Li fragments in the Coulomb dissociation of ^{11}Li which was observed in a recent experiment [102, 103]. The observation was qualitatively interpreted as an effect of classical deceleration of ^{11}Li and acceleration of ^9Li in the Coulomb field and led to the discussion of the Coulomb reacceleration as a clock for nuclear reactions [102, 103, 104, 105]. The subsequent quantum-mechanical treatment of the reacceleration effect did not support this classical interpretation though (see [104, 105, 106], and references therein). The deuteron is the simplest example for the mechanism of reacceleration by FSI. With a suitable model wave function, the same calculation for the electro-dissociation of ^{11}Li can be performed.

The conclusions which can be drawn from the results presented in this thesis and in [15, 14, 16, 18, 17] for future experiments are that it will be very difficult to extract any kind of information on the high momentum component of the nuclear ground state by performing $(e,e'p)$ experiments at GeV energies. For this, a very tight control over the final state interaction on the theoretical side and an outstanding precision of the measurements on the experimental side will be necessary.

Appendix A

Jacobi coordinates

In the case of a multi-particle system it is often convenient to use Jacobi coordinates, which describe the relative motion of the particles. For systems of particles with equal mass, the k-th Jacobi coordinate is given by

$$\vec{R}_k = \vec{r}_{k+1} - \frac{1}{k}\sum_{i=1}^{k} \vec{r}_i \,, \tag{A.1}$$

where the $\vec{r}_i$ denote the laboratory coordinates of the particles. The k-th Jacobi coordinate points from the center of mass of the first k particles to the particle $k+1$. In order to express the Jacobi coordinates in lab coordinates and vice versa, one has to add the center of mass coordinate $\vec{R}_{CM} = \frac{1}{A}\sum_{i=1}^{A}\vec{r}_i = \vec{0}$ to the set of Jacobi coordinates. For the special case of the four particle system, e.g. ^4He, the Jacobi coordinates read:

$$\begin{aligned} \vec{R}_1 &= \vec{r}_2 - \vec{r}_1 \\ \vec{R}_2 &= \vec{r}_3 - \frac{\vec{r}_1 + \vec{r}_2}{3} \\ \vec{R}_3 &= \vec{r}_4 - \frac{\vec{r}_1 + \vec{r}_2 + \vec{r}_3}{3} \end{aligned} \tag{A.2}$$

and the lab coordinates are given by

$$\begin{aligned} \vec{r}_1 &= -\frac{1}{2}\vec{R}_1 - \frac{1}{3}\vec{R}_2 - \frac{1}{4}\vec{R}_3 \\ \vec{r}_2 &= \frac{1}{2}\vec{R}_1 - \frac{1}{3}\vec{R}_2 - \frac{1}{4}\vec{R}_3 \\ \vec{r}_3 &= \frac{2}{3}\vec{R}_2 - \frac{1}{4}\vec{R}_3 \\ \vec{r}_4 &= \frac{3}{4}\vec{R}_3 \,. \end{aligned}$$

In some parts of the text I have used $\vec{R}'_2 = \frac{2}{3}\vec{R}_2$ in order to simplify the appearing coefficients.

Appendix B

Kinematical Constraints

In this appendix, I give an overview over the kinematical conditions of the $D(e,e'p)n$ and $^4He(e,e'p)X$ reactions (where X stands for the possible final three-nucleon states). This is interesting in order to see e.g. over which range of the missing energy E_m and negative four momentum transfer Q^2 the experiments have to be carried out to find the momentum distribution.

In the experiment, the transferred energy ν, the transferred 3-momentum $\vec{q}$ and the kinetic energy of the knocked out proton $T_{kin,p}$ are measured. From $T_{kin,p}$, the modulus of the momentum, $|\vec{p}\,|$, can be extracted, and the direction of $\vec{p}$ is fixed by the detector position.

In the calculations, I have assumed a fixed $T_{kin,p}$ and I have calculated $W(\vec{p}_m)$ for various $\vec{p}_m$.

The modulus of the momentum of the detected proton is given by

$$|\vec{p}\,| = \sqrt{T_{kin,p}^2 + 2m_p T_{kin,p}} \tag{B.1}$$

and with the missing momentum

$$\vec{p}_m = \vec{q} - \vec{p}\,, \tag{B.2}$$

the proton angle $\theta_p = \sphericalangle(\vec{p}, \vec{q})$ is then given by

$$\theta_p = \arcsin\left(\frac{p_m}{p}\sin\theta\right)\,, \tag{B.3}$$

where θ is the angle of the missing momentum. For $T_{kin,p} = 1\,GeV$ the proton angle θ_p varies from $\theta_p = 3.4^o$ for $p_m = 0.05 fm^{-1}$ and $\theta_p = 28.1^o$ for $p_m = 4 fm^{-1}$ in perpendicular kinematics ($\theta = 90^o$). The proton angle for arbitrary angles θ of the missing momentum is smaller and obviously vanishes for (anti)parallel kinematics. This shows that the application of Glauber theory is justified in this regime, as Glauber theory works even for angles of 30°, see [40]. The modulus of the 3-momentum transfer is given by

$$|\vec{q}\,| = \sqrt{\vec{p}_m{}^2 + \vec{p}^{\,2} + 2|\vec{p}_m||\vec{p}\,|\cos(\theta + \theta_p)}\,. \tag{B.4}$$

The total energy E_{res} of the residual system is

$$E_{res} = \nu - E(p) + M_{target} \tag{B.5}$$

with the target mass M_{target} and the energy of the proton $E(p) = m_p + T_{kin,p}$. The residual system is recoiling with the missing momentum $\vec{p}_m$, so that one has

$$M_{res}^2 = E_{res}^2 - \vec{p}_m{}^2\,. \tag{B.6}$$

This expression for M_{res} contains the mass and the excitation energy of the residual system. Of course, in a specific reaction channel, M_{res} must be at least as large as the sum of the rest masses of the particles of the residual system, which leads to the necessary condition

$$M_{res} \geq M_{res,min} := \sum_i m_i \tag{B.7}$$

that is equivalent to the condition

$$E_{res} \geq E_{res,min} := T_{kin,res} + M_{res,min}\,. \tag{B.8}$$

The difference $M_{res} - M_{res,min}$ gives the intrinsic excitation energy of the residual system. This intrinsic energy consists of the kinetic energy of the relative motion of the particles which the residual system contains. The recoil energy of the residual system, i.e. the kinetic energy of it, is given by

$$T_{kin,res} = E_{rec} = \sqrt{\vec{p}_m{}^2 + M_{res}^2} - M_{res}\,. \tag{B.9}$$

The missing energy E_m equals

$$E_m := \nu - T_{kin,p} - T_{kin,res} = M_{res} + m_p - M_{target}\,. \tag{B.10}$$

For the considered type of experiment, the momentum transfer is space-like, so that the negative four momentum transfer squared must be positive, which gives another constraint for the kinematics:

$$Q^2 = \vec{q}^{\,2} - \nu^2 > 0\,. \tag{B.11}$$

This leads to a condition for the maximum energy transfer

$$\nu_{max} = |\vec{q}\,| \tag{B.12}$$

and from condition (B.8) the minimal energy transfer which is necessary is

$$\nu_{min} = E(p) - M_{target} + \sqrt{\vec{p}_m^{\;2} + M^2_{res,min}}\,. \tag{B.13}$$

Now the necessary background is set up and the kinematical settings and constraints for the specific reactions under consideration can be discussed in detail. Numbers for the kinematical variables are given in order to facilitate comparisons e.g. with the kinematical ranges of planned experiments.

B.1 Deuteron

First, the reaction $D(e, e'p)n$ is discussed, i.e. the reaction without any pions in the final state. The only possible missing energy equals the binding energy E_B of the deuteron:

$$E_m = E_B = 2.226\,MeV\,, \tag{B.14}$$

and the only possible mass of the residual system is obviously the neutron mass, $M_{res} = m_n$. The boundaries for the energy transfer ν now read

$$\begin{aligned} \nu_{min} &= m_p + T_{kin,p} - m_d + \sqrt{\vec{p}_m^{\;2} + m_n^2} \\ \nu_{max} &= \sqrt{\vec{p}_m^{\;2} + \vec{p}^{\,2} + 2|\vec{p}_m||\vec{p}\,|\cos(\theta + \theta_p)}\,. \end{aligned} \tag{B.15}$$

If the condition $\nu_{min} < \nu_{max}$ is fulfilled, the only possible energy transfer is $\nu = \nu_{min}$; higher values of the transferred energy are only possible if they excite a resonance of the nucleon, therefore leading to pions in the final state after the decay of the resonance. The minimum value of the energy transfer equals $1.0\,GeV$ for $p_m = 0\,fm^{-1}$ and $1.297\,GeV$ for $p_m = 4\,fm^{-1}$. The transferred three momentum $|\vec{q}|$ equal to ν_{max} is $1.7\,GeV$ for $p_m = 0\,fm^{-1}$ and is given in table B.1 for $p_m = 4\,fm^{-1}$ for parallel and perpendicular kinematics and for $p_{m,max}$ in antiparallel kinematics.

In table B.1, the kinematical constraints following from the above conditions are shown. As can be seen from Eq. (B.15), the condition $\nu_{min} < \nu_{max}$ is most restrictive in antiparallel kinematics, where $\theta = 180^o$ and the cosine term in the expression for ν_{max} is close to -1, as the proton angle is zero in antiparallel kinematics. Correspondingly, the possible maximal values of Q^2 decrease in antiparallel kinematics

θ	$p_{m,max}$	ν_{max}	Q^2_{max}
0^o	$> 10\,fm^{-1}$	$2.5\,GeV$	$4.56\,GeV^2$
90^o	$4.5\,fm^{-1}$	$1.5\,GeV$	$1.87\,GeV^2$
180^o	$2.5\,fm^{-1}$	$1.2\,GeV$	$1.87\,GeV^2$

Table B.1: This table shows the kinematical constraints for the $D(e,e'p)n$ reaction in parallel, perpendicular and antiparallel kinematics at $T_{kin,p} = 1\,GeV$. For each kinematics, the accessible maximal missing momentum $p_{m,max}$ is given in the first column, the maximal transferred energy at $p_m = 4fm^{-1}$ or $p_{m,max}$, respectively, is given in the second column and the maximal value of Q^2 for the whole considered missing momentum range $p_m \leq 4fm^{-1}$ is given in the third column.

until they reach zero. Also in perpendicular kinematics, the range of missing momenta is limited, as the proton angle increases with higher p_m, leading to smaller values of ν_{max}. So also here, the maximal value of Q^2, i.e. $Q^2_{max} = \nu^2_{max} - \nu^2_{min}$ decreases for higher missing momenta, so that the maximal four momentum transfer squared is given by the value of $Q^2 = 1.87GeV^2$ for vanishing missing momentum.

The accessible range of missing momenta is increased when the kinetic energy of the proton is increased. The results presented in this thesis have been obtained for $T_{kin,p} = 1\,GeV$, but as the parameters entering the FSI operator hardly change for higher energies, the results will remain the same for $T_{kin,p} > 1\,GeV$.

Now, the reaction $D(e,e'p)n\pi$ is considered. In contrast to the previous case, excitations of the residual $\pi + n$ system are possible, leading to a broad spectrum of missing energies. The minimum missing energy for this reaction is

$$E_{m,min} = m_\pi + E_B \approx 140\,MeV\,. \tag{B.16}$$

This missing energy is much larger than the missing energy of $E_m = 2.226\,MeV$ one has without the pion in the final state. The expression for $\nu_{max} = |\vec{q}|$ remains the same as above, the minimum necessary energy transfer is now

$$\nu_{min} = m_p + T_{kin,p} - m_d + \sqrt{\vec{p}_m^{\;2} + m_n^2 + m_\pi^2 + 2m_n m_\pi}\,. \tag{B.17}$$

The accessible kinematical regions are shown in table B.2. The limits on the range of the missing momentum are similar, although the upper bounds are slightly smaller now, and also the Q^2 values are slightly smaller, due to the fact that some extra energy is needed for the production of the pion. For vanishing missing momentum,

$p_m = 0$, the missing energy is $E_m = 696\,MeV$. In antiparallel and perpendicular kinematics, this is the maximum value of the missing energy which decreases until it reaches the lower bound. In parallel kinematics, the missing energy increases and reaches $E_m = 1.36\,GeV$ at $p_m = 4fm^{-1}$.

θ	$p_{m,max}$	ν_{max}	Q^2_{max}
0^o	$9.5\,fm^{-1}$	$2.5\,GeV$	$4.25\,GeV$
90^o	$4.4\,fm^{-1}$	$1.5\,GeV$	$1.57\,GeV$
180^o	$2.3\,fm^{-1}$	$1.2\,GeV$	$1.57\,GeV$

Table B.2: This table shows the kinematical constraints for the $D(e,e'p)n\pi$ reaction in parallel, perpendicular and antiparallel kinematics at $T_{kin,p} = 1\,GeV$. For each kinematics, the accessible maximal missing momentum $p_{m,max}$ is given in the first column, the maximal transferred energy at $p_m = 4fm^{-1}$ or $p_{m,max}$, respectively, is given in the second column and the maximal value of Q^2 for the whole considered missing momentum range $p_m \leq 4fm^{-1}$ is given in the third column.

B.2 Helium

In this thesis, I have considered the inclusive $^4He(e,e'p)$ reaction, i.e. I have summed over all possible final states. There are several possible final states:

- The two-body breakup channel $^4He(e,e'p)^3H$ with the triton ground state as final state. In this channel, the missing energy has the fixed value $E_m = 19.8\,MeV$.
- The three-body breakup channels $^4He(e,e'p)Dn$ with a minimum missing energy of $E_m = 26.1\,MeV$ and $^4He(e,e'p)pnn$ with a minimum missing energy of $E_m = 28.3\,MeV$.

The values of ν and Q^2 for the two-body break-up channel are fairly similar to the values for the $D(e,e'p)n$ reaction. The situation in the three-body break-up channels is more interesting as there is a broad range of missing energy accessible. As the two channels are quite similar, I give numbers only for the $^4He(e,e'p)Dn$ reaction. For vanishing missing momentum, $p_m = 0fm^{-1}$, the possible energy transfers range from $1.03\,GeV$ to $1.7\,GeV$, the corresponding missing energies range from $26\,MeV$

to 696 MeV, and the maximal attainable Q^2 is 1.82 GeV for all kinematics. Both in antiparallel and perpendicular kinematics the missing momenta are limited, and the maximum value of the missing energy is therefore 696 MeV. In parallel kinematics, however, the missing energy spectrum extends to higher values with increasing p_m and reaches $E_m = 1.42\, GeV$ at $p_m = 4 fm^{-1}$.

When there are pions in the final state, the value for ν_{min} increases to 1.17 GeV for $p_m = 0 fm^{-1}$ and to 1.27 GeV for $p_m = 4 fm^{-1}$. The minimal missing energy is 166 MeV. Once the transferred energy is larger than ν_{min}, the two types of reactions cannot be distinguished solely through the kinematics. However, it should be possible to identify the pions in the experiment. At CEBAF, there is a multi-particle spectrometer available which detects all charged particles. With this additional information on the residual system, the reaction can be reconstructed.

Bibliography

[1] R.Hofstadter, Annu. Rev. Nucl. Sci. **7**, 231 (1957).

[2] K.Gottfried, Ann. Phys. **21**, 29 (1963).

[3] W.Czyż and K.Gottfried, Nucl. Phys. **21**, 676 (1961).

[4] W.Czyż and K.Gottfried, Ann. Phys. **21**, 47 (1963).

[5] N.Srivastava, Phys. Rev. **135**, 612 (1964).

[6] D.U.L.Yu, Ann. Phys. **38**, 392 (1966).

[7] J. Orden, W.Truex, and M.K.Banerjee, Phys. Rev. C **21**, 2628 (1980).

[8] S.Fantoni and V.R.Pandharipande, Nucl. Phys. **A427**, 473 (1984).

[9] S.C.Pieper, R.B.Wiringa, and V.R.Pandharipande, Phys. Rev. C **46**, 1741 (1992).

[10] R.Jastrow, Phys. Rev. **98**, 1479 (1955).

[11] S.Frullani and J.Mougey, Adv. Nucl. Phys. **14**, 3 (1984).

[12] A.E.I.Dieperink and P. de Witt Huberts, Annu. Rev. Nucl. Part. Sci. **40**, 239 (1990).

[13] S.Boffi, C.Giusti, and F.D.Pacati, Phys. Rep. **226**, 1 (1993).

[14] A.Bianconi, S.Jeschonnek, N.N.Nikolaev, and B.G.Zakharov, Phys. Lett. **B343**, 13 (1995).

[15] A.Bianconi, S.Jeschonnek, N.N.Nikolaev, and B.G.Zakharov, Phys. Lett. **B338**, 123 (1994).

[16] A.Bianconi, S.Jeschonnek, N.N.Nikolaev, and B.G.Zakharov, Phys. Rev. C , in print (1996).

[17] A.Bianconi, S.Jeschonnek, N.N.Nikolaev, and B.G.Zakharov, Phys. Lett. **B363**, 217 (1995).

[18] A.Bianconi, S.Jeschonnek, N.N.Nikolaev, and B.G.Zakharov, Jülich preprint KFA-IKP(Th)-1995-13 , submitted to Nuclear Physics A (1995).

[19] R.J.Glauber, in *Lectures in Theoretical Physics*, edited by W.Brittain and L.G.Dunham (Interscience Publ., New York, 1959), No. 1.

[20] R.J.Glauber and G.Matthiae, Nucl. Phys. **B21**, 135 (1970).

[21] J.Golak, H.Kamada, H.Witala, W.Glöckle, and S.Ishikawa, Phys. Rev. C **51**, 1638 (1995).

[22] M.Viviani, A.Kievsky, and S.Rosati, Few Body Systems **18**, 25 (1995).

[23] R.B.Wiringa, Nucl. Phys. **A543**, 199c (1992).

[24] J.Carlson, Phys. Rev. C **36**, 2026 (1987).

[25] R.Machleidt, K.Holinde, and C.Elster, Phys. Rep. **149**, 1 (1987).

[26] M.Lacombe, B.Loiseau, R. Mau, J.Cote, P.Pires, and R. Tourreil, Phys. Lett. **B101**, 139 (1981).

[27] R. V. Reid, Jr., Ann. Phys. **50**, 411 (1968).

[28] R.B.Wiringa, R.A.Smith, and T.L.Ainsworth, Phys. Rev. C **29**, 1207 (1984).

[29] S.A.Coon, M.D.Scadron, P.C.McNamee, B.R.Barret, D.W.E.Blatt, and B.H.J.McKellar, Nucl. Phys. **A317**, 242 (1979).

[30] R.Schiavilla, V.R.Pandharipande, and R.B.Wiringa, Nucl. Phys. **A449**, 219 (1986).

[31] R.B.Wiringa, Phys. Rev. C **43**, 1585 (1991).

[32] A.H.Mueller, in *XVII Rencontres de Moriond, Les Arcs, France*, edited by T.T.Van (Editions Frontieres, Gif-sur-Yvette, 1982), p. 13.

[33] S.J.Brodsky, in *XIII Int. Symp. on Multiparticle Dynamics, Volendam, The Netherlands*, edited by E.W.Kittel, W.Metzger, and A.Stergion (World Scientific, Singapore, 1982), p. 963.

[34] N.N.Nikolaev, Surveys in High Energy Physics **7**, 1 (1994).

[35] N.N.Nikolaev, A.Szczurek, J.Speth, J.Wambach, B.G.Zakharov, and V.R.Zoller, Nucl. Phys. **A567**, 781 (1994).

[36] B.Jennings and B.Z.Kopeliovich, Phys. Rev. Lett. **70**, 3384 (1993).

[37] N.N.Nikolaev, A.Szczurek, J.Speth, J.Wambach, B.G.Zakharov, and V.R.Zoller, Phys. Lett. **B317**, 287 (1993).

[38] A.Bianconi, S.Boffi, and D.E.Kharzeev, Phys. Lett. **B325**, 294 (1994).

[39] K. Egiyan, L. Frankfurt, W. Greenberg, G. Miller, M. Sargsyan, and M. Strikman, Nucl. Phys. **A580**, 365 (1994).

[40] G.D.Alkhazov, S.I.Belostotsky, and A.A.Vorobyev, Phys. Rep. **42**, 89 (1978).

[41] S.J.Wallace, Adv. Nucl. Phys. **12**, 135 (1981).

[42] J.S.Levinger, Phys. Rev. **84**, 43 (1951).

[43] J.G.Zabolitzky and W.Ey, Phys. Lett. **B76**, 527 (1978).

[44] R.Schiavilla, V.R.Pandharipande, and R.B.Wiringa, Nucl. Phys. **A449**, 219 (1986).

[45] C.Marchand *et al.*, Phys. Rev. Lett. **60**, 1703 (1988).

[46] C.Ciofi degli Atti, S.Liuti, and S.Simula, Phys. Rev. C **41**, R2474 (1990).

[47] G.Jacob and Th.A.J.Maris, Rev. Mod. Phys. **38**, 121 (1966).

[48] T.deForest Jr., Nucl. Phys. **A392**, 232 (1983).

[49] C.Lechanoine-LeLuc and F.Lehar, Rev. Mod. Phys. **65**, 47 (1993).

[50] M.Bleszynski *et al.*, Phys. Lett. **B87**, 198 (1979).

[51] V.Braun, L.G.Dakhno, and V.A.Nikonov, Sov. J. Nucl. Phys. **44**, 848 (1986).

[52] S.J.Wallace, Phys. Rev. C **12**, 179 (1975).

[53] T.Lasinski *et al.*, Nucl. Phys. **B37**, 1 (1972).

[54] B.H.Silverman *et al.*, Nucl. Phys. **A499**, 763 (1989).

[55] A.V.Dobrovolsky *et al.*, Nucl. Phys. **B214**, 1 (1983).

[56] W.Grein and P.Kroll, Nucl. Phys. **A377**, 505 (1982).

[57] S.J.Wallace, Phys. Rev. D **8**, 1846 (1973).

[58] S.J.Wallace and J.A.McNeil, Phys. Rev. D **16**, 3565 (1977).

[59] S.J.Wallace, Phys. Rev. D **9**, 406 (1974).

[60] H.D.I.Abarbanel and C.Itzykson, Phys. Rev. Lett. **23**, 53 (1969).

[61] V.N.Gribov, Sov. Phys. JETP **29**, 483 (1969).

[62] R.D.Smith and S.J.Wallace, Phys. Rev. C **32**, 1654 (1986).

[63] N.N.Nikolaev, A.Szczurek, J.Speth, J.Wambach, B.G.Zakharov, and V.R.Zoller, Phys. Rev. C **50**, R1296 (1994).

[64] J.Nemchik, N.N.Nikolaev, and B.G.Zakharov, in *Workshop on CEBAF at Higher Energies*, edited by N. Isgur and P. Stoler (CEBAF, Newport News, Va., USA, 1994), p. 415.

[65] G.B.West, Phys. Rep. **18**, 264 (1975).

[66] C.Ciofi degli Atti, E.Pace, and G.Salme, Phys. Rev. C **43**, 1155 (1991), and references therein.

[67] N.C.R.Makins *et al.*, Phys. Rev. Lett. **72**, 1986 (1994).

[68] T.G. O'Neill *et al.*, Phys. Lett. **B351**, 87 (1995).

[69] N.C.R.Makins and R.G.Milner, preprint MIT-LNS **94-79** .

[70] D.Day *et al.*, Phys. Rev. Lett. **59**, 427 (1987).

[71] J.M.Fontaine *et al.*, Nucl. Phys. **B358**, 297 (1991).

[72] S.M.Bilensky and R.M.Ryndin, Phys. Lett. **6**, 217 (1963).

[73] J.Bystricky, C.Lechanoine-LeLuc, and F.Lehar, J. Phys. (Paris) **51**, 2747 (1990).

[74] P.Kroll, in *Phenomenological Analyses of Nucleon-Nucleon Scattering*, edited by H.Behrens and G.Ebel (Fachinformationszentrum, Karlsruhe, 1981), No. 22-1.

[75] D.R.Harrington, Phys. Rev. **21**, 1496 (1968).

[76] V.Franco and R.J.Glauber, Phys. Rev. **22**, 370 (1969).

[77] J.Mougey (spokesperson), CEBAF Proposal No. E-89-044.

[78] R.G.Milner (spokesperson), CEBAF Proposal No. E-91-007.

[79] D.F.Geesaman (spokesperson), CEBAF Proposal No. E-91-011.

[80] K.Rith (spokesperson), HERMES proposal at HERA .

[81] W.Fabian and H.Arenhövel, Nucl. Phys. **A445**, 461 (1976).

[82] H.Arenhövel and M.Sanzone in *Few Body Systems, Supplementum* 3 (Springer Verlag, Heidelberg,1991).

[83] J.M.R.Kellog, I.I.Rabi, N.F.Ramsey, and J.R.Zacharias, Phys. Rev. **56**, 728 (1939).

[84] M.Traini and G.Orlandini, Z. Phys. **A321**, 479 (1985).

[85] A.N.Antonov, P.E.Hodgson, and I.Zh.Petkov, *Nucleon Momentum and Density Distributions in Nuclei* (Clarendon Press, Oxford, 1988).

[86] R.I.Dzhibuti and R.Ya.Kezerashvili, Sov. J. Nucl. Phys. **20**, 17 (1974).

[87] V.R.Pandharipande and S.C.Pieper, Phys. Rev. C **45**, 791 (1992).

[88] G.Co', A.Fabrocini, and S.Fantoni, Nucl. Phys. **A568**, 73 (1994).

[89] H. Vries, C. de Jager, and C. de Vries, Atomic Data and Nuclear Data Tables **36**, 495 (1987).

[90] L.G.Dakhno and N.N.Nikolaev, Nucl. Phys. **A436**, 653 (1985).

[91] N.N.Nikolaev, J.Speth, and B.G.Zakharov, Jülich preprint KFA-IKP(Th)-1995-01 , (1995).

[92] N.N.Nikolaev, A.Szczurek, J.Speth, J.Wambach, B.G.Zakharov, and V.R.Zoller, Nucl. Phys. **A582**, 665 (1995).

[93] O.Benhar, A.Fabrocini, S.Fantoni, V.R.Pandharipande, and I.Sick, Phys. Rev. Lett. **69**, 881 (1992).

[94] N.N.Nikolaev, A.Szczurek, J.Speth, J.Wambach, B.G.Zakharov, and V.R.Zoller, Phys. Lett. **B317**, 281 (1993).

[95] R.Schiavilla, D.S.Lewart, V.R.Pandharipande, S.C.Pieper, R.B.Wiringa, and S.Fantoni, Nucl. Phys. **A473**, 267 (1987).

[96] R.Schiavilla, Phys. Rev. Lett. **65**, 835 (1990).

[97] A.Kohama, K.Yazaki, and R.Seki, Nucl. Phys. **A551**, 687 (1993).

[98] A.S.Rinat and B.K.Jennings, Nucl. Phys. **A568**, 873 (1994).

[99] C.Ciofi degli Atti and S.Simula, Phys. Lett. **B325**, 276 (1994).

[100] L.L.Frankfurt, W.R.Greenberg, G.A.Miller, M.M.Sargsyan, and M.I.Strikman, Z. Phys. A **352**, 97 (1995).

[101] A.Bianconi, S.Jeschonnek, N.N.Nikolaev, and B.G.Zakharov, Phys. Rev. C **51**, 1584 (1995).

[102] K.Ieki *et al.*, Phys. Rev. Lett. **70**, 730 (1993).

[103] D.Sackett *et al.*, Phys. Rev. C **48**, 118 (1993).

[104] G.F.Bertsch and C.A.Bertulani, Nucl. Phys. **A556**, 136 (1993).

[105] G.F.Bertsch and C.A.Bertulani, Phys. Rev. C **49**, 2389 (1994).

[106] S.Typel and G.Baur, Nucl. Phys. **A573**, 486 (1994).

Acknowledgments

The research work for this thesis was carried out at the Institut für Kernphysik, Forschungszentrum Jülich, from February 1993 to December 1995. I would like to thank everyone who has contributed to the successful completion of this work:

I would like to thank Professor J. Speth for his encouragement, continuous support and interest in my work. I have benefited from the opportunities he has created for me, especially from the exchange program with Italy.

I am grateful to Professor N. N. Nikolaev not only for his invaluable contribution to this work, but also for his continuous advice, teaching, all our discussions and his daily help. I have profited a lot from his profound knowledge and I have always enjoyed working with him.

I would like to thank Andrea Bianconi for our successful collaboration, the many discussions we had and for his assistance in organizing my stays in Italy.

I would like to thank Dr. B. G. Zakharov for the fruitful collaboration.

I would like to thank Professor S. Boffi and the theory group of the Dipartimento di Fisica Nucleare e Teorica, Pavia University, for their friendly hospitality. I would like to thank the german academic exchange service (DAAD) for the financial support of those visits.

I thank Alessandra Saino and Cristina Riccardi for sharing their apartment in Pavia with me, for teaching me Italian and for turning my working trips to Pavia into enjoyable stays.

I am grateful to Professor A. Fabrocini (Pisa), Professor C. Ciofi degli Atti (Perugia), Dr. S. Simula (Rome), and Professor G. Co' (Lecce) for their invitations enabling me to present and discuss my work and to travel through Italy.

I would like to thank Professor S. Krewald, Dr. A. Szczurek, and Professor G. Co' for many discussions and the collaboration on the $^{12}C(e,e'N)$ reaction.

I am grateful to Dr. S. Bass for checking parts of the manuscript.

I would like to thank Frau Bley and Frau Burck for their friendly help in any administrative problems.

I am grateful to all members and guests of the theory group at IKP for creating a friendly and stimulating environment. Special thanks go to Monika Hoffmann, Christoph Hanhart and Michael Buballa, who have not only shared my room, but also my ups and downs during the past years.

I would like to thank my husband Volker for his support, care, encouragement and patience.

I am grateful to my parents for their support throughout my studies.

FORSCHUNGSZENTRUM JÜLICH GmbH

KFA

Jül-3175
Januar 1996
ISSN 0944-2952